Chem Soc Rev

REVIEW ARTICLE

View Article Online
View Journal | View Issue

Cite this: *Chem. Soc. Rev.*, 2023, **52**, 6754

Dihydroindenofluorenes as building units in organic semiconductors for organic electronics

Cyril Poriel and Joëlle Rault-Berthelot

This review aims to discuss organic semiconductors constructed on dihydroindenofluorene positional isomers, which are key molecular scaffolds in organic electronics. Bridged oligophenylenes are key organic semiconductors that have allowed the development of organic electronic technologies. Dihydroindenofluorenes (DHIFs) belong to the family of bridged oligophenylenes constructed on a terphenyl backbone. They have proven to be very promising building blocks for the construction of highly efficient organic semiconductors for all OE devices, namely organic light emitting diodes (OLEDs), phosphorescent OLEDs, organic field-effect transistors (OFETs), solar cells, *etc.*

Received 13th April 2023

DOI: 10.1039/d1cs00993a

rsc.li/chem-soc-rev

In the DHIF family, there are five positional isomers, with different phenyl linkages (*para*/*meta*/*ortho*) and different ring bridge arrangements (*anti*/*syn*) (Scheme 1).

UMR CNRS 6226-Université Rennes 1-ISCR-Campus de Beaulieu, 35042 Rennes, France. E-mail: cyril.poriel@univ-rennes1.fr, joelle.rault-berthelot@univ-rennes1.fr

6,12-Dihydroindeno[1,2-*b*]fluorene (**[1,2-*b*]-DHIF**) is constructed on a *para*-terphenyl core and possesses *anti* geometry. This isomer displays many appealing properties such as a high quantum yield and a low oxidation potential and can be easily functionalized at the bridge and/or at the phenyl units to tune its properties. Thus, many functional groups have been attached to this scaffold in order to fit with the requirements of specific applications (OLED, OFET,

Cyril Poriel

Cyril Poriel is a CNRS Research Director at "Institut des Sciences Chimiques de Rennes" – UMR 6226 (Rennes 1 University, France). His main research interest deals with the design of π-conjugated molecular architectures for organic electronics. He is particularly interested in the design of blue emitting fluorophores for organic light-emitting diodes (OLEDs), high triplet host materials for phosphorescent OLEDs, electron-deficient semiconductors for n-type organic field-effect transistors and, more recently, in nanoring chemistry.

Joëlle Rault-Berthelot

Joëlle Rault-Berthelot is a "CNRS Research Director" at "Institut des Sciences Chimiques de Rennes" – UMR 6226 (Rennes 1 University, France). She has more than 40 years of experience in electrochemistry of π-conjugated systems. She is recognized for her work on electrode surface modification: graphite intercalation compounds (1981–1985) and conducting polymers such as polyfluorene derivatives, polydibenzo-crown-ethers, polyphenylenes, polyarylporphyrines, and so on. She developed the electrochemical synthesis of the polymers and studied their main properties and applications (electrochromism, sensors, catalysis, etc. (1985–2007). Since 2005, she has been working on new materials for organic electronics: design, physico-chemical properties and uses as active layers in electronic devices. Among them: new three-dimensional molecules with « 2π-1spiro » or « 3π-2spiro » architectures in view of their use as active layers in fluorescent OLEDs, as a host for PhOLEDs, and new linear molecules with low LUMO levels and their use as the active layer in n-type OFETs.

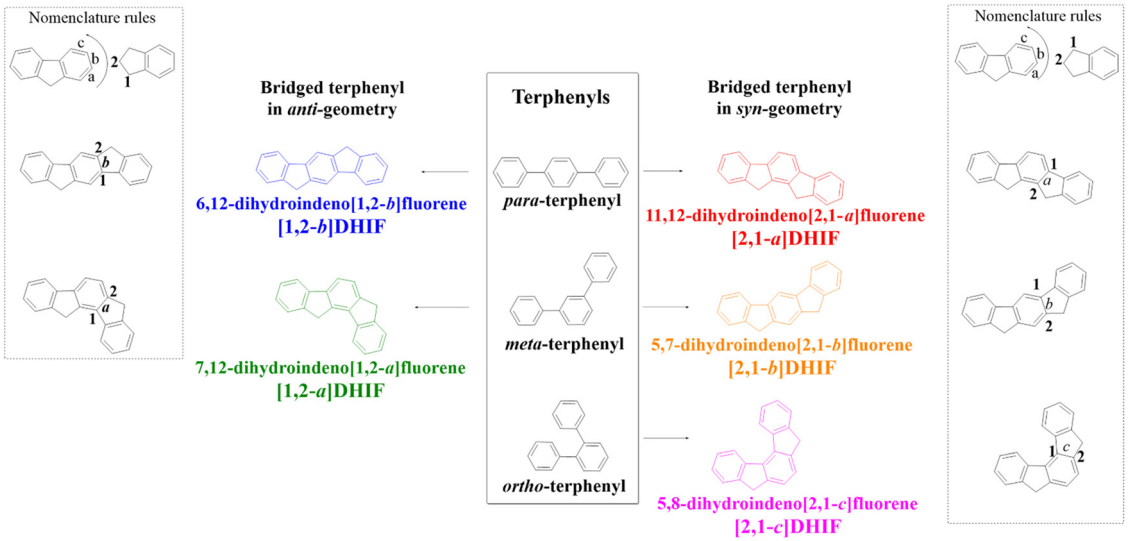

Scheme 1 The five DHIFs and their corresponding terphenyl regioisomers.

solar cells...). These design tactics have led, in many cases, to highly efficient materials and high performance devices. This fragment has therefore been widely investigated in organic electronics.

A second isomer in the series, namely 11,12-dihydroindeno[2,1-*a*]fluorene (**[2,1-*a*]DHIF**) is also constructed on a bridged *para* terphenyl core possessing nevertheless a *syn* geometry. This specific geometry has been notably used to tune the electronic properties and this isomer has emerged as a promising scaffold to obtain a stable blue emission used to modulate the electronic characteristics and this regioisomer has become an interesting building unit to reach a stable emission from conformationally-controllable intramolecular excimers.

Modification of the phenyl linkages from a *para* linkage to a *meta* linkage gives the '*meta* isomers', namely 7,12-dihydroindeno[1,2-*a*]fluorene (**[1,2-*a*]DHIF**) with an *anti* geometry and 5,7-dihydroindeno[2,1-*b*]fluorene (**[2,1-*b*]DHIF**) with a *syn* geometry. The last isomer in this family is 5,8-dihydroindeno[2,1-*c*]fluorene (**[2,1-*c*]DHIF**), which possesses a central *ortho* terphenyl backbone and a *syn* geometry. This isomer, due to its *ortho* linkage, offers a unique example which induces a particular helicoidal turn of the DHIF core. For these three isomers, the strong impact of both the linkage (*meta* and *ortho*) and the geometry (*syn*/*anti*) on the electronic properties has been particularly highlighted over the years. This review discusses how these fragments have been used in the construction of organic semiconductors for different OE devices. It will be notably shown how the positional isomerism is a powerful tool to tune the electronic properties, which in turn also has huge consequences on the device performance.

1. Introduction

Bridged oligophenylenes are a key class of organic semiconductors in organic electronics (OEs). Fluorene, which is a biphenyl bridged by a carbon atom, is the leader of this class of organic materials. It has led to formidable advances in organic light-emitting diodes (OLEDs, for a brief history of OLEDs, see ref. 1) due to the wide diversity of oligomers,[2–7] homo-polymers[8–12] or copolymers synthesized.[13–16] With a more extended conjugation, dihydroindenofluorenes (DHIFs) belong to the family of bridged terphenyls and can be viewed as the fusion of a fluorene unit with an indene fragment fused at different positions of the fluorene. The DHIF family presents five positional isomers (Scheme 1). They possess three different phenyl linkages (*para*/*meta*/*ortho*) and two different ring bridge arrangements (*anti*/*syn*).

In the DHIF family,[17,18] each isomer is described with a set of numbers and a letter as nomenclature. As depicted in Scheme 1, the letter corresponds to the edge of the indene/fluorene fusion (*a*, *b* or *c*) and the numbers correspond to the orientation of the indene group *vs.* the fluorene (1,2 or 2,1). Both **[1,2-*a*]DHIF** and **[1,2-*b*]DHIF** exhibit an *anti*-relationship between the methylene bridges whereas **[2,1-*a*]DHIF**, **[2,1-*b*]DHIF** and **[2,1-*c*]DHIF** exhibit a *syn*-relationship.

Thus, 6,12-dihydroindeno[1,2-*b*]fluorene (*para–anti* **[1,2-*b*]DHIF** in blue, Scheme 1) is built on a *para*-terphenyl core and possesses an *anti*-geometry. For the last 20 years, this regioisomer has been largely studied and a lot of organic semiconductors based on this [1,2-*b*]DHIF core have been synthesized, studied and used as an active material in different OE devices (fluorescent and phosphorescent organic light-emitting diodes, organic field-effect transistors (OFETs) and solar cells). 11,12-Dihydroindeno[2,1-*a*]fluorene (*para–syn* **[2,1-*a*]DHIF** in red) is also built on a bridged *para*-terphenyl core but possesses *syn*-geometry. This core has been significantly less studied despite its singular geometry, which has been notably used to tune the electronic properties.[19–22] Modification of the π-system from *para*- to *meta*-terphenyl provides the two *meta* isomers, 7,12-dihydroindeno[1,2-*a*]fluorene (*meta-anti* **[1,2-*a*]DHIF** in green, Scheme 1) and 5,7-dihydroindeno[2,1-*b*]fluorene

(*meta–syn* **[2,1-*b*]DHIF** in orange, Scheme 1). As for **[2,1-*a*]DHIF**, these fragments have been far less used in OE devices than **[1,2-*b*]DHIF**. However, the strong impacts of both the linkage and the geometry on the electronic properties of **[1,2-*a*]DHIF** and **[2,1-*b*]DHIF** derivatives have been particularly highlighted over the years.[23–27] There is another positional isomer in the family of DHIF, namely 5,8-dihydroindeno[2,1-*c*]fluorene (**[2,1-*c*]DHIF** in pink, Scheme 1), which possesses a central *ortho*-terphenyl backbone and a *syn*-geometry. This isomer has also been scarcely used to construct organic semiconductors despite its interesting *ortho* linkage, which induces a particular helicoidal turn of the DHIF core.

In addition, in the present review, our interest is focused on the use of organic semiconductors constructed on the five DHIF cores in different electronic devices. In fact, polymers based on DHIF cores are also numerous in the literature;[28] however most of them are based on the [1,2-*b*]-DHIF core. Additionally, the literature also reports a huge number of DHIF derived oligomers and copolymers. Due to the diversity of these materials, their physicochemical properties are broad[29] and some of them have been used in different organic electronic devices.[30,31] The purpose of this review is to highlight the key synthetic routes, the physicochemical properties and the uses of the molecules belonging to the five DHIF families and not on their oligomers, polymers or copolymers.

As **[1,2-*b*]DHIF** is the most investigated isomer in the literature to date, the first part of this review will be dedicated to the description of around 70 [1,2-*b*]DHIF-derived organic semiconductors and their integration in different OE devices. The second part will be dedicated to the [2,1-*a*]DHIF-based organic semiconductors. The review will end with a third part describing modification of the DHIF core by different linkages in [1,2-*a*]DHIF-, [2,1-*b*]DHIF- and [2,1-*c*]DHIF-based organic semiconductors. The analysis of the effects of the different linkages on the electronic properties and particularly on the triplet energy will be discussed. A structure–property relationship approach is presented all along the review in order to highlight the impact of structural modification on the physicochemical properties.

It should be noted that several accounts and reviews have discussed DHIFs in recent years.[17,18,27,31] In 2022, Usta and Fachetti reported a review on DHIF derivatives for electronics. This review was more centred on OFET and OPV devices and incorporated polymers.[31] An account was also dedicated, five years ago, to antiaromatic indenofluorenes by Haley's group.[17]

2. Dihydroindeno[1,2-*b*]fluorenyl-based organic semiconductors

2.1. A brief overview of [1,2-*b*]DHIF synthesis and the main physicochemical properties

To our knowledge, the first synthesis of **[1,2-*b*]DHIF** was reported in 1951,[32] and since this first synthesis, many different routes have been described (see Scheme 2).[33–39] As shown in Scheme 2, the corresponding diketone **[1,2-*b*]IF(=O)$_2$** is an important intermediate in these routes. This fragment, due to its electron withdrawing behaviour, is also a very important building unit widely used in electronic devices as detailed below.

Looking chronologically to the different accesses to **[1,2-*b*]DHIF** (Scheme 2), Deuschel described in 1951,[32] the condensation of *para*-xylene **1** and cyclohexene **2** in (2,5-dimethyl-1,4-phenylene)dicyclohexane **3** in 67% yield followed by its direct aromatisation-cyclization in **[1,2-*b*]DHIF** (20% yield) or by a three steps aromatization/cyclization/dechlorination sequence (**3** → **4** → **5** → **[1,2-*b*]DHIF**) (18% yield). In 1960, a novel access to **[1,2-*b*]DHIF** from the macrocycle **6** was described in two steps *via* the hexahydroindeno[1,2-*b*]fluorene **7**.[33]

The first access to **[1,2-*b*]DHIF** *via* the reduction of its diketone **[1,2-*b*]IF(=O)$_2$** was described in 1968 by Chardonnens and Salamin.[34] As the reduction of the dione is not the limiting

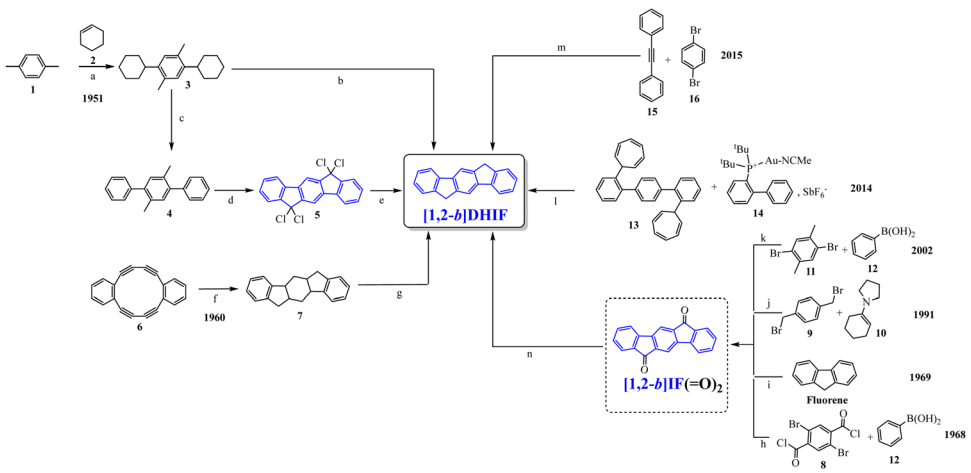

Scheme 2 Different approaches to [1,2-*b*]DHIF described in the literature from 1951 to 2015.[28–35] (a) $AlCl_3$, 0 °C; (b) Pd/C, 205 °C; (c) Pd/C cat, 280 °C; (d) Cl_2; (e) Zn, pyridine/AcOH; (f) Na, NH_2, THF; (g) 15% Pd/C, 320 °C; (h) Pd(II) palladacycle, PhMe, K_2CO_3, 55 °C then DMA, 120 °C, (i) in 5 steps *via* the 2-iodo-fluorene, then 2-iodofluorenone, then *ortho*-tolyl-fluorenone, then *ortho*-carboxyphenyl-fluorenone; (j) dioxane, reflux under N_2 then solvent evaporation; (k) in 3 steps: water, K_2CO_3, Bu_4NBr, $Pd(OAc)_2$, 70 °C leading to **4** then $KMnO_4$, pyridine water leading to terphenyl-2,5-carboxylic acid and finally H_2SO_4 25 °C; (l) DCE, 120 °C; (m) in 2 steps: $PdCl_2$, DPPE, DBU, CsOPiv, dioxane in a sealed tube, heating for 24 h then KOH, *t*-BuOK, N_2H_4/H_2O and 18-crown-6, heated for 12 h.

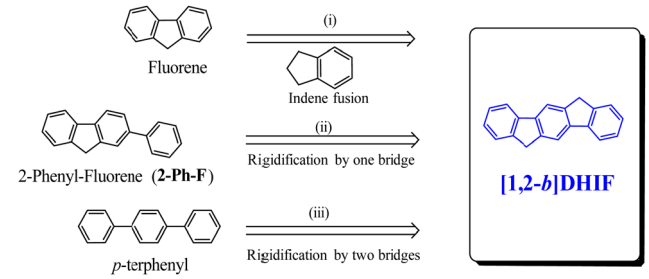

Scheme 3 **[1,2-*b*]DHIF** and the three model compounds used to discuss its main physicochemical properties.

step (classically the yield is reported between 75 and 95%), the access to **[1,2-*b*]IF(=O)$_2$** has been the subject of intense scouting (from **8** + **12**, from fluorene, from **9** + **10** or from **11** + **12**)[34–37] and the yield has been increased from 13% (**8** → **[1,2-*b*]IF(=O)$_2$**) in the initial work of Chardonnens[34] to 84% with the more efficient access (**11** + **12** → **[1,2-*b*]IF(=O)$_2$**) described, in 2002, by Wang's group.[37]

In 2014, direct access to **[1,2-*b*]DHIF** was described through double annulation of 2,2″-di(cyclohepta-2,4,6-trien-1-yl)-1,1′:4′,1″-terphenyl **13** using a cationic gold complex **14**[38] with 40% yield. Finally, in 2015, another access to **[1,2-*b*]DHIF** was published through a palladium-catalyzed reaction of diphenylethylene **15** and *para*-dibromobenzene **16**[39] with 50% yield.

A brief overview of **[1,2-*b*]DHIF** physicochemical properties, taken from the literature, is summarized below. This is an important step before describing the different organic semiconductors built on this core. As shown in Scheme 3, **[1,2-*b*]DHIF** may be viewed either as (i) the fusion of a fluorene unit with an indene fragment, (ii) the addition of a carbon bridge to a 2-phenyl-fluorene (**2-Ph-F**) or (iii) the addition of two carbon bridges to a *p*-terphenyl. Comparing the properties of **[1,2-*b*]DHIF** with those of the three fragments (summarized in Table 1) appears then relevant.

The thermal analysis using thermogravimetry (TGA) indicates for **[1,2-*b*]DHIF** a decomposition temperature @ 5% mass loss (T_d) of 200 °C.[40] This T_d is higher than that measured for *p*-terphenyl (176 °C)[24] indicating the beneficial effect of the two bridges on the thermal stability. It is known that the rigidification by carbon bridges increases the thermal stability, particularly the T_d.[24,41,42]

The structural characteristics of **[1,2-*b*]DHIF** are described in Fig. 1 (CCDC 779934, grown from CH_2Cl_2/MeOH).[43] **[1,2-*b*]DHIF** possesses an extended central core of 11.05 Å long, a distance of 5.77 Å between its two methylene bridges. The two external phenyl rings are in two parallel planes distant from 0.409 Å and show a small angle of 1.5° with the central phenyl ring. The **[1,2-*b*]DHIF** core is therefore almost perfectly flat. The packing of **[1,2-*b*]DHIF** occurs only *via* intermolecular carbon-hydrogen short interactions (Fig. 1-right).

The absorption spectrum of **[1,2-*b*]DHIF** in CH_2Cl_2,[40] presents a low absorption energy band peaking at 334 nm, showing an optical gap of 3.61 eV. Looking at the absorption spectra of the model compounds (recorded in cyclohexane, Fig. 2, left), a 33 nm redshift of the absorbance is observed from 277 nm for *p*-terphenyl to 310 nm for **2-Ph-F** signing the effect of the rigidification of the conjugated terphenyl core by the addition of one bridge. Note that both spectra remain large and ill-defined due to the rotation of one or two phenyl units. The comparison of fluorene and **2-Ph-F** clearly shows the impact of the addition of one phenyl unit, namely a loss of structuration and a 9 nm red-shift. The introduction of the second bridge in **[1,2-*b*]DHIF** leads to an additional 24 nm red-shift from **2-Ph-F** and the spectrum appears to be more defined translating the rigidification of the system.

The emission spectrum of **[1,2-*b*]DHIF** (in decaline or DCM) presents several emission bands peaking at 339, 347 and 356 nm with a fluorescence quantum yield of 0.73 reported

Table 1 Physicochemical properties of **[1,2-*b*]DHIF**[40] and of model compounds *p*-terphenyl, **2-Ph-F** and fluorene

	p-Terphenyl[24]	**2-Ph-F**	**[1,2-*b*]DHIF**	Fluorene
T_d (°C)	176	—	200[40]	—
$\lambda_{abs}(\varepsilon)$ (nm) ($\times 10^4$ L mol^{-1} cm^{-1})	277(3.16) (CHX)	289(3.23), 310(2.68) (CHX)[44]	328, 334 (CH_2Cl_2)[40] 333 (6.76) (Decaline)[37]	265, 290, 301 (CH_2Cl_2)[45] 272(1.39), 290(0.63), 294(0.53), 301(0.93) (CHX)[44]
λ_{em} (nm)	325, 339	329, 343 (CHX)[44]	339, 347, 356 (CH_2Cl_2)[40] 340, 356 (Decaline)[37]	310 (CH_2Cl_2)[45] 303, 310 (CHX)[44]
$\varnothing_{sol}$	0.93 (CHX)[46]	0.97 (CHX)[44]	0.61 (Decaline)[40] 0.73 (Decaline)[37]	0.88 (CHX)[44]
		0.91 (CHX)[46]	0.90 (CHX)[46]	0.80 (CHX)[46]
HOMO (eV)				
from electrochemistry	−5.96	−5.72 (CH_2Cl_2)[44]	−5.62 (CH_2Cl_2)[40]	−5.91 (CH_2Cl_2)[40,44]
from calculation	−6.13	−5.90[44]	−5.43[40]	−5.81[40]
LUMO (eV)				
from electrochemistry	−2.00	−1.92 (DMF)[44]	−1.99 (DMF)[40]/−2.16 (DMF)[37]	−1.69 (DMF)[40]
from calculation	−1.40	−1.55[44]	−1.13[40]	−0.77[40]
ΔE (eV)				
from optical data	4.03	3.76[44]	3.61[40]/3.71 (Decaline)[37]	3.97 (CH_2Cl_2)[40]
from electrochemistry	3.96	3.80[44]	3.63[40]/3.85[37]	4.19[40]
from calculation	4.44	4.35[44]	4.30[40]	5.04[40]
E_{T1} (eV)				
from optical data	2.55	2.57[44]	–	2.93[44]
from calculation	2.67	2.40[44]	—	2.72[44]

CHX: cyclohexane, DMF: *N*,*N*-dimethylformamide.

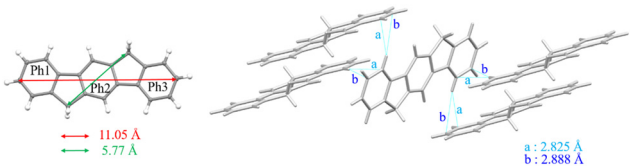

Fig. 1 X-Ray structure of **[1,2-*b*]DHIF** from CCDC 779934 (grown from CH_2Cl_2/MeOH).[43]

by Wang and coworkers[37] or of 0.61 reported by Poriel and coworkers.[40] A small Stokes shift is observed between the absorption and fluorescence spectra indicating the high rigidity of the molecule with very weak rearrangements at the excited state. Comparing the fluorescent spectrum of the *p*-terphenyl with the first band peaking at 325 nm, to that of **2-Ph-F** observed at 329 nm, one can note a red shift of 4 nm due to the presence of one bridge. Then, a red shift of 10 nm is observed from 329 nm for **2-Ph-F** to 339 nm for **[1,2-*b*]DHIF** indicating the influence of a second bridge. It is known that there is a planification of the pendant phenyl ring in the first excited state explaining the similitude of the fluorescent spectra of **[1,2-*b*]DHIF** and **2-Ph-F**.[24] The impact of the bridges on the optical properties and particularly on the emission characteristics is discussed in other reports.[23,24,47]

The electrochemical properties of **[1,2-*b*]DHIF** have also been widely investigated in previous studies.[48] As shown in Fig. 3, its electrochemical oxidation (CH_2Cl_2-Bu_4NPF_6 0.2 M) presents between 0.0 and 2.0 V (*vs.* Fc/Fc^+) two successive oxidation waves with maxima at 0.9 and 1.6 V (Fig. 3A). The first oxidation process is reversible (Fig. 3B). However, the oxidation in a potential range reaching the second oxidation process *E*2 caused the formation of insoluble electroactive deposits on the working electrode surface visible for example in Fig. 3C by the appearance and the growth of new redox waves (Ian/Icat and IIan/IIcat) in addition to the *E*1 and *E*2 waves belonging to **[1,2-*b*]DHIF** oxidation. The deposit itself has a high electroactivity over a rather large potential range (0.35–1.25 V *vs.* Fc/Fc^+).[48] The polymer formation proceeds by carbon–

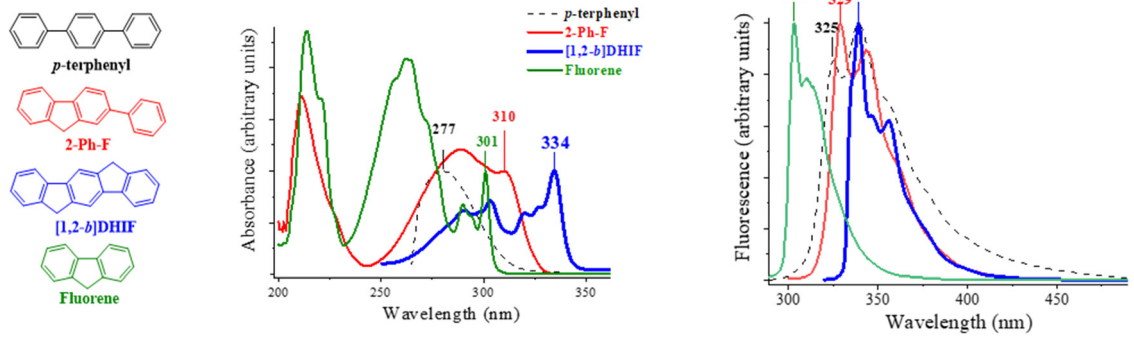

Fig. 2 Absorption (left) and emission (right) spectra of **[1,2-*b*]DHIF** (absorption/emission recorded in CH_2Cl_2/decaline) and of model compounds *p*-terphenyl, **2-Ph-F** and fluorene (all recorded in cyclohexane).

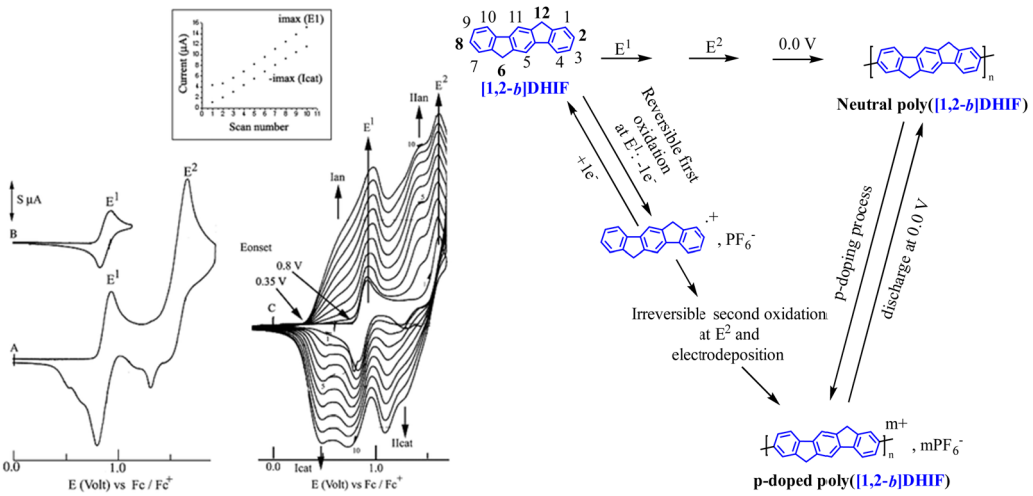

Fig. 3 Cyclic voltammetry in the presence of **[1,2-*b*]DHIF** (2×10^{-3} M) (A–C) in CH_2Cl_2 (Bu_4NPF_6 0.2 M); working electrode: Pt disk diameter 1 mm; sweep-rate 100 mV s^{-1}. The potential limit was of 0.0 to 1.75 V in A; 0.0 to 1.0 V in B; −0.2 to 1.73 V in C. The current scale *S* is equal to 2 in (A) and to 4 in (B) and in (C). The inset reports the I_{max} at E^1 and $-I_{max}$ at I_{cat} *vs.* the scan number. Adapted from ref. 48 with permission from the Royal Society of Chemistry.

carbon coupling involving the C2 and C8 carbon atoms of the DHIF core (Fig. 3, right) as classically observed for its shorter analogue fluorene.[49–52] To the best of our knowledge, this was, in 2008, the first example of an electrochemical synthesis of poly([1,2-*b*]DHIF).

2.2. [1,2-*b*]DHIF-based fluorescent organic light-emitting diodes (OLEDs)

Due to the above-mentioned characteristics and particularly the high quantum yield in the near UV region, **[1,2-*b*]DHIF** was first used as a building unit in fluorophores for the first generation of fluorescent OLEDs. Thus, many fluorophores have been constructed on this core through the substitution of the bridges and/or of the π-systems (Scheme 4).

In the following, the syntheses of the organic semiconductors are rather basic starting either from **[1,2-*b*]DHIF** or **[1,2-*b*]IF(=O)$_2$** and will not be described in detail as the access of the two starting molecules have been discussed above. However, synthetic details will be presented for organic semiconductors obtained by other more sophisticated routes.

[1,2-*b*]-1 to **[1,2-*b*]-15** have been used as fluorescent emitting layers (or as the hole-transporting layer (HTL) for **[1,2-*b*]-15**) in OLED devices, whose performances will be compared in order to draw a structure/properties/device performance map. The basic single-layer devices (SL-OLEDs) are constructed with the simple anode/emitting layer (EML)/cathode structures (with ITO or ITO/ PEDOT:PSS as the anode and Ca, Al or LiF/Al as the cathode). Such simplified devices have been investigated more and more recently.[53] The structure of the other devices constructed with additional layers named Multilayer OLED (ML-OLED) are detailed in Table 2 together with all the device performances.

The first OLED using a molecular emitter (non-polymeric structure) based on the [1,2-*b*]DHIF core was described in 2005,[54] 54 years after the first synthesis of **[1,2-*b*]DHIF**[32] translating the growing interest for this fragment in OE. **[1,2-*b*]-1** (see the molecular structure in Scheme 4) is based on the central [1,2-*b*]DHIF core substituted at its C2 and C8 carbon atoms by two 2-thienyl units. **[1,2-*b*]-1** was synthesized among a series of eight 2,8-diaryl-[1,2-*b*]DHIFs by Suzuki cross-coupling reactions with different arylboronic acids and **2,8-Br$_2$-[1,2-*b*]DHIF**, the latter being synthesized from **[1,2-*b*]DHIF** (route A, Scheme 5).[54]

The physicochemical properties of this series of 2,8-diaryl-[1,2-*b*]DHIF show that they all possess thermal stabilities higher than that of **[1,2-*b*]DHIF**. An important increase of T_d from 200 °C for **[1,2-*b*]DHIF**[40] to 411 °C for **[1,2-*b*]-1**[54] highlights the huge role played by the substituents on the thermal properties. The UV-vis absorption and emission of the eight compounds were also different to those of the central constituted **[1,2-*b*]DHIF** as the presence of the diaryl units induced an extension of the conjugation. In particular, the lowest energy absorption band of **[1,2-*b*]-1** is red shifted by 47 nm, from 334 nm for **[1,2-*b*]DHIF** (in CH_2Cl_2)[40] to 381 nm for **[1,2-*b*]-1** (in DMF).[54] A similar red shift of 57 nm of the emission spectrum is noted from 339 nm for **[1,2-*b*]DHIF** (in decalin)[40] to 396 nm for **[1,2-*b*]-1** (in DMF).[54]

The electroluminescent (EL) properties of **[1,2-*b*]-1** were evaluated in OLED1.[54] The architecture and the performance of all the devices presented below are summarized in Table 2. A moderate current efficiency (CE) of 1 cd A^{-1} and luminance of 1400 cd m^{-2} was reached. The EL spectrum was independent of

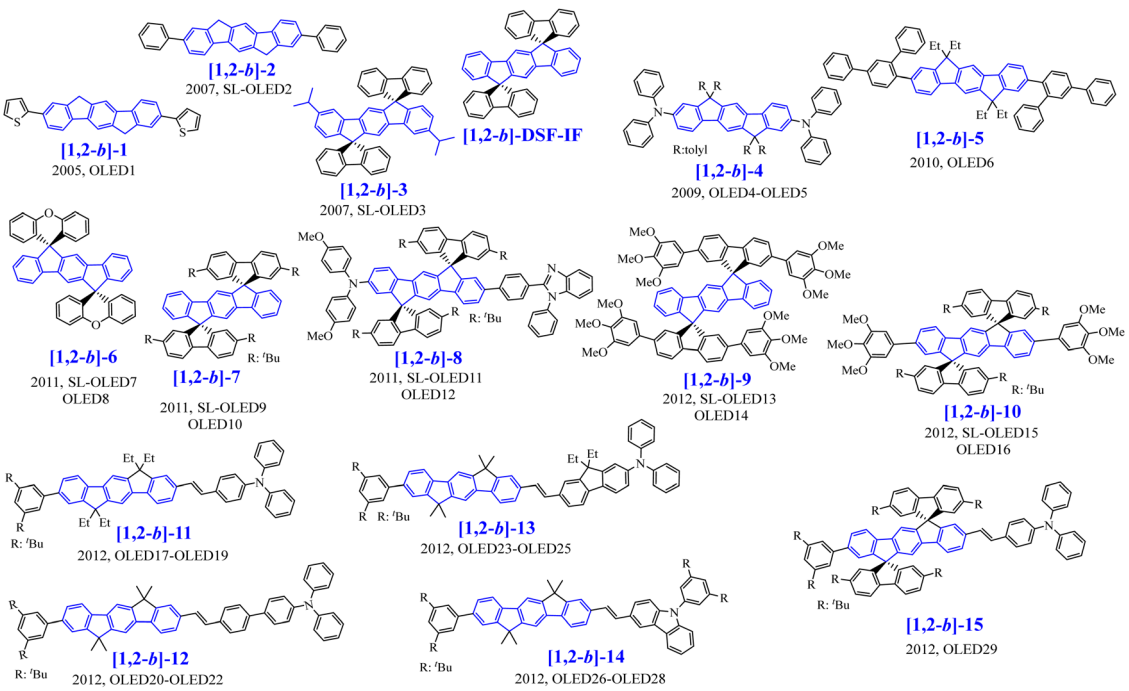

Scheme 4 **[1,2-*b*]DHIF**-based organic semiconductors used in fluorescent OLEDs.

Table 2 Performance of devices with [1,2-*b*]DHIF-based (**[1,2-*b*]-1**-**[1,2-*b*]-15**) as the EML or as another component

Device	Device architecture	V_{on} (V)	EQE (%)	CE (cd A^{-1})	PE (lm W^{-1})	Luminance (cd m^{-2})	λ_{max} (nm) CIE (x,y)	Ref.
OLED1	ITO/**[1,2-*b*]-1** (50 nm)/PBD(50 nm)/LiF(1.5 nm)/Al		—	1	—	1400 (@1600 A m^{-2})	— —	54
SL-OLED2	ITO/**[1,2-*b*]-2**/Al	20	—	—	—	150 (@35 V)	465, 500, 530 —	55
SL-OLED3	ITO/PEDOT:PSS/**[1,2-*b*]-3** (30 nm)/Ca	7	—	0.9	0.19	200 (@15 V & 220 A m^{-2})	399, 416, 483, 587 (0.21, 0.16)	40
OLED4	ITO/DPAInT2(20 nm)/**[1,2-*b*]-4**(20 nm)/TCTA(10 nm)/ DFBTA(60 nm)LiF/Al	2	3.3	11.4	11.2	64 000	— —	67
OLED5	ITO/DPAInT2(20 nm)/**[1,2-*b*]-4**(20 nm)/TCTA(10 nm)/ DFBTA (30 nm)/Alq3(30 nm)/LiF/Al	2.5	3.7	12.9	11	168 000	— —	67
OLED6	ITO/NPB(40 nm)/TCTA(20 nm)/**[1,2-*b*]-5**(30 nm)/Bphen (30 nm)/LiF(1 nm)/Al	11.2	2.19	0.76	0.27	—	430 (0.163, 0.073)	69
SL-OLED7	ITO/PEDOT:PSS/**[1,2-*b*]-6** (40 nm)/Ca	12.7	—	0.008	0.002	31	413, 590, 650 (0.18, 0.08)	58
OLED8	ITO/PEDOT:PSS/NPB(35 nm)/**[1,2-*b*]-6**(40 nm)/ BCP(10 nm)/ Ca	8	—	1	0.3	3 740	413, 438, 590, 650 (0.19, 0.14)	58
SL-OLED9	ITO/PEDOT:PSS/**[1,2-*b*]-7**(40 nm)/Ca	—	—	—	—	<2	— —	71
OLED10	ITO/PEDOT/NPB (35 nm)/**[1,2-*b*]-7** (40 nm)/Ca	9	—	0.005	—	25	415/436 nm	71
SL-OLED11	ITO/PEDOT:PSS/**[1,2-*b*]-8** (40 nm)/LiF(0.8 nm)/Al	5.2	—	0.13	—	320	470	71
OLED12	ITO/PEDOT:PSS/NPB/**[1,2-*b*]-8**(40 nm)/BCP/ LiF(0.8 nm)/Al	4.8	—	0.2	—	1000	465–472 (0.18, 0.28)	72
SL-OLED13	ITO/PEDOT:PSS/**[1,2-*b*]-9**(40 nm)/Ca	7.2	—	0.031	0.011	52	432 (0.24, 0.24)	22
OLED14	ITO/PEDOT:PSS/NPB(40 nm)/**[1,2-*b*]-9**(50 nm)/Ca	6.8	—	0.062	0.002	230	448 (0.25, 0.27)	22
SL-OLED15	ITO/PEDOT:PSS/**[1,2-*b*]-10**(40 nm)/Ca	10.8	—	0.016	0.004	50	452	22
OLED16	ITO/PEDOT:PSS/NPB(40 nm)/**[1,2-*b*]-10**(50 nm)/Ca	6.5	—	—	—	65	490	22
OLED17	ITO/DNTPD(60 nm)/NPB(30 nm)/**[1,2-*b*]-11** 3% in MADN (30 nm)/Alq3(20 nm)/LiF(1 nm)/Al	4.5	5.96	8.06	4.41	10 740	453, 481 (0.145, 0.194)	76
OLED18	ITO/DNTPD(60 nm)/NPB(30 nm)/**[1,2-*b*]-11** 5% in MADN (30 nm)/Alq3(20 nm)/LiF(1 nm)/Al	4.5	6.17	8.44	4.62	10 260	454, 482 (0.145, 0.198)	76
OLED19	ITO/DNTPD(60 nm)/NPB(30 nm)/**[1,2-*b*]-11** 7% in MADN (30 nm)/Alq3(20 nm)/LiF(1 nm)/Al	4.5	6.4	9.19	4.82	10 480	455, 483 (0.146, 0.212)	76
OLED20	ITO/DNTPD(60 nm)/NPB(30 nm)/**[1,2-*b*]-12** 3% in MADN (30 nm)/Alq3(20 nm)/LiF(1 nm)/Al	5.0	5.34	7.00	3.98	7541	451, 479 (0.149, 0.183)	76
OLED21	ITO/DNTPD(60 nm)/NPB(30 nm)/**[1,2-*b*]-12** 5% in MADN (30 nm)/Alq3(20 nm)/LiF(1 nm)/Al	5.0	5.73	7.84	4.11	7863	451, 474 (0.150, 0.194)	76
OLED22	ITO/DNTPD(60 nm)/NPB(30 nm)/**[1,2-*b*]-12** 7% in MADN (30 nm)/Alq3(20 nm)/LiF(1 nm)/Al	5.0	5.98	7.84	4.12	11 580	452, 480 (0.149, 0.193)	76
OLED23	ITO/DNTPD(60 nm)/NPB(30 nm)/**[1,2-*b*]-13** 3% in MADN (30 nm)/Alq3(20 nm)/LiF(1 nm)/Al	5.0	8.21	12.6	6.69	15 290	459, 488 (0.148, 0.241)	76
OLED24	ITO/DNTPD(6 0 nm)/NPB(30 nm)/**[1,2-*b*]-13** 5% in MADN (30 nm)/Alq3(20 nm)/LiF(1 nm)/Al	4.5	7.14	11.3	5.04	13 420	460, 489 (0.149, 0.250)	76
OLED25	ITO/DNTPD(60 nm)/NPB(30 nm)/**[1,2-*b*]-13** 7% in MADN (30 nm)/Alq3(20 nm)/LiF(1 nm)/Al	4.5	7.55	12.2	6.18	22 410	461, 491 (0.151, 0.257)	76
OLED26	ITO/DNTPD(60 nm)/NPB(30 nm)/**[1,2-*b*]-14** 3% in MADN (30 nm)/Alq3(20 nm)/LiF(1 nm)/Al	4.0	2.87	2.98	2.13	8767	438, 461 (0.153, 0.121)	76
OLED27	ITO/DNTPD(60 nm)/NPB(30 nm)/**[1,2-*b*]-14** 5% in MADN (30 nm)/Alq3(20 nm)/LiF(1 nm)/Al	4.0	2.82	3.13	1.77	8887	437, 463 (0.153, 0.133)	76
OLED28	ITO/DNTPD(60 nm)/NPB(30 nm)/**[1,2-*b*]-14** 7% in MADN (30 nm)/Alq3(20 nm)/LiF(1 nm)/Al	4.0	2.96	3.25	1.82	7952	437, 462 (0.153, 0.128)	76
OLED29	ITO/DNTPD(60 nm)/NPB(30 nm)/**[1,2-*b*]-15** 5% in MADN (30 nm)/Alq3(20 nm)/LiF(1 nm)/Al	4.0	7.3	10.2	5.4	25 100	458, 484 (0.14, 0.21)	77

2-(4-biphenylyl)-5-phenyl-1,3,4-oxadiazole (PBD); 4,4′,4″-tris(carbazol-9-yl)triphenylamine (TCTA); *N*1,*N*1′-(biphenyl-4,4′-diyl)bis(N1-phenyl-N4,N4 -di-*m*-tolylbenzene-1,4-diamine (DNTPD).

the voltage but presented a broad emission with parasite emission bands surely due to oxidation of the bridges. The device emitted a whitish yellow colour.

The performances of OLED1 were nevertheless higher than those of SL-OLED2, a device based on **[1,2-*b*]-2** (Scheme 4), similar to **[1,2-*b*]-1** with two phenyl units instead of two thienyl units, published two years later.[55] **[1,2-*b*]-2** was prepared using a similar route than that used for **[1,2-*b*]-1**[54] (Scheme 5-route A) but a second route (Scheme 5-route B) was also described. In this second approach,[55] the **2,8-Ph$_2$-[1,2-*b*]IF(=O)$_2$** was first synthesized by a coupling reaction between 4-biphenylboronic acid and dimethyl-2,5-dibromoterephthalate **17** in the presence of $Pd(PPh_3)_4$ leading to the pentaphenyl **18** followed by a cyclization step leading to **2,8-Ph$_2$-[1,2-*b*]IF(=O)$_2$**, which was then reduced to **[1,2-*b*]-2**. In this approach, the DHIF core was constructed in the last step, as the phenyl units were already grafted.

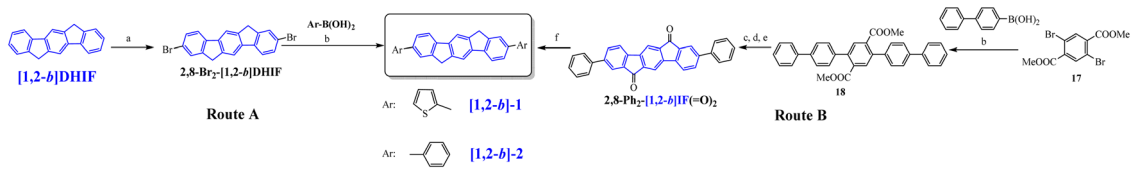

Scheme 5 Synthesis of **[1,2-*b*]-1** and **[1,2-*b*]-2**. (a) Br_2, TCE, RT, (b) $Pd(PPh_3)_4$ in 1-methyl-2-pyrrolidinone (NMP), 90 °C, (c) aq. NaOH solution (10%), 1,2-dimethoxyethane, 90 °C, (d) aq. HCl solution (20%), (e) Eaton's reagent, 90 °C, and f) KOH, diethylene glycol, H_2NNH_2, 200 °C.

T_d of **[1,2-*b*]-2**, 404 °C,[55] was very high and almost identical to that of **[1,2-*b*]-1**, 411 °C.[54] Its absorption spectrum was blue shifted by 31 nm (λ_{max}: 350 nm) compared to that of **[1,2-*b*]-1** (381 nm) translating a different π-conjugation extension (different aromaticity of phenyl and thienyl units). Similarly, its fluorescence spectrum with a maximum at 375 nm was blue shifted by about 20 nm compared to that of **[1,2-*b*]-1** (396 nm). The HOMO and LUMO reported for **[1,2-*b*]-2**, −5.2 and −2.0 eV were similar to those reported for **[1,2-*b*]-1** (the HOMO of **[1,2-*b*]-2** was nevertheless lower by 0.1 eV than that of **[1,2-*b*]-1** in accordance with the substituent effects indicated above). SL-OLED2 based on **[1,2-*b*]-2** emitted a green light with an extremely high threshold voltage (V_{on}) of 20 V and only reached a low luminance of 150 cd m^{-2} at 35 V, showing very weak OLED performances.

In 2006, our group described a novel route to construct the [1,2-*b*]DHIF core starting from diiodo-terphenyl derivatives (**19a-b**) and the 9-fluorenone **20**.[45] A novel generation of efficient violet emitters called dispirofluorene-indenofluorene (DSF-IF) was then reported.[27] **[1,2-*b*]-DSF-IF** and **[1,2-*b*]-3** belong to this family of emitters (Scheme 4). They possess three π-systems connected *via* two spiro carbon atoms. Their synthesis, as presented in Scheme 6, starts with diiodo-terphenyls **19a-b** involved in a lithium-iodine exchange followed by quenching with the 9-fluorenone **20** to give the corresponding diols, **21a-b**, which were finally converted to the corresponding DSF-IFs: **[1,2-*b*]-DSF-IF** and **[1,2-*b*]-3**. Each fluorenyl unit is in a plane perpendicular to that of the central [1,2-*b*]DHIF core. The specific architecture of these organic semiconductors was named "3π-2spiro", the association of 3 π-systems *via* 2 spiro-bridges.[56–62]

The X-ray analysis of **[1,2-*b*]-3**,[40] presented in Scheme 6, right, reveals that the central [1,2-*b*]DHIF core is almost perfectly flat and similar to that of **[1,2-*b*]DHIF** (Fig. 1) with small distortions probably caused by the two *iso*-propyl substituents. The angle measured between the central core and the fluorenyl units was ca 89° demonstrating the orthogonality between the central [1,2-*b*]DHIF core and the external fluorenyl π-systems.

[1,2-*b*]-3 and **[1,2-*b*]-DSF-IF** maintain the main physicochemical properties of **[1,2-*b*]DHIF**, with however higher thermal stability (T_d: 200 °C for **[1,2-*b*]DHIF**, 355 °C for **[1,2-*b*]-DSF-IF** and 382 °C for **[1,2-*b*]-3**).[40] This highlights the strong interest of the incorporation of spiro connected fragments. This feature was introduced by Salbeck *et al.* in the nineties.[41] HOMO and LUMO obtained from electrochemical experiments showed that (i) the HOMO of **[1,2-*b*]-DSF-IF** (−5.76 eV) and of **[1,2-*b*]-3** (−5.66 eV) were deepened compared to that of **[1,2-*b*]DHIF** (−5.62 eV) and that (ii) their LUMOs were lowered from **[1,2-*b*]DHIF** (−1.99 eV), to **[1,2-*b*]-3** (−2.07 eV) and **[1,2-*b*]-DSF-IF** (−2.17 eV). These effects may result from the electron-withdrawing impact of the spiro-linked fluorenyl units rendering the [1,2-*b*]DHIF core more difficult to oxidize and easier to reduce. These moderate effects through the spiro-bridges are induced by the "spiroconjugation".[63–66]

Both **[1,2-*b*]-3** and **[1,2-*b*]-DSF-IF** absorption spectra (CH_2Cl_2) present a low energy absorption band at respectively 348 nm and 345 nm and their emission spectra (cyclohexane) show bands at 351 and 347 nm respectively. The small Stokes shifts (2–3 nm) are consistent with the rigidity of the structures and with the high QY (0.66 and 0.62).

[1,2-*b*]-3 was used as the EML in SL-OLED3.[40] V_{on} was measured at 7 V and its luminance reached 200 cd m^{-2} at 15 V for a current density of 220 A m^{-2} showing the weak efficiency of the device. Its EL spectrum nevertheless possesses two main bands in the blue region (399 and 416 nm) and two others at 483 and 587 nm (CIE 1964 (0.21; 0.16)).

In 2009, the [1,2-*b*]DHIF-based donor–π–donor (D–π–D) **[1,2-*b*]-4**[67] (Scheme 4) was prepared from the 6,6,12,12-tetratolyl-6,12,dihydroindeno-[1,2-*b*]DHIF-fluorene **24**[68] (Scheme 7), itself obtained from the diethyl 2,5-dibromoterephthalate **22** and phenylboronic acid **12** *via* the terphenyl-2′,5′-diester **23**. The reaction of **23** with an excess of 4-methylphenyllithium

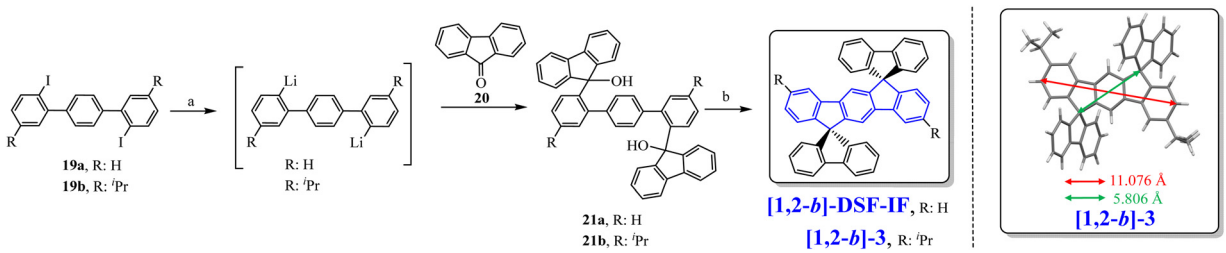

Scheme 6 Left: Synthesis of **[1,2-*b*]-DSF-IF** and **[1,2-*b*]-3**.^{n}BuLi, THF, −78 °C. (b) AcOH/HCl reflux. Right: X-Ray structure of **[1,2-*b*]-3**.

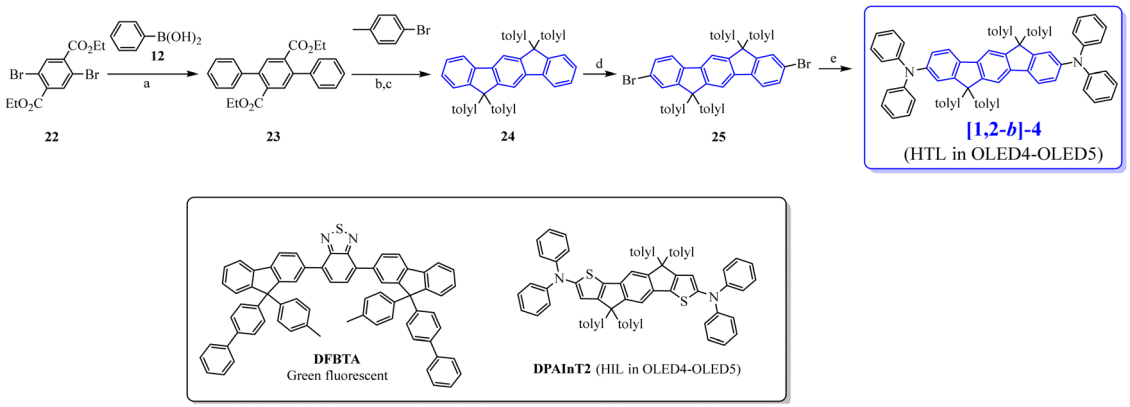

Scheme 7 Top: Synthesis of **[1,2-*b*]-4**. (a) $Pd(PPh_3)_4$, P^tBu_3, K_3PO_4, toluene, 60 °C, (b) ^{n}BuLi, THF, −78 °C, (c) boiling acetic acid/HCl, (d) Br_2, $FeCl_3$, $CHCl_3$, 0 °C, and (e) $Pd(OAc)_2$, $NHPh_2$, Na^tBuO, P^tBu_3, toluene, 60 °C. Bottom: The molecular structure of the green fluorescent emitter **DFBTA** and of the **DPAInT2** ETL used in OLED 4 and OLED 5.

(generated *in situ* by reacting 1-bromo-4-methylbenzene with *n*-BuLi at −78 °C) provided a diol, which underwent ring closure to generate **24**. **[1,2-*b*]-4** was then obtained through the selective bromination of **24** with 2.2 eq. of Br_2 in the presence of a catalytic amount of $FeCl_3$ (0.05 eq.) to afford the dibromo chromophore **25**. Pd-catalyzed C–N bond cross-coupling of **25** with diphenylamine gave **[1,2-*b*]-4**.

Compared to **[1,2-*b*]DHIF**, **[1,2-*b*]-4** presented a higher thermal stability with a T_d of 420 °C (200 °C for [1,2-*b*]DHIF[40]). The substitution at C2 and C8 by two donor units in addition to the substitution at C6 and C12 by four tolyl units led to a gap contraction of 0.69 eV from 3.61 eV for **[1,2-*b*]DHIF**[40] to 2.92 eV for **[1,2-*b*]-4**.[67] A high hole mobility (μ_h) of 10^{-3} cm^2 V^{-1} s^{-1} was measured for **[1,2-*b*]-4**[67] using time-of-flight measurements highlighting the significant role of the NPh_2 units.

[1,2-*b*]-4 was then used as the HTL in ML-OLEDs using as the EML the efficient green fluorescent emitter **DFBTA** (see the molecular structure in Scheme 7). Two devices were constructed (OLED4 and OLED5). Compared to similar OLEDs with a hole injection layer (HIL)/HTL of PEDOT:PSS/*N*,*N*′-Di(1-naphthyl)-*N*,*N*′-diphenyl-(1,1′-biphenyl)-4,4′-diamine (NPB) instead of **DPAInT2**/**[1,2-*b*]-4**,[67] OLED4 and OLED5 were slightly more efficient; the external quantum efficiency (EQE) increases from 2.6% to 3.3% in OLED4 and from 3% to 3.7% in OLED5. OLED5 exhibited the highest efficiency: V_{on} of 2.5 V, a maximum EQE of 3.7% (CE: 12.9 cd A^{-1}) and an extremely high luminance reaching 168 000 cd m^{-2}. This showed that DHIF derivatives could be efficiently used as the HTL when a judicious substitution is chosen.

In 2010, the group of Park[69] has prepared an extended **[1,2-*b*]DHIF** derivative substituted at C2 and C8 by two terphenyl groups, namely **[1,2-*b*]-5** (Scheme 4). Synthesis of **[1,2-*b*]-5** (Scheme 10, p. 13) starts from the dialkylation of **[1,2-*b*]DHIF** in **32** followed by dibromination giving **33** further involved in Suzuki coupling with **34** to provide **[1,2-*b*]-5** (Scheme 10). **[1,2-*b*]-5** showed a high T_g (179 °C), a key point for OLED applications, and also a high T_d (418 °C). The UV-vis absorption spectrum (THF) presented a maximum at 366 nm, red-shifted by 32 nm compared to **[1,2-*b*]DHIF**.[40] The optical gap of **[1,2-*b*]-5** (3.13 eV) was therefore more contracted than that of **[1,2-*b*]DHIF** (3.61 eV), indicating an extension of the conjugation in **[1,2-*b*]-5** due to the terphenyl substituents. Compared to the optical gap of **[1,2-*b*]-1** (3.1 eV),[54] with two 2-thienyl substituents, the extension of conjugation appears similar for **[1,2-*b*]-5** with two terphenyl groups. The emission spectrum of **[1,2-*b*]-5** presented a non-structured band, due to the rotation of the terphenyl fragments (λ_{max}: 405 nm, Stokes-shift: 39 nm). The authors measured the μ_h of films of **[1,2-*b*]-5** by the time-of-flight transient photocurrent techniques as 8.3×10^{-5} cm^2 V^{-1} s^{-1} (one order of magnitude lower than that of **[1,2-*b*]-4**).[67] This showed the importance of the substituents grafted to the IF core to improve the charge transport. OLED6 with **[1,2-*b*]-5** as the EML and 4,7-diphenyl-1,10-phenanthroline (Bphen) as the electron-transporting layer (ETL) reached an EQE_{max} of 2.19% and emitted a pure blue light with an EL_{max} centered at 430 nm with CIE coordinates of (0.163, 0.073) indicating an efficient electron injection from the cathode to the EML *via* the Bphen ETL.

Following our explorations on three dimensional [1,2-*b*] DHIF-based organic semiconductors, our group synthesized, in 2010, an organic semiconductor based on xanthenyl π-systems.[57] **[1,2-*b*]-6** (Scheme 4), possessing also a 3π-2spiro architecture, was constructed following two different routes presented in Scheme 8: the first from 2,2″-diiodoterphenyl **26** and xanthenone **27**, and the second starting from **[1,2-*b*]IF(=O)$_2$** in a one-step rearrangement reaction. Both routes provided **[1,2-*b*]-6** in moderate yield (50% from **26** and 35% from **[1,2-*b*]IF(=O)$_2$**).

The main physicochemical properties of **[1,2-*b*]-6**[57] may be first compared to those of **[1,2-*b*]DHIF** to investigate the impact of the xanthenyl substituents. Thanks to cyclic voltammetries,[70] $HOMO^{el}$/$LUMO^{el}$ were reported at −5.79/−2.15 eV, **[1,2-*b*]-6** displays almost identical energy levels compared to those of **[1,2-*b*]-DSF-IF** ($HOMO^{el}$/$LUMO^{el}$: −5.76/−2.17 eV),[40] indicating that xanthenyl units or fluorenyl units have similar electronic effects on the central [1,2-*b*]DHIF core. The gaps remain therefore similar for the three organic semiconductors (3.63/3.59/3.64 eV for **[1,2-*b*]DHIF**/**[1,2-*b*]-DSF-IF**/**[1,2-*b*]-6**) as the main

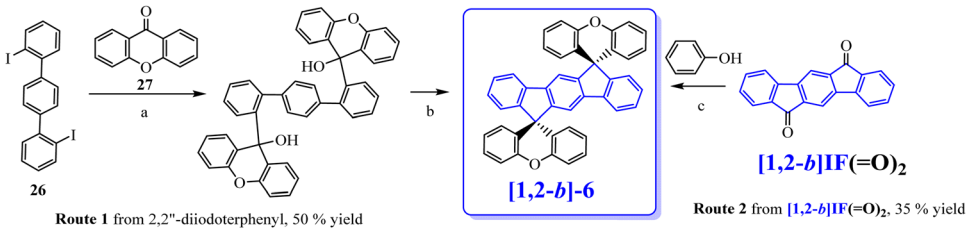

Scheme 8 Synthesis of **[1,2-*b*]-6**. (a) ^{n}BuLi, THF, −78 °C to RT, (b) CH_3CO_2H/HCl, 100 °C, and (c) $MeSO_3H$, 160 °C.

electronic properties in solution are imposed by the [1,2-*b*]DHIF core with only a moderate effect of the spiro connected units.

In absorption spectroscopy (cyclohexane), **[1,2-*b*]-6** presented a low energy band at 344 nm almost identical to that of **[1,2-*b*]-DSF-IF** (345 nm, see above).[40,45] The emission of **[1,2-*b*]-6** (cyclohexane) showed the first maximum at 347 nm is also similar to that of **[1,2-*b*]-DSF-IF** (347 nm, see above),[40,45] indicating that the optical properties of **[1,2-*b*]-6** and **[1,2-*b*]-DSF-IF** were both directed by their common [1,2-*b*]DHIF cores. For the two organic semiconductors, the Stokes shift was very small (3 nm) indicating rigid molecular structures.

[1,2-*b*]-6 was used as the fluorescent EML in devices of different architectures.[57,58] The performances of SL-OLED7 were extremely low (V_{on}: 12.7 V and maximum luminance of only 31 cd m^{-2}). OLED 8 was designed with *N*,*N*′-di(1-naphthyl)-*N*,*N*′-diphenyl-[1,1′-biphenyl]-4,4′-diamine (NPB) as the HTL and bathocuproine (BCP) as the hole blocking layer (HBL) inserted on both sides of **[1,2-*b*]-6**. Thus, for OLED8, V_{on} was measured at 8 V and the luminance reached 3 740 cd m^{-2}, showing the efficiency of this OLED architecture. A comparison of SL-OLED7 and OLED8 indicates that the addition of the HTL and HBL on both sides of the emitting layer (**[1,2-*b*]-6**) leads to a lower V_{on} (best charge injection in the device) and to a significant increase in the luminance (by a factor 100) indicating a more important exciton formation (best charges recombination in the EML) and relaxation. The EL spectra of the devices both showed the blue emission arising from **[1,2-*b*]-6**.

In 2011, our group synthesized a bipolar [1,2-*b*]DHIF-based emitter with a donor–π–acceptor (D–π–A) design[71] (**[1,2-*b*]-8**, Scheme 4) and compared its main physicochemical properties to those of its central π-system **[1,2-*b*]-7**[19] and of its donor–π–donor (D-[1,2-*b*]IF-D) and acceptor–π–acceptor (A-[1,2-*b*]IF-A) parent compounds[72] (molecular structure of A-[1,2-*b*]IF-A and of D-[1,2-*b*]IF-D in Scheme 9). Indeed the design of bipolar D–π–A materials with both electron and hole-transporting capabilities is of high interest for OLEDs, and particularly for simplified SL-devices.[25,53,71–73]

[1,2-*b*]-7 was first synthesized following a protocol similar to that used for **[1,2-*b*]-6** (Scheme 8, left) using 2,7-(^{t}Bu)$_2$-fluorenone instead of xanthenone **27**. Then **[1,2-*b*]-8** and its D–π–D and A–π–A parent compounds were prepared from **[1,2-*b*]-7** (see Scheme 9).[71,72] The D–π–A derivative, **[1,2-*b*]-8**, was prepared in four steps, from **[1,2-*b*]-7** by (a) a dibromation of the [1,2-*b*]DHIF central core leading to the 2′,8′-dibromo-derivative **28**, followed by (b) a selective Pd-catalyzed desymmetrization with 4-formylphenylboronic acid leading to **29**. The benzimidazolyl group of **30** was then constructed (c) through the condensation with *N*-phenyl-*o*-phenylenediamine in methoxyethanol (Scheme 9). Then **[1,2-*b*]-8** was obtained from **30** by the introduction of the dimethoxydiphenylamine unit. The overall yield from **[1,2-*b*]-7** was 10%. Similarly, **D-[1,2-*b*]IF-D** was obtained from **28** by the introduction of two dimethoxydiphenylamine units and **A-[1,2-*b*]IF-A** was obtained in two steps (**28** → **31** → **A-[1,2-*b*]IF-A**) following steps b and c.

Extension of the central [1,2-*b*]DHIF core of **[1,2-*b*]-7** by two electron donating units in **D-[1,2-*b*]IF-D** or by two electron accepting units in **A-[1,2-*b*]IF-A** leading to (i) an increase of the HOMO (without strong variation of the LUMO level) in **D-[1,2-*b*]IF-D** (HOMO^{el}/LUMO^{el}: −4.81/−2.02 eV[72]) or to (ii) a decrease of the LUMO (without strong variation of the HOMO level) in **A-[1,2-*b*]IF-A** (HOMO^{el}/LUMO^{el}: −5.55/−2.44 eV[72]), Fig. 4. Indeed, in these systems, the HOMO and LUMO levels are governed by the pending substituents and not by the DHIF core. **[1,2-*b*]-8** (HOMO^{el}/LUMO^{el}: −4.87/−2.35 eV[72]) gathers the characteristics of both **A-[1,2-*b*]IF-A** and **D-[1,2-*b*]IF-D**. Indeed, the substitution by both the donor and the acceptor units in **[1,2-*b*]-8**, leads to a decrease of the LUMO and an increase of the HOMO compared to **[1,2-*b*]-7**. It must be noted that **[1,2-*b*]-7** oxidation has been particularly studied both by cyclic voltammetries and spectroelectrochemical methods.[74] These studies showed the singular multielectronic oxidation of **[1,2-*b*]-7** with the first monoelectronic oxidation of the indenofluorenyl core followed by a second one electron oxidation and the reorganization of the dicationic charges on the two external fluorenyl units.

In absorption spectroscopy (cyclohexane), there was a shift of the lowest energy absorption band from 345 nm for **[1,2-*b*]-7** to 410 nm for **[1,2-*b*]-8**. Thus, **[1,2-*b*]-8** presented a ΔE^{opt} of 2.83 eV, strongly contracted compared to that of **[1,2-*b*]-7** (ΔE_{opt} = 3.49 eV). The emission spectrum of **[1,2-*b*]-8** showed fluorescence in the blue region (435 nm). This spectrum was significantly red-shifted by 86 nm compared to that of **[1,2-*b*]-7** (349 nm) due to both the intramolecular charge transfer and conjugation extension induced by the substituents. In addition, the emission spectrum of **[1,2-*b*]-8** is more resolved than its absorption one, indicating that, in the excited state, the bond linking the central DHIF core and the benzimidazolyl fragment gains some double bond character and therefore a more rigid/planar molecular structure. Finally, **[1,2-*b*]-8** also presented a very high quantum yield of *ca.* 0.97, in the blue region, ensuring therefore its potential as an efficient blue emitter.

OLED devices were first constructed with model compound **[1,2-*b*]-7** as the EML.[71] Both single (SL-OLED9) and double

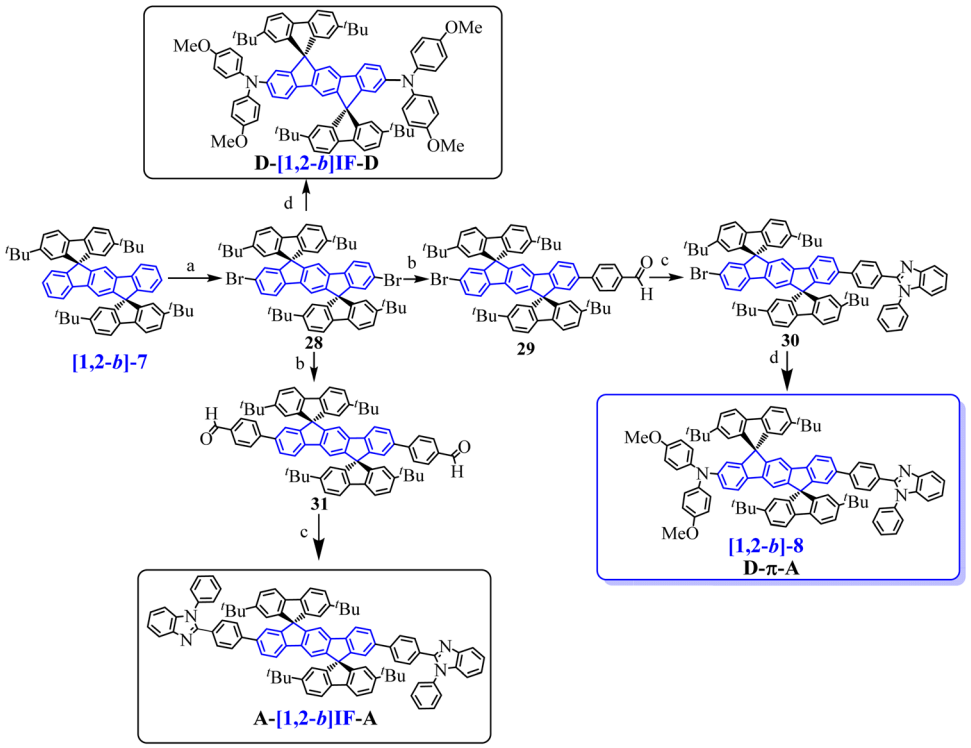

Scheme 9 Synthesis of **[1,2-*b*]-8**, and of its parent **A-[1,2-*b*]IF-A** and **D-[1,2-*b*]IF-D** derivatives. (a) Br_2, Na_2CO_3, I_2 (catalytic amount), CH_2Cl_2/water, RT, (90%); (b) $Pd_2(dba)_3$/P(^{t}Bu)$_3$, Na_2CO_3, 4-formylphenylboronic acid (1.4 eq. *vs.* **28** for **29** or 2 eq. *vs.* **28** for **31**), toluene/water, 100 °C; (c) methoxyethanol, *N*-phenyl-*o*-phenylenediamine, 120 °C; (d) $Pd(OAc)_2$, P(^{t}Bu)$_3$, ^{t}BuOK, 4,4′-dimethoxydiphenylamine, toluene, 100 °C.

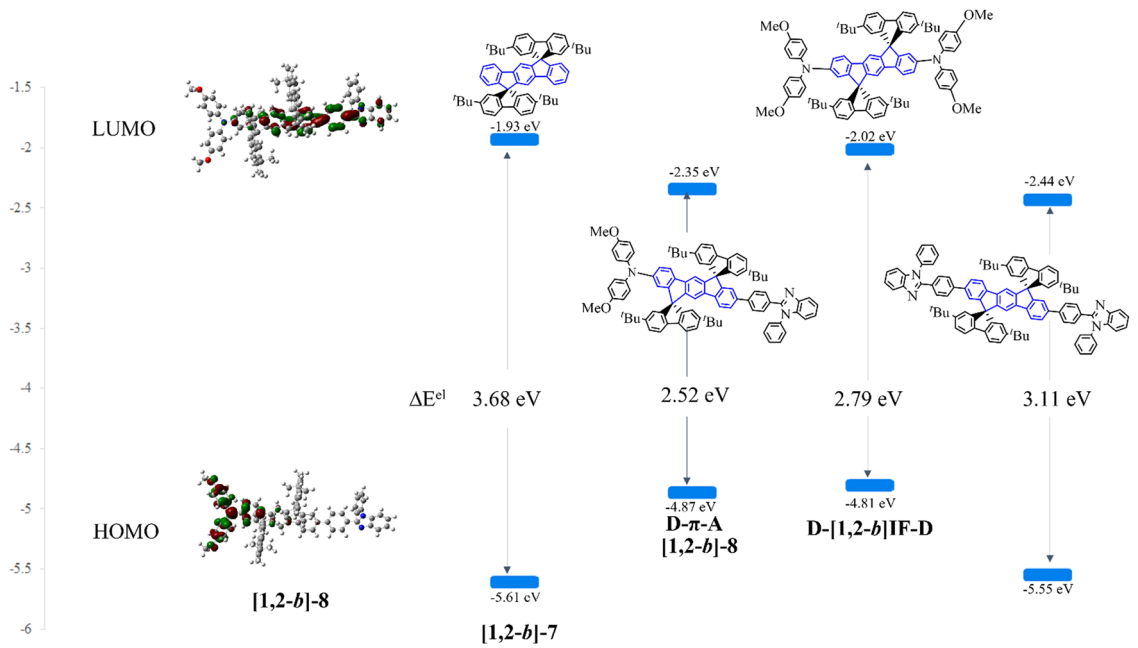

Fig. 4 Representation of the HOMO and LUMO energy levels obtained from electrochemical studies of different **[1,2-*b*]-**derivatives. Left: Representation of the electron density contour (HOMO and LUMO) obtained from DFT calculations for **[1,2-*b*]-8** (isovalue: 0.03 [e Bohr^{-3}]$^{1/2}$).

(OLED10) layer OLEDs displayed a very low performance translating the high difficulty to inject charges within the EML. Two OLEDs were then constructed using **[1,2-*b*]-8** as the EML, SL-OLED11 and OLED 12. Compared to the performance of SL-OLED9, SL-OLED11 appeared more efficient showing the interest of the D–π–A architecture of **[1,2-*b*]-8.** The performance of

SL-OLED11 remains however low reaching only 320 cd m^{-2} and a CE max of 0.13 cd A^{-1}. The performance was improved using multilayer stacking in OLED12[72] (1 000 cd m^{-2} and 0.2 cd A^{-1}).

In 2011, **[1,2-*b*]-9**[75] and in 2012, **[1,2-*b*]-10**[22] (Scheme 4) were synthesized and studied by our group. The HOMO/LUMO energy levels of **[1,2-*b*]-9** and **[1,2-*b*]-10** were compared to those of structurally related compounds: **[1,2-*b*]-DSF-IF** and **[1,2-*b*]-7** in order to highlight the key role played by the substituents on the electronic properties of the different organic semiconductors (Fig. 5).

The HOMO level obtained by cyclic voltammetries was increased by 0.27 eV from **[1,2-*b*]-DSF-IF** (−5.76 eV) to **[1,2-*b*]-9** (−5.49 eV) due to the incorporation of the 3,4,5-trimethoxyphenyl units, which extends the π-conjugation of the fluorene units. In **[1,2-*b*]-9**, the HOMO/LUMO energy levels are therefore governed by the "aryl-fluorene-aryl" core. For the same reason, the LUMO (calculated from the optical gap ΔE^{opt} and the HOMO) was decreased by 0.21 eV from **[1,2-*b*]-DSF-IF** (LUMO: −2.25 eV) to **[1,2-*b*]-9** (LUMO: −2.04 eV).

For **[1,2-*b*]-10**, the modulation of the HOMO and LUMO levels was associated with the extension of conjugation of the [1,2-*b*]DHIF central unit by the two 3,4,5-trimethoxyphenyl moieties. For this compound, both HOMO and LUMO were governed by the aryl-[1,2-*b*]DHIF-aryl core. Thus the HOMO level was increased by 0.18 eV from **[1,2-*b*]-7** to **[1,2-*b*]-10** and the LUMO level was decreased by 0.17 eV from **[1,2-*b*]-7** to **[1,2-*b*]-10** providing a gap contraction of 0.35 eV.

The UV-vis absorption spectrum of **[1,2-*b*]-10** presented a maximum at 345 nm whereas that of **[1,2-*b*]-9** was red-shifted by 17 nm (362 nm). The same trend was observed in emission spectroscopy (381 *vs.* 391 nm for **[1,2-*b*]-9** and **[1,2-*b*]-10**). The optical properties of **[1,2-*b*]-10** are fully governed by the central aryl-[1,2-*b*]DHIF-aryl moiety whereas those of **[1,2-*b*]-9** are governed by the two spiro-linked aryl-fluorene-aryl units.

SL-OLED13 and SL-OLED15 based on **[1,2-*b*]-9** and **[1,2-*b*]-10** reached very low performances (CE lower than 0.06 cd A^{-1}). The insertion of a NPB layer between the anode and the EML in OLED14 and in OLED16, slightly increases the performances which remain however very low (luminance reaching only 230 or 65 cd m^{-2} for OLED 14 or OLED16).

Four other non-symmetric [1,2-*b*]DHIF-derivatives, **[1,2-*b*]-11** to **[1,2-*b*]-14** (Scheme 4), were prepared, in 2012, by Lee and Yoon.[76] As shown in Scheme 10, all of them were obtained by a non-symmetric modification of the 2,8-dibromo-6,6,12,12-tetraethyl-6,12-dihydroindeno[1,2-*b*]fluorene **33** (obtained from **[1,2-*b*]-DHIF** as described before for the synthesis of **[1,2-*b*]-5**[69]). **33** was then monolithiated, followed by reaction with DMF to afford the monoformylated intermediate **35**, which was coupled with 3,5-di-*tert*-butylphenylboronic acid **36**. Finally, **[1,2-*b*]-11**-**[1,2-*b*]-14** were obtained by Horner–Wadsworth–Emmons reaction between **37** and the corresponding phosphonates **38a-38d** (Scheme 10).

Absorption spectra were only weakly modulated from **[1,2-*b*]-11** to **[1,2-*b*]-13** indicating the weak influence of the phenyl-vinylene/biphenyl-vinylene or fluorenyl-vinylene links between the diphenylamine and the [1,2-*b*]DHIF core in the three compounds. For **[1,2-*b*]-14**, a blue shift of 10 nm of the absorption spectrum related to **[1,2-*b*]-11** was noted due to the different influence of the triphenylamine in **[1,2-*b*]-11** and phenylcarbazole in **[1,2-*b*]-14**. The four fluorophores displayed a blue light with maxima at 464, 469, 480 and 429 nm for **[1,2-*b*]-11**-**[1,2-*b*]-14** respectively. The maximum was red-shifted from **[1,2-*b*]-11** to **[1,2-*b*]-13** indicating the extension of conjugation from **[1,2-*b*]-11** with one phenyl linker to **[1,2-*b*]-12** with a biphenyl linker and finally to **[1,2-*b*]-13** with one

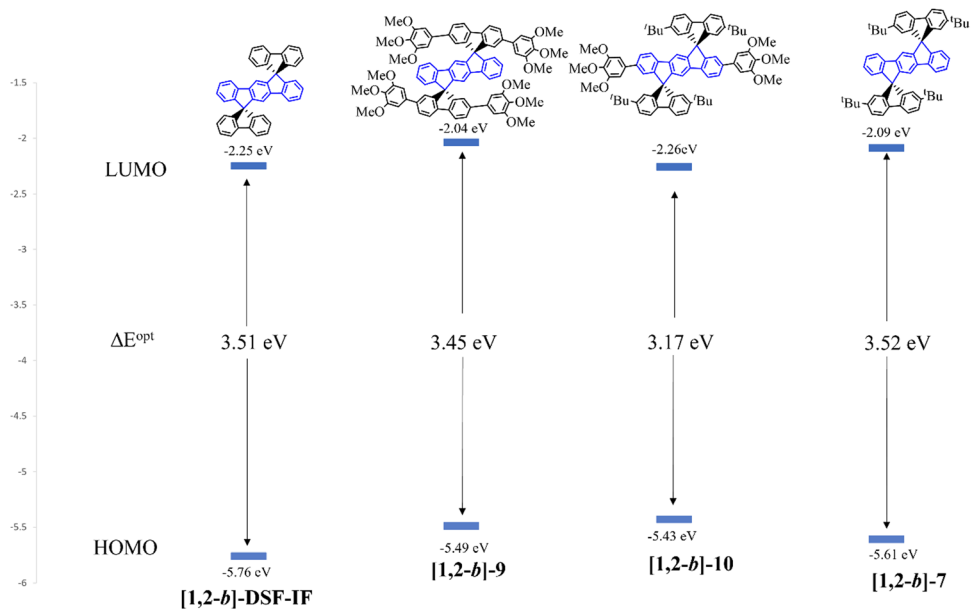

Fig. 5 HOMO/LUMO energy levels and optical gaps of different **[1,2-*b*]**-derivatives. HOMO levels were calculated from electrochemical studies and LUMO levels were calculated from the HOMO and the optical gap.[22,40,75]

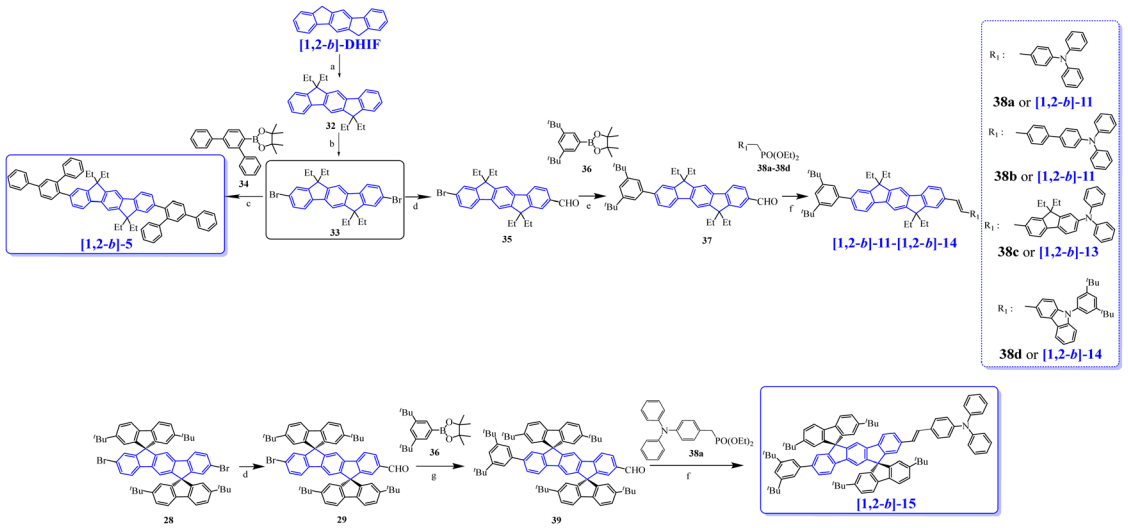

Scheme 10 Synthesis of **[1,2-*b*]-5** and **[1,2-*b*]-11** to **[1,2-*b*]-15**. (a) Bromoethane, $^{n}Bu_4NBr$, toluene, NaOH/Reflux; (b) Br_2, $FeCl_3$, $CHCl_3$; (c) $Pd(OAc)_2$,Et_4NOH, Ph_3P, toluene; (d) $^{n}BuLi$, DMF, THF, −78 °C; (e) $[Pd(PPh_3)_4]$, 2 M Na_2CO_3, ethanol, toluene; (f) $^{t}BuOK$, THF; (g) $Pd(PPh_3)_4$, Aliquat 336, K_2CO_3, toluene.

fluorenyl linker. **[1,2-*b*]-14** which contains a C3-substituted carbazole unit (disruption of the conjugation) showed a blue shift relative to **[1,2-*b*]-11**–**[1,2-*b*]-13**.

The four compounds were employed as emitters dispersed in a matrix of 2-methyl-9,10-bis(2-naphthyl)anthracene (MADN). In these devices (OLED17 to OLED28), the blue fluorophores were used to dope the MADN host in concentrations varying from 3 to 5 and 7%. The highest device performances were obtained with **[1,2-*b*]-13** as the dopant, either in 3% in MADN showing an EQE higher than 8.2% (OLED23) or in 7% in MADN with a luminance reaching 22 410 cd m^{-2} (OLED25). Performances of OLED17 to OLED28 were significantly higher than the performances of the non-doped OLEDs presented above (OLED1 to OLED16), showing the importance of using a host matrix to improve the device performance. All devices with **[1,2-*b*]-11** to **[1,2-*b*]-14** as the dopant displayed a low V_{on} of 4.0 to 5.0 V with blue emission for all the devices.

The same group also synthesized **[1,2-*b*]-15**[77] by an asymmetric modification of **28** (Scheme 10). Using this strategy, two different substituents were introduced, namely $Ph(^{t}Bu)_2$ and vinyl-TPA. Thus, the first monoformylation led to **29**, which was involved in C–C coupling with the boronic acid **36** leading to **39**. Then, a Horner-Wadsworth-Emmons reaction of **39** with the phosphonate **38a** afforded **[1,2-*b*]-15** with 11% yield from **28**.

[1,2-*b*]-15 physicochemical properties were similar to those of **[1,2-*b*]-11** showing that the main properties are governed by the same central extended [1,2-*b*]DHIF. **[1,2-*b*]-15** was also used as the dopant of MADN in OLED29. This device was a very high efficiency blue OLED reaching an EQE_{max} of 7.3% (CE_{max}/PE_{max}: 10.2 cd A^{-1}/5.4 lm W^{-1}) with a maximum luminance of 25 100 cd m^{-2} at 8.5 V. Compared to OLED18, OLED29 outperformed with an EQE increasing from 6.17 to 7.3% and a luminance increasing from 10 260 to 25 100 cd m^{-2}. The performance of OLED29 was the highest in the series (OLED17-OLED29) with the lower V_{on}, the highest luminance and an EQE of 7.3%. OLED23-OLED25 based on **[1,2-*b*]-13** were also very efficient (EQE between 7.14 and 8.21%) with however higher V_{on} and lower luminances.

2.3. [1,2-*b*]DHIF-based organic semiconductors used in organic field-effect transistors

Organic field-effect transistors have attracted great interest in the last 30 years due to their possible incorporation in full OE devices.[78–82] In the course of writing the present review, another review also dedicated to [1,2-*b*]DHIF fragments was published by Facchetti and Usta.[31] Some of the organic semiconductors presented in Scheme 11 have been described in this review with however a different view angle.

The development of [1,2-*b*]DHIF derivatives for OFET is described below starting from the first p-type OFET1 based on **[1,2-*b*]-1**[83] to electron-transporting n-type OFETs based on more efficient organic semiconductors (**[1,2-*b*]-16** to **[1,2-*b*]-42**) described in Scheme 11. The [1,2-*b*]DHIF core displays appealing characteristics for charge transport such as its extended π-conjugated backbone, which may favour π–π interactions. As exposed above, it can also be easily functionalizable either on the bridges or on the benzene rings, of great interest to tune the electronic properties such as HOMO/LUMO levels. In this part, we will describe the [1,2-*b*]DHIF derivatives, which have been used as active materials in OFETs (Table 3). As previously presented above for OLED devices, analysis of both the organic semiconductor physicochemical properties and the OFET performances will allow us to draw a structure/properties/device performance relationship map.

In 2006, a transistor based on **[1,2-*b*]-1** was reported.[83] **[1,2-*b*]-1** was used as the organic semiconductor in the top-contact/bottom-gate device exhibiting p-type transport with a high μ_h of 0.012 cm^2 V^{-1} s^{-1} and a threshold of −55 V (OFET1).

The same year, **[1,2-*b*]-2** was used in semiconductor/metal/semiconductor (SMS) transistors (a thin metal base located

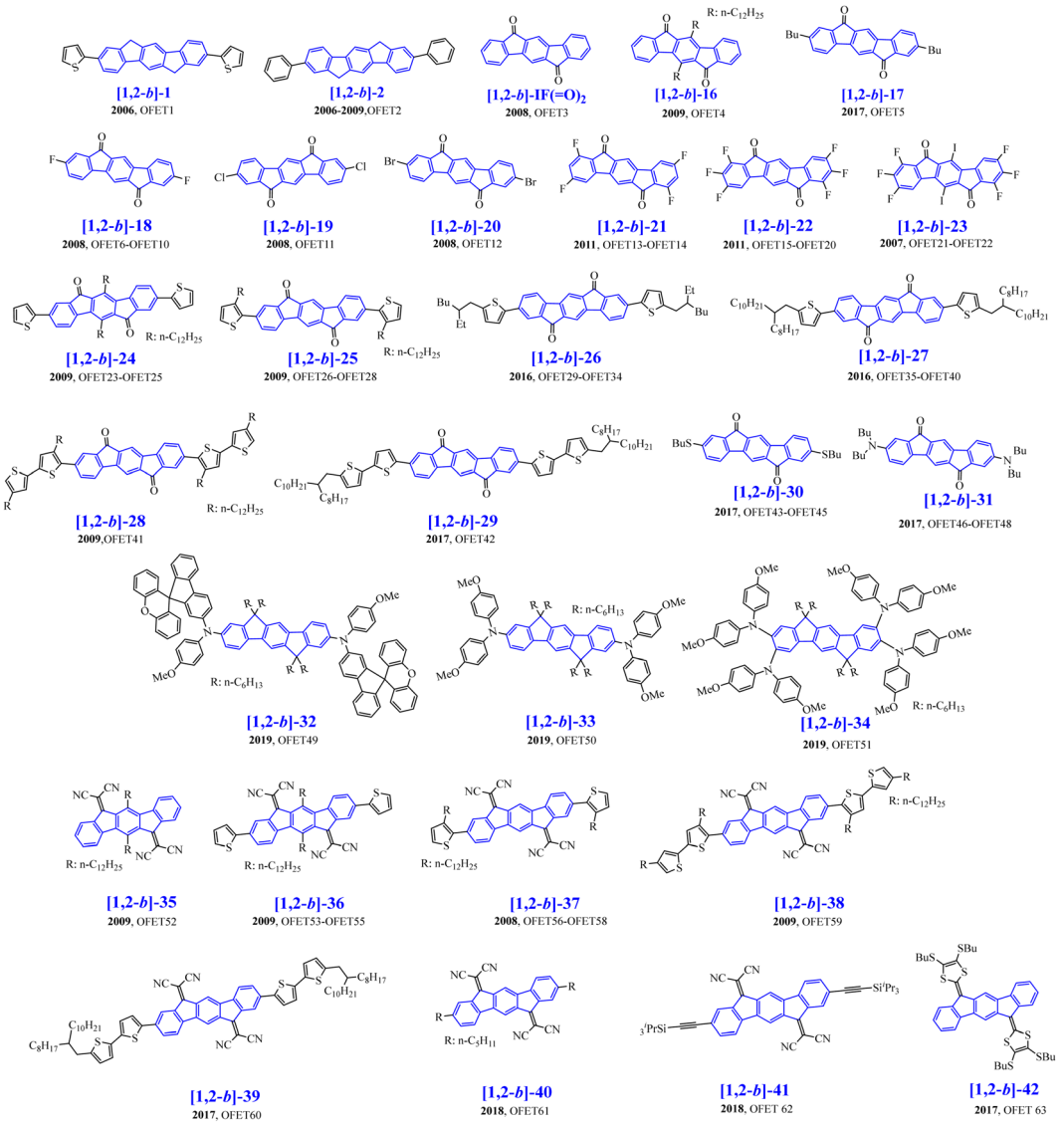

Scheme 11 **[1,2-*b*]DHIF**-based organic semiconductors used as the active material in OFET (**[1,2-*b*]-16**–**[1,2-*b*]-42**).

between two semiconductor layers, **[1,2-*b*]-2** and the collector). In this work,[84] it was shown that hybrid permeable-base transistors, operating with positive charges as the majority carriers can be obtained and possess a nearly ideal base transport factor. In 2007, a thin-film transistor (TFT) and SMS were fabricated and characterized by the same group.[55] **[1,2-*b*]-2** showed a weak n-type character from the TFT measurement, while SMS transistors using **[1,2-*b*]-2** behave like permeable-base transistors with low operating voltages in both common-base and common-emitter modes and a feature of current amplifications.

Finally, in 2009, the same group presented a permeable-base transistor consisting of **[1,2-*b*]-2** with a Ca/Al/Ca multilayer as the metal base and p-Si as the collector.[85] Playing with the thickness of Al, they have shown that the device presents common-base current gain and common-emitter current gain. This last gain of around 2 was independent of collector-emitter voltage and base current. All these first experiments showed the possibility of using **[1,2-*b*]-2** in different types of transistors and may be seen as a proof of concept.

In 2008, OFET3 based on **[1,2-*b*]IF(=O)$_2$**[37] was fabricated on SiO_2/Si substrates by thermal evaporation (SiO_2 gate dielectric was treated with hexamethyldisilane (HMDS)) in bottom-contact geometry.[86] However, these OFETs indicated a no-gate effect.

Then, differently substituted **[1,2-*b*]IF(=O)$_2$** were synthesized and used in different OFETs. To improve the processability of **[1,2-*b*]IF(=O)$_2$**, two dodecyl chains were first positioned on the central phenyl unit of **[1,2-*b*]-16**. Despite this, OFET4, based on a top-contact/bottom-gate device, showed no gate effect.[87] Similarly, the substitution of the C2 and C8 atoms of **[1,2-*b*]IF(=O)$_2$** by two *n*-butyl chains in **[1,2-*b*]-17** was tested[88] but no gate effect was observed in OFET5.

In 2008, different **[1,2-*b*]IF(=O)$_2$** substituted with two halogen atoms at C2 and C8: fluorine in **[1,2-*b*]-18**, chloride in

Table 3 Performance of devices with a [1,2-*b*]DHIF-based active layer in OFETs

Device	Device architecture	μ	I_{on}/I_{off}	V_T (V)	Ref.
OFET1	Top-contact/bottom gate device Si/SiO_2/HMDS/**[1,2-*b*]-1**/Au	p-type transistor μ_e: 0.012 $cm^2 V^{-1} s^{-1}$	—	−55	83
OFET2	SCO/metal/SCO permeable-base transistor GaIn/p-Si/Sn/**[1,2-*b*]-2**/PEDOT:PSS/Al	p-Type transistor	—	—	84
	OTFT transistor based on **[1,2-*b*]-2**	Weak n-type characteristic	—	—	55
	SCO/metal/SCO permeable-base transistor GaIn/p-Si/Sn/**[1,2-*b*]-2**/Au	Permeable-base transistors with low operating voltage Instability	—	—	55
	Vertical permeable-base hybrid transistor based on a multilayer metal base	Common-emitter current gain of 2, independent of collector-emitter voltage and base current, stable device	—	—	85
OFET3	Bottom-contact structure Si/SiO_2/HMDS/**[1,2-*b*]IF(=O)$_2$**)/Au	No-gate effect	—	—	86
OFET4	Top-contact/bottom gate device p^+-Si/SiO_2/**[1,2-*b*]-16**/Au	No-gate effect	—	—	87
OFET5	Top-contact/bottom gate device in glove box p-Si/SiO_2/OTMS/**[1,2-*b*]-17**/Au	No gate effect whatever the temperature	—	—	88
OFET6	Bottom-contact structure Si/SiO_2/HMDS/**[1,2-*b*]-18**/Au	n-type μ_{FET} μ_e: 0.17 $cm^2 V^{-1} s^{-1}$	2×10^7	69	86
OFET7	Top-contact structure Si/SiO_2/HMDS/**[1,2-*b*]-18**/Au	n-type μ_{FET} μ_e: 0.06 $cm^2 V^{-1} s^{-1}$	2×10^4	75	86
OFET8	Bottom-contact structure Si/SiO_2/**[1,2-*b*]-18**/Au	n-type μ_{FET} μ_e: 1.9×10^{-4} $cm^2 V^{-1} s^{-1}$	6×10^3	88	86
OFET9	Top-contact/bottom gate device n-Si/SiO_2/PS/**[1,2-*b*]-18**/Al/LiF	n-type μ_{FET} μ_e: 0.07 $cm^2 V^{-1} s^{-1}$	6.9×10^5	31.7	89
OFET10	Top-contact/bottom gate device n-Si/SiO_2/PS/**[1,2-*b*]-18**/Au	n-type μ_{FET} μ_e: 0.14 $cm^2 V^{-1} s^{-1}$	1.2×10^5	32.1	89
OFET11	Bottom -contact structure Si/SiO_2/HMDS/**[1,2-*b*]-19**/Au	n-type μ_{FET} μ_e: 0.018 $cm^2 V^{-1} s^{-1}$	1×10^7	56	86
OFET12	Bottom -contact structure Si/SiO_2/HMDS/**[1,2-*b*]-20**/Au	n-type μ_{FET} μ_e: 9.9×10^{-3} $cm^2 V^{-1} s^{-1}$	4×10^6	61	86
OFET13	Top-contact/bottom gate device n-Si/SiO_2/PS/**[1,2-*b*]-21**/Al/LiF	n-type μ_{FET} μ_e: 0.05 $cm^2 V^{-1} s^{-1}$	4.3×10^5	26.1	89
OFET14	Top-contact/bottom gate device n-Si/SiO_2/PS/**[1,2-*b*]-21**/Au	n-type μ_{FET} μ_e: 0.07 $cm^2 V^{-1} s^{-1}$	5.4×10^5	22.2	89
OFET15	Top-contact/bottom gate device n-Si/SiO_2/PS/**[1,2-*b*]-22**/Al/LiF	n-type μ_{FET} μ_e: 0.09 $cm^2 V^{-1} s^{-1}$	1.8×10^5	4.7	89
OFET16	Top-contact/bottom gate device n-Si/SiO_2/PS/**[1,2-*b*]-22**/Au	n-type μ_{FET} μ_e: 0.16 $cm^2 V^{-1} s^{-1}$	6.8×10^5	9.2	89
OFET17	Bottom gate-top contact OFET n-Si/SiO_2/NH_2-alkylsilane/**[1,2-*b*]-22**/Au	n-type μ_{FET} μ_e: 0.05 $cm^2 V^{-1} s^{-1}$	5.1×10^4	-56.8	90
OFET18	Bottom gate-top contact OFET n-Si/SiO_2/PS/**[1,2-*b*]-22**/Au	n-type μ_{FET} μ_e: 0.18 $cm^2 V^{-1} s^{-1}$	4.4×10^5	-15.5	90
OFET19	Bottom gate-top contact OFET n-Si/SiO_2/ CH_3-alkylsilane /**[1,2-*b*]-22**/Au	n-type μ_{FET} μ_e: 0.02 $cm^2 V^{-1} s^{-1}$	5.8×10^4	16.2	90
OFET20	Bottom gate-top contact OFET n-Si/SiO_2/ CF_3-alkylsilane /**[1,2-*b*]-22**/Au	n-type μ_{FET} μ_e: 3.7×10^{-4} $cm^2 V^{-1} s^{-1}$	0.9×10^3	9.2	90
OFET21	Top-contact structure n^+-Si/SiO_2/**[1,2-*b*]-23**/Au	n-type μ_{FET} (vacuum) μ_e: 2.93×10^{-5} $cm^2 V^{-1} s^{-1}$	10^5	48	91
OFET22	Top-contact structure n^+-Si/SiO_2/**[1,2-*b*]-23**/Au	n-type μ_{FET} (Air) μ_e: 6.08×10^{-6} $cm^2 V^{-1} s^{-1}$	10^3	35	91
OFET23	Top-contact/bottom gate device Thermal evaporation (70 °C) p^+-Si/SiO_2/**[1,2-*b*]-24**/Au	Bipolar n, p μ_e: 2×10^{-3} $cm^2 V^{-1} s^{-1}$ μ_h: 2×10^{-4} $cm^2 V^{-1} s^{-1}$	 10^5 —	 45 −50	87
OFET24	Top-contact/bottom gate device Thermal evaporation (110 °C) p^+-Si/SiO_2/**[1,2-*b*]-24**/Au	Bipolar n, p μ_e: 0.01 $cm^2 V^{-1} s^{-1}$ μ_h: 6×10^{-4} $cm^2 V^{-1} s^{-1}$	 10^6 10^7	 60 −40	87
OFET25	Top-contact/bottom gate device Solution-processed p^+-Si/SiO_2/**[1,2-*b*]-24**/Au	μ_h: 10^{-3} $cm^2 V^{-1} s^{-1}$	10^4	−42	87
OFET26	Top-contact/bottom gate device Thermal evaporation (70 °C) p^+-Si/SiO_2/**[1,2-*b*]-25**/Au	Ambipolar n, p μ_e: 2×10^{-3} $cm^2 V^{-1} s^{-1}$ μ_h: 2×10^{-3} $cm^2 V^{-1} s^{-1}$	10^4 —	50 −32	87
OFET27	Top-contact/bottom gate device Thermal evaporation (110 °C) p^+-Si/SiO_2/**[1,2-*b*]-25**/Au	Ambipolar n, p μ_e: 6×10^{-3} $cm^2 V^{-1} s^{-1}$ μ_h: 6×10^{-3} $cm^2 V^{-1} s^{-1}$	 10^4 —	 50 −30	87

Table 3 (*continued*)

Device	Device architecture	μ	I_{on}/I_{off}	V_T (V)	Ref.
OFET28	Top-contact/bottom gate device Solution-processed p^+-Si/SiO_2/**[1,2-*b*]-25**/Au	μ_e: 2×10^{-4} cm^2 V^{-1} s^{-1} μ_h: 2×10^{-4} cm^2 V^{-1} s^{-1}	10^4 —	60 −35	87
OFET29	Top-contact/bottom gate device Drop-casting process measured under vacuum Si/SiO_2/PS/**[1,2-*b*]-26**/Au	Bipolar n-type and p-type μ_e: 1.6×10^{-3} cm^2 V^{-1} s^{-1} μ_h: 8.2×10^{-4} cm^2 V^{-1} s^{-1}	 2.8×10^5 1.5×10^2	 53 −22	92
OFET30	Top-contact/bottom gate device in vacuum Droplet-pinned crystallization process Si/SiO_2/PS/**[1,2-*b*]-26**/Au	Bipolar n-type and p-type μ_e: 7.7×10^{-4} cm^2 V^{-1} s^{-1} μ_h: 2.5×10^{-4} cm^2 V^{-1} s^{-1}	 3.1×10^2 5.3×10^4	 46 −4	92
OFET31	Top-contact/bottom gate device in vacuum Solution-shearing process Si/SiO_2/PS/**[1,2-*b*]-26**/Au	Bipolar n-type and p-type μ_e: 0.12 cm^2 V^{-1} s^{-1} μ_h: 0.02 cm^2 V^{-1} s^{-1}	 8.5×10^5 2.1×10^2	 57 −62	92
OFET32	Top-contact/bottom gate device in air Drop-casting process Si/SiO_2/PS/**[1,2-*b*]-26**/Au	p-type μ_{FET} μ_h: 2.7×10^{-4} cm^2 V^{-1} s^{-1}	6.3×10^6	−33	92
OFET33	Top-contact/bottom gate device in air Droplet-pinned crystallization process Si/SiO_2/PS/**[1,2-*b*]-26**/Au	p-type μ_{FET} μ_h: 1.6×10^{-4} cm^2 V^{-1} s^{-1}	2.6×10^4	−38	92
OFET34	Top-contact/bottom gate device in air Solution-shearing process Si/SiO_2/PS/**[1,2-*b*]-26**/Au	p-type μ_{FET} μ_h: 2.2×10^{-3} cm^2 V^{-1} s^{-1}	4.8×10^2	2.8	92
OFET35	Top-contact/bottom gate device in vacuum Drop-casting process Si/SiO_2/PS/**[1,2-*b*]-27**/Au	Bipolar n-type and p-type μ_e: 1.5×10^{-4} cm^2 V^{-1} s^{-1} μ_h: 5.3×10^{-7} cm^2 V^{-1} s^{-1}	 6.7×10^5 5.9×10^3	 47 −54	92
OFET36	Top-contact/bottom gate device in vacuum Droplet-pinned crystallization process Si/SiO_2/PS/**[1,2-*b*]-27**/Au	Bipolar n-type and p-type μ_e: 0.013 cm^2 V^{-1} s^{-1} μ_h: 2.7×10^{-4} cm^2 V^{-1} s^{-1}	 1.2×10^4 4.2×10^4	 26 −35	92
OFET37	Top-contact/bottom gate device in vacuum Solution-shearing process Si/SiO_2/PS/**[1,2-*b*]-27**/Au	Bipolar n-type and p-type μ_e: 0.04 cm^2 V^{-1} s^{-1} μ_h: 3.3×10^{-4} cm^2 V^{-1} s^{-1}	 2.2×10^5 1.2×10^5	 10 −45	92
OFET38	Top-contact/bottom gate device in air Drop-casting process Si/SiO_2/PS/**[1,2-*b*]-27**/Au	p-type μ_{FET} μ_h: 2.9×10^{-4} cm^2 V^{-1} s^{-1}	2×10^5	−12	92
OFET39	Top-contact/bottom gate device in air Droplet-pinned crystallization process Si/SiO_2/PS/**[1,2-*b*]-27**/Au	p-type μ_{FET} μ_h: 8.0×10^{-4} cm^2 V^{-1} s^{-1}	8.1×10^2	−14	92
OFET40	Top-contact/bottom gate device in air Drop-casting process Si/SiO_2/PS/**[1,2-*b*]-27**/Au	p-type μ_{FET} μ_h: 5.4×10^{-4} cm^2 V^{-1} s^{-1}	5.2×10^4	−9.7	92
OFET41	Top-contact/bottom gate device Solution-processed p^+-Si/SiO_2/**[1,2-*b*]-28**/Au	μ_h: 10^{-4} cm^2 V^{-1} s^{-1}	10^4	−30	87
OFET42	Top-contact/bottom gate device Solution-processed measured under vacuum p^+-Si/SiO_2/**[1,2-*b*]-29**/Au	Ambipolar n-type and p-type μ_e: 0.02 cm^2 V^{-1} s^{-1} μ_h: 0.01 cm^2 V^{-1} s^{-1}	1.4×10^5 2.2×10^6	34 −55	93
OFET43	Top-contact/bottom gate device in glove box at RT p-Si/SiO_2/OTMS/**[1,2-*b*]-30**/Au	Ambipolar n-type and p-type μ_e: 0.05 cm^2 V^{-1} s^{-1} μ_h: 0.14 cm^2 V^{-1} s^{-1}	 10^4 10^6	 62 −36	88
OFET44	Top-contact/bottom gate device in glove box at 60 °C p-Si/SiO_2/OTMS/**[1,2-*b*]-30**/Au	Ambipolar n-type and p-type μ_e: 0.65 cm^2 V^{-1} s^{-1} μ_h: 0.71 cm^2 V^{-1} s^{-1}	 10^4 10^5	 41 −48	88
OFET45	Top-contact/bottom gate device in glove box at 100 °C p-Si/SiO_2/OTMS/**[1,2-*b*]-30**/Au	Ambipolar n-type and p-type μ_e: 0.14 cm^2 V^{-1} s^{-1} μ_h: 0.24 cm^2 V^{-1} s^{-1}	 10^5 10^4	 60 −32	88
OFET46	Top-contact/bottom gate device in glove box at RT p-Si/SiO_2/OTMS/**[1,2-*b*]-31**/Au	p-type μ_{FET} μ_h: 0.19 cm^2 V^{-1} s^{-1}	10^6	−19	88
OFET47	Top-contact/bottom gate device in glove box at 60 °C p-Si/SiO_2/OTMS/**[1,2-*b*]-31**/Au	p-type μ_{FET} μ_h: 1.03 cm^2 V^{-1} s^{-1}	10^5	−27	88
OFET48	Top-contact/bottom gate device in glove box at 100 °C p-Si/SiO_2/OTMS/**[1,2-*b*]-31**/Au	p-type μ_{FET} μ_h: 0.22 cm^2 V^{-1} s^{-1}	10^6	−14	88
OFET49	Space-charge-limited current (SCLC) ITO/PEDOT:PSS/**[1,2-*b*]-32**/MoO_3 (10 nm)/Al (100 nm)	μ_h: 1.41×10^{-4} cm^2 V^{-1} s^{-1}			97
OFET50	Space-charge-limited current (SCLC) ITO/PEDOT:PSS/**[1,2-*b*]-33**/MoO_3 (10 nm)/Al (100 nm)	μ_h: 8.40×10^{-5} cm^2 V^{-1} s^{-1}			97
OFET51	Space-charge-limited current (SCLC) ITO/PEDOT:PSS/**[1,2-*b*]-34**/MoO_3 (10 nm)/Al (100 nm)	μ_h: 1.96×10^{-5} cm^2 V^{-1} s^{-1}			97
OFET52	Top-contact/bottom gate device p^+-Si/SiO_2/**[1,2-*b*]-35**/Au	No-gate effect	—	—	87
OFET53	Top-contact/bottom gate device Thermal evaporation (70 °C) p^+-Si/SiO_2/**[1,2-*b*]-36**/Au	n-type air stable μ_e: 4×10^{-4} cm^2 V^{-1} s^{-1}	10^4	10	87

Table 3 (*continued*)

Device	Device architecture	μ	I_{on}/I_{off}	V_T (V)	Ref.
OFET54	Top-contact/bottom gate device Thermal evaporation (110 °C) p^+-Si/SiO_2/**[1,2-*b*]-36**/Au	n-type air stable μ_e: 10^{-3} cm^2 V^{-1} s^{-1}	10^5	3	87
OFET55	Top-contact/bottom gate device Solution-processed p^+-Si/SiO_2/**[1,2-*b*]-36**/Au	n-type air stable μ_e: 10^{-4} cm^2 V^{-1} s^{-1}	10^4	7	87
OFET56	Top-contact/bottom gate device Thermal evaporation (70 °C) p^+-Si/SiO_2/**[1,2-*b*]-37**/Au	n-type air stable μ_e: 0.03 cm^2 V^{-1} s^{-1}	10^6	2	87
OFET57	Top-contact/bottom gate device Thermal evaporation (110 °C) p^+-Si/SiO_2/**[1,2-*b*]-37**/Au	n-type air stable μ_e: 0.16 cm^2 V^{-1} s^{-1}	10^7	5	87
OFET58	Top-contact/bottom gate device Solution-processed p^+-Si/SiO_2/**[1,2-*b*]-37**/Au	n-type air stable μ_e: 0.16 cm^2 V^{-1} s^{-1}	10^8	5	87
OFET59	Top-contact/bottom gate device Solution-processed p^+-Si/SiO_2/**[1,2-*b*]-38**Au	Bipolar n-type and p-type air stable μ_e: 10^{-3} cm^2 V^{-1} s^{-1} μ_h: 10^{-4} cm^2 V^{-1} s^{-1}	10^5 —	20 −25	87
OFET60	Top-contact/bottom gate device Solution-processed measured in air p^+-Si/SiO_2/**[1,2-*b*]-39**/Au	Bipolar n-type and p-type air stable μ_e: 0.13 cm^2 V^{-1} s^{-1} μ_h: 0.01 cm^2 V^{-1} s^{-1}	10^4 1.1×10^3	13 −33	93
OFET61	Bottom-Gate/bottom-contact device in glove box under ambient nitrogen Al/SU-8/Au/**[1,2-*b*]-40**	μ_{FET} Linear: 0.005 cm^2 V^{-1} s^{-1}, SS: 1.3 V dec^{-1} μ_{FET} saturation: 0.02 cm^2 V^{-1} s^{-1}, SS: 1.9 V dec^{-1}	4×10^6 5×10^5	26 20	99
OFET62	Top-contact/bottom gate device Solution processable **[1,2-*b*]-41**/PS/ SiO_2/n^{++}-Si	n-type μ_{FET} μ_e: 0.02 cm^2 V^{-1} s^{-1}	10^7–10^8	2	94
OFET63	Top-contact/bottom gate device-Thermal evaporation OTS-Si/SiO_2/**[1,2-*b*]-42**/Au	p-OFET (single crystal) μ_h: 1.44 cm^2 V^{-1} s^{-1}	10^3	—	104

Bis(triméthylsilyl)amine (HMDS); *n*-Octadecyltrimethoxysilane (OTMS); polystyrene (PS); photosensible resin (SU-8); octadecyltrichlorosilane (OTS).

[1,2-*b*]-19 and bromide in **[1,2-*b*]-20**[86] were synthesized using the adapted method of Wang *et al.*[37] The idea was to incorporate electron-withdrawing fragments to depress the LUMO energy levels of the corresponding organic semiconductors. OFET devices (OFET6-OFET12) based on these organic semiconductors were fabricated on SiO_2/Si substrates by thermal evaporation (the SiO_2 gate dielectric was treated with HMDS) with a bottom-contact geometry. As reported above, OFET3 based on **[1,2-*b*]IF(=O)$_2$** indicated no-gate effect however those based on **[1,2-*b*]-18** to **[1,2-*b*]-20** successfully showed n-type OFET behaviour increasing from **[1,2-*b*]-20** (OFET12: 9.9 × 10^{-3} cm^2 V^{-1} s^{-1}, I_{on}/I_{off}: 4 10^6, +61 V), to **[1,2-*b*]-19** (OFET11: 1.8 × 10^{-2} cm^2 V^{-1} s^{-1}, I_{on}/I_{off}: 10^7, +56 V) and to **[1,2-*b*]-18** (OFET6: 0.17 cm^2 V^{-1} s^{-1}, I_{on}/I_{off}: 2 10^7, +69 V). This work showed that the two terminal halogen groups induced n-type FET behaviour and that the mobility was dependent on the halogen size. The high mobility obtained with OFET6, 0.17 cm^2 V^{-1} s^{-1}, revealed the potential of **[1,2-*b*]-18** as an n-type material.

The top-contact device using **[1,2-*b*]-18**, OFET7, was also constructed and showed lower FET mobility (OFET7, μ_e: 6.6 × 10^{-2} cm^2 V^{-1} s^{-1}) than the bottom-contact one (OFET6, μ_e: 0.17 cm^2 V^{-1} s^{-1})). The treatment of SiO_2 by HMDS or by polystyrene (PS) was also highlighted for the bottom-contact device using **[1,2-*b*]-18**. Without HMDS or PS (OFET8[86]), the n-type μ_e was measured at 1.9 × 10^{-4} cm^2 V^{-1} s^{-1} and was significantly increased to 0.07 or 0.17 cm^2 V^{-1} s^{-1} with PS[89] (OFET9) or HMDS[86] (OFET6) treatment.

In 2011, a novel series of diones substituted on their external phenyls by two (in **[1,2-*b*]-21**) or three (in **[1,2-*b*]-22**) fluorine atoms was synthesized and used in n-type OFETs (OFET13-OFET20).[89] Their properties and efficiencies in OFET were compared to that of **[1,2-*b*]-18**, presented above.[86] The LUMO energy levels obtained by electrochemical studies were lowered from −3.38 eV for **[1,2-*b*]-18** to −3.53 eV for **[1,2-*b*]-22** showing a decrease in the LUMO in relation to the increase of the number of fluorine atoms on the [1,2-*b*]DHIF core. Depressing the LUMO energy level is, in this field, an important feature notably to reach air stable OFETs. **[1,2-*b*]-21** and **[1,2-*b*]-22** present similar UV-vis absorption spectra slightly red-shifted compared to **[1,2-*b*]-18**.

Top-contact OFETs based on **[1,2-*b*]-21** and **[1,2-*b*]-22** were fabricated on heavily doped n-type Si substrates (devices OFET13-OFET16) and compared to those based on **[1,2-*b*]-18** (OFET9-OFET10). All devices were found to be very efficient as n-type transistors with I_{on}/I_{off} exceeding 10^5 and μ_e measured between 0.05 and 0.16 cm^2 V^{-1} s^{-1} depending on the organic semiconductor and on the nature of the source drain contacts (LiF/Al or Au). These results showed that [1,2-*b*]indenofluorenones with a different number of fluorine atoms (**[1,2-*b*]-18**,

[1,2-*b*]-21 and **[1,2-*b*]-22**) are excellent transporters in n-type OFETs. The mobility was increasing consistently with the number of fluorine atoms: 2 in **[1,2-*b*]-18**, 4 in **[1,2-*b*]-21** and 6 in **[1,2-*b*]-22**, following the decrease in LUMO energy levels (−3.38/−3.43/−3.52 eV for **[1,2-*b*]-18**/**[1,2-*b*]-21**/**[1,2-*b*]-22**) showing the efficiency of the strategy.

In 2012, the electrical performance and stability of n-type OFETs based on **[1,2-*b*]-22** were more deeply investigated.[90] Different organic interlayers such as self-assembled monolayers (NH_2 in OFET17, CH_3 in OFET19 or CF_3 in OFET20) and polymeric layers (PS in OFET18) were introduced at the **[1,2-*b*]-22**-SiO_2 interfaces to control the interfacial properties. Bottom gate-top contact OFET18 showed an excellent device performance with μ_e of 0.18 $cm^2\ V^{-1}\ s^{-1}$ and I_{on}/I_{off} of 4.4×10^5. Moreover, OFET18 yielded excellent electrical stability allowing us to fabricate a complementary inverter fabricated using both p-type pentacene and n-type **[1,2-*b*]-22**.[90]

In 2007, a highly halogenated derivative, **[1,2-*b*]-23**[91] bearing eight fluorine atoms on the external phenyl and two iodine atoms on the central phenyl of the [1,2-*b*]indenofluorenone core was synthesized. Two top-contact OFET using **[1,2-*b*]-23** on a Si/SiO_2 substrate were prepared by vacuum deposition and tested either under vacuum (OFET21) or under air (OFET22). The device performances were low, with $\mu < 3 \times 10^{-5}\ cm^2\ V^{-1}\ s^{-1}$ and high threshold potentials. Compared to the performances reported above with **[1,2-*b*]-18** (OFET7 and OFET10), with **[1,2-*b*]-21** (OFET14) or **[1,2-*b*]-22** (OFET16–20), the low efficiency of OFET21 may be due to the poor film morphology and to the nature of the semiconductor/SiO_2 interface.

Elongation of the [1,2-*b*]indenofluorenone core has also been an investigated strategy to achieve efficient OFET devices (see **[1,2-*b*]-24** to **[1,2-*b*]-31** in Scheme 11).[87,88,92–94] **[1,2-*b*]-24** and **[1,2-*b*]-25** were substituted at C2 and C8 positions by two thienyl units whereas **[1,2-*b*]-28** possessed two dithienyl units at these positions. Moreover, in order to increase the processability of these organic semiconductors, solubilising groups were added to the external thienyl units in **[1,2-*b*]-26**, **[1,2-*b*]-27** and **[1,2-*b*]-29**. Different devices, OFET23-OFET42, were constructed with **[1,2-*b*]-24** - **[1,2-*b*]-29**.[87,88,92,93] With similar top-contact/bottom-gate architecture but varying their modes of fabrication (thermal evaporation at 70 or 110 °C, drop-casting or droplet pinned crystallization in vacuum or in air) a lot of different performances were reported. The devices based on **[1,2-*b*]-25** (OFET26-OFET28) have shown interesting ambipolar properties with μ_h equal to μ_e values ($\mu_e = \mu_h = 2 \times 10^{-3}/6 \times 10^{-3}/2 \times 10^{-4}\ cm^2\ V^{-1}\ s^{-1}$ for OFET26/27/28). Other devices have also shown bipolar properties (OFET29-OFET31, OFET35–37, OFET42) and the highest mobilities were obtained for **[1,2-*b*]-26** (μ_e: 0.12 $cm^2\ V^{-1}\ s^{-1}$ and μ_h: 0.02 $cm^2\ V^{-1}\ s^{-1}$) in the solution processed OFET31. **[1,2-*b*]-24** and **[1,2-*b*]-27** showed n-type and p-type OFET behaviour with however μ_e largely higher than μ_h (OFET23-OFET24 and OFET35-OFET37). From all the devices, those measured in air (OFET32–34 with **[1,2-*b*]-26** and OFET38–40 with **[1,2-*b*]-27**) present only a p-type character indicating the instability of the electron-transport in this organic semiconductor due to their too high LUMO value (−3.65 eV for **[1,2-*b*]-26** and −3.63 eV for **[1,2-*b*]-27**) (ambient-stable electron-transport is possible only with organic semiconductor possessing a LUMO lower than −4.1 eV[87,95]).

The use of alkylthio side chains in **[1,2-*b*]-30** or of dibutylamino side chains in **[1,2-*b*]-31** has been tested in order to modulate both the processability and the electronic properties.[88] **[1,2-*b*]-30** and **[1,2-*b*]-31** were obtained from their respective diketones.[88] Compared with **[1,2-*b*]-17**, substituted by *n*-butyl units (HOMO/LUMO: −6.0/−3.5 eV), it was observed that the sulfur linkage, in **[1,2-*b*]-30**, lowers the LUMO to −3.7 eV and raises the HOMO to −5.6 eV (the SBu groups are weakly electron-donating meanwhile the sulfur atom has some π-acceptor capability due to the formation of the $p_\pi(C)$-$d_\pi(S)$ orbital overlap[96]). For **[1,2-*b*]-31**, the introduction of the dibutylamino groups results in an increase of the HOMO energy level at −5.0 eV due the strong electron-donating effect of the nitrogen atoms and to a small rise of the LUMO at −3.4 eV. X-Ray analysis has shown that (a) **[1,2-*b*]-17** exhibited one-dimensional column stacking, (b) **[1,2-*b*]-30** exhibited two-dimensional brick wall stacking and (c) **[1,2-*b*]-31** adopted a two-dimensional crossed stacking. Short π–π distances of 3.45, 3.22 and 3.39 Å between the [1,2-*b*]-indenofluorenone planes were measured in **[1,2-*b*]-17**, **[1,2-*b*]-30** and **[1,2-*b*]-31**, respectively. This variation in the π–π distances demonstrates that the different side chains induce different molecular packing in the crystals, which in turn modifies the charge transfer.

To assess the charge transport properties of the films for the three semiconductors, the bottom-gate/top-contact OFET devices were produced and studied at different temperatures (RT, 60 °C or 100 °C). Devices based on **[1,2-*b*]-30** (OFET43–45) have shown the bipolar character of this organic semiconductor (μ_e/μ_h = 0.05/0.14, 0.65/0.71 and 0.14/0.24 $cm^2\ V^{-1}\ s^{-1}$ for OFET43/44/45) whereas the ones based on **[1,2-*b*]-31** (OFET46–48) have shown only p-type OFET characteristics (μ_h = 0.18, 1.03 and 0.22 $cm^2\ V^{-1}\ s^{-1}$ for OFET46, OFET47 and OFET48). All the mobilities obtained were very high. It must be recalled that OFET5 based on **[1,2-*b*]-17** presents no gate effect due to the large injection barrier and the 1D molecular packing. Oppositely, **[1,2-*b*]-30** has a more appropriate HOMO level due to the alkylthio side chain and also 2D molecular stacking, which provides favourable charge transport channels for hole and electrons. Finally, with **[1,2-*b*]-31** the 2D molecular stacking was also favourable for the charge transport however, the LUMO of **[1,2-*b*]-31** (−3.4 eV) was similar to that of **[1,2-*b*]-17** (−3.5 eV) and electron injection was rather difficult only leading to a p-type transport.

In conclusion, for **[1,2-*b*]-17** with a large injection barrier (HOMO/LUMO: −6.0/−3.5 eV) and a one-dimensional packing, no gate effect was observed (see OFET5). **[1,2-*b*]-30** with appropriate energy levels (HOMO/LUMO: −5.6/−3.7 eV) due to the sulphur linkage and a two-dimensional packing, exhibited high and balanced ambipolar transport behaviour. Finally, the nitrogen linkages in **[1,2-*b*]-31** significantly raised the HOMO level (−5.0 eV) but the LUMO level (−3.4 eV) appeared too high for electron injection. OFET46–48 exhibited high μ_h but no electron transport properties.

In 2019, **[1,2-*b*]-32**-**[1,2-*b*]-34** were synthesized (Scheme 12).[97] They were all prepared from the 6,6,12,12-tetrahexyl-6,12-dihydroindeno[1,2-*b*]fluorene **40**, which was di-brominated at C2 and C8 with benzyltrimethylammonium tribromide ($BTMABr_3$) or tetrabrominated at C2, C3, C8 and C9 with Br_2 leading to the intermediates **41** and **42**. The last step was a classical Buchwald–Hartwig C–N coupling reaction between **41** and/or **42** and the corresponding amines (**43** or **44**) to reach **[1,2-*b*]-32**–**[1,2-*b*]-34** (see Scheme 12). These three organic semiconductors were used as the Hole Transport Material (HTM) in Perovskite Solar Cells (PSC) and the performance of these devices will be discussed below in section 2.4. As will be shown, devices with **[1,2-*b*]-32** as the HTM are more efficient than those based on **[1,2-*b*]-33** and **[1,2-*b*]-34**. In order to understand the different performances, μ_h of the three organic semiconductors have been investigated by using space-charge-limited current (SCLC) techniques (OFET49-OFET51). Although the three organic semiconductors are constructed on the same central core (tetrahexyl-[1,2-*b*]DHIF), they exhibit different μ_h of 1.41×10^{-4}, 8.4×10^{-5} and 1.96×10^{-5} $cm^2\ V^{-1}\ s^{-1}$ for **[1,2-*b*]-32**, **[1,2-*b*]-33** and **[1,2-*b*]-34** respectively. The enhanced μ_h for **[1,2-*b*]-32** was attributed by the authors to the introduction of the spirofluorene-xanthenyl unit with a 3D electronic structure, which can improve intermolecular interactions to some extent and increase the transporting channels in spite of causing partial twisting of the whole molecule. For **[1,2-*b*]-34**, the introduction of four diphenylamine groups on the [1,2-*b*]DHIF core can reduce the planarity and disturb intermolecular packing, thus leading to a decrease in intermolecular charge carrier hopping, which in turn decreases the μ_h value as well (8.4×10^{-5} and 1.96×10^{-5} $cm^2\ V^{-1}\ s^{-1}$ for **[1,2-*b*]-33** and **[1,2-*b*]-34** respectively).

In order to depress the LUMO energy levels and to increase the stability in air of their related n-type OFETs, organic semiconductors based on the electron-deficient [1,2-*b*]-indenofluorenebis(dicyanovinylene) ([1,2-*b*]DHIF(=C(CN)$_2$)$_2$) have then been investigated (see **[1,2-*b*]-35** to **[1,2-*b*]-41** in Scheme 11). These molecules were obtained by Knoevenagel condensation of their related diones with malononitrile.[87,98] Our group also designed in 2018 another organic semiconductor, **[1,2-*b*]-40**,[99] also based on the electron-deficient [1,2-*b*]DHIF(=C(CN)$_2$)$_2$) core with two alkyl units (n-C_5H_{11}) substituting the external phenyl rings (instead of two n-$C_{12}H_{25}$ groups in the central phenyl ring in **[1,2-*b*]-35**).[99] Highly soluble **[1,2-*b*]-41**, also based on the electron-deficient [1,2-*b*]DHIF(=C(CN)$_2$)$_2$) core bearing two triisopropylsilyl-ethynyl endgroups was prepared by the Kim and Usta group.[94]

The main electronic properties modification of **[1,2-*b*]-35** to **[1,2-*b*]-39** compare to their related diones (**[1,2-*b*]-16**, **[1,2-*b*]-24-25** and **[1,2-*b*]-28-29**) concerns their LUMO energy levels that decreased by ~0.63 eV (when their HOMO levels increase by ~0.15 eV). Due to these HOMO/LUMO variations, the gap of **[1,2-*b*]-35** to **[1,2-*b*]-39** was reduced from 0.25 to 0.38 eV compared to that of their related diones. Compared to **[1,2-*b*]-35**, in which the LUMO was measured at −4.30 eV,[87] our group measured the LUMO of **[1,2-*b*]-40** at the very low energy

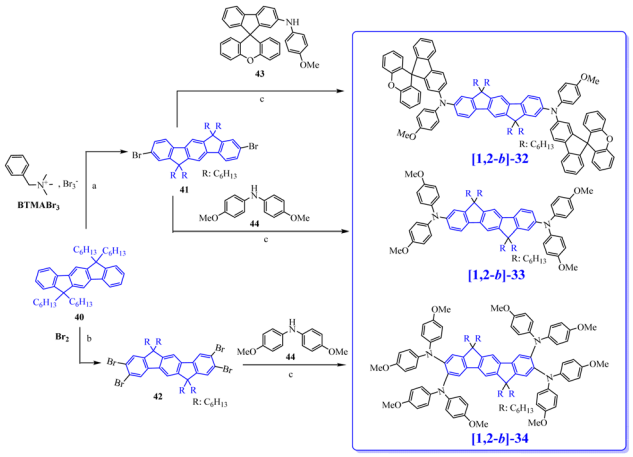

Scheme 12 Synthesis of **[1,2-*b*]-32**, **[1,2-*b*]-33** and **[1,2-*b*]-34**. (a) $ZnCl_2$, AcOH, 70 °C; (b) $CHCl_3$, $FeCl_3$, 0 °C; (c) P(^{t}Bu)$_3$, Pd(OAc)$_2$, sodium *tert*-butoxide, toluene, 110 °C.

of −4.1 eV.[99] The dicyanovinylene fragment appeared then as a very efficient electron-withdrawing group to strongly depress the LUMO energy level. The dicyanovinylene is currently a widely used fragment in efficient n-type OFET.[78,99–103]

Top contact FETs (OFET52–60) were fabricated by either vacuum deposition or spin-coating on octadecyltrichlorosilane (OTS)-treated SiO_2/p$^+$-Si substrates. No-gate effect was observed for OFET52 based on **[1,2-*b*]-35**.

The top-contact devices based on **[1,2-*b*]-36** (OFET53–55) and **[1,2-*b*]-37** (OFET56–58) have shown n-type air stable activity with μ_e around $10^{-4}/10^{-3}$ $cm^2\ V^{-1}\ s^{-1}$ for **[1,2-*b*]-36** and μ_e around 0.03/0.16 $cm^2\ V^{-1}\ s^{-1}$ for **[1,2-*b*]-37**. Finally, **[1,2-*b*]-38** in OFET59 and **[1,2-*b*]-39** in OFET60 have also shown bipolar properties with μ_e (10^{-3} $cm^2\ V^{-1}\ s^{-1}$) equal to 10 × μ_h for **[1,2-*b*]-38** and μ_e (0.13 $cm^2\ V^{-1}\ s^{-1}$) equal to 13 × μ_h for **[1,2-*b*]-39**.

A comparison of these performances with those of the related dione-based devices indicates that for **[1,2-*b*]-36**, OFET53–55, despite the OFETs being air-stable, the μ_e was lower than that for **[1,2-*b*]-24** in OFET23–25 (see Table 3).

Oppositely, the comparison of devices based on **[1,2-*b*]-37** (OFET56-OFET58) to those based on **[1,2-*b*]-25** (OFET26-OFET28), shows n-type air-stable devices with the former and a μ_e increasing from 2×10^{-3} $cm^2\ V^{-1}\ s^{-1}$ in OFET26 to 0.03 $cm^2\ V^{-1}\ s^{-1}$ in OFET56, from 6×10^{-3} $cm^2\ V^{-1}\ s^{-1}$ in OFET27 to 0.16 $cm^2\ V^{-1}\ s^{-1}$ in OFET57 and from 2×10^{-4} $cm^2\ V^{-1}\ s^{-1}$ in OFET28 to 0.16 $cm^2\ V^{-1}\ s^{-1}$ in OFET58, indicating the positive effect of the presence of the dicyanovinylene units in **[1,2-*b*]-37**.

It must also be noted that OFET56–58 exhibits very low threshold voltages (around 2 to 5 V) in accordance, among other parameters (morphological or device mode preparation), to its very low LUMO of 4.32 eV.[87]

The comparison between OFET59 and OFET41, highlights the similarity of μ_h in both devices (10^{-4} $cm^2\ V^{-1}\ s^{-1}$). However, due to the presence of the dicyanovinylene units of **[1,2-*b*]-38**, a μ_e value of 10^{-3} $cm^2\ V^{-1}\ s^{-1}$ was measured in the air stable

OFET59. Finally, a similar comparison between OFET60 and OFET42, also points to the same μ_h value in both devices (10^{-2} cm^2 V^{-1} s^{-1}). However, the presence of the dicyanovinylene units in **[1,2-*b*]-40**, increases the μ_e value to 0.13 cm^2 V^{-1} s^{-1} which was also measured in the air stable OFET60.

Bottom-gate bottom-contact n-type channel OFETs were also constructed with **[1,2-*b*]-40** as the active layer.[99] Contrary to OFET 3 based on **[1,2-*b*]IF(=O)$_2$**, which demonstrated no-gate effect, an electron mobility of 0.02 cm^2 V^{-1} s^{-1} was measured in OFET61. The performance of OFET61 remains lower than those of OFET6 (μ_e: 0.17 cm^2 V^{-1} s^{-1}) based on the difluoro **[1,2-*b*]-18**, and higher than that of OFET11 and OFET12 based on the dichloro **[1,2-*b*]-19** or dibromo **[1,2-*b*]-20**. This shows how rational design is complicated to establish to reach high performances.

The solution processable OFET62 based on **[1,2-*b*]-41** has shown μ_e as high as 0.02 cm^2 V^{-1} s^{-1} with a very high I_{on}/I_{off} ratio of 10^7–10^8 and a low threshold voltage of around 2 V under ambient atmosphere.[94] These results demonstrate that (triisopropylsilyl)ethynyl substitution is a possible approach to realize new families of solution-processable organic semiconductors.

Finally, OFET63 is a p-type OFET based on the indenofluorene-extended tetrathiafulvalene, **[1,2-*b*]-42** (HOMO/LUMO: −4.64/−2.09 eV).[105] OFET63 was constructed using a single crystal of **[1,2-*b*]-42** and carrier mobility was demonstrated to vary with the α- or β-phase of the crystal. With the α-phase **[1,2-*b*]-42** single crystal, the hole mobility, μ_h, reached the very high value of 1.44 cm^2 V^{-1} s^{-1} with an I_{on}/I_{off} ratio of 10^3.[104]

2.4. [1,2-*b*]DHIF-based organic semiconductors used as the host for phosphorescent OLEDs

At the end of the twentieth century, the development of phosphorescent organic light-emitting devices (PhOLEDs) attracted a great deal of attention since Baldo, O'Brien, and Forrest[106] announced the possibility of harvesting all the singlet and triplet excitons generated in an appropriate organic semiconductor matrix *via* a heavy metal-containing complex dispersed as the dopant in this organic semiconductor. The design of organic host materials possessing specific properties and notably a triplet energy value higher than that of the phosphorescent emitters then started to be significantly developed and has been the driving force of the field.

Different design tactics were studied to gather within a host material all the necessary properties to fit with a phosphorescent emitter in a PhOLED. The ideal host should possess:

(i) a triplet energy (E_{T1}) above that of the phosphor used (*ca.* 2.2 eV for red, 2.5 eV for green, and 2.7 eV for blue phosphors) to confine the triplet excitons within the phosphorescent guest,

(ii) HOMO/ LUMO energy level fitting with those of the phosphor and with the Fermi levels of the electrodes (or of the adjacent transporting layers) to ensure efficient charge injection,

(iii) good and equilibrated μ_h and μ_e values for efficient charge transport and recombination,

(iv) thermal and morphological stabilities to reach a stable electroluminescence and extend the lifetime of the device.

The [1,2-*b*]DHIF core has been used to construct a high E_{T1} host material for PhOLEDs. Due to the presence of three phenyl rings, reaching high E_{T1} values was nevertheless a difficult task (see below). Indeed, high E_{T1} materials are usually obtained with small π-conjugated units with restricted conjugation.[73,107–116]

The first organic semiconductor constructed on the [1,2-*b*]DHIF core used as the host for a phosphorescent emitter was **[1,2-*b*]-43**[117] (Fig. 6). The [1,2-*b*]DHIF core was built from a SBF fragment **45** in which was bridged an additional phenyl ring *via* an intramolecular electrophilic substitution (Scheme 13).

Due to the substituents attached on the two bridges, the T_d of **[1,2-*b*]-43** was higher (354 °C) than that of **[1,2-*b*]DHIF** (200 °C). **[1,2-*b*]-43** presented a T_g of 171 °C suggesting good morphological stability as an active material in a device. The HOMO of **[1,2-*b*]-43** was measured at −5.83 eV, similar to that of **[1,2-*b*]DHIF** (−5.81 eV) showing that the first oxidation occurs on the [1,2-*b*]DHIF core for both compounds. The optical gap was measured at 3.49 eV (in $CHCl_3$) for **[1,2-*b*]-43** slightly more contracted than for **[1,2-*b*]DHIF** (3.61 eV in CH_2Cl_2).

E_{T1} of **[1,2-*b*]-43** (2.52 eV) was estimated from the first phosphorescent peak (492 nm) measured at 77 K in ethanol. This value was close to that of the parent *para*-terphenyl (E_{T1}: 2.55 eV)[24] and higher than that of the green emitter Ir(ppy)$_2$(acac) (E_{T1}: 2.41 eV).[118] In **[1,2-*b*]-43**, the E_{T1} is driven by the [1,2-*b*]DHIF core but remains relatively high for an extended π-conjugated fragment. Thus, these works have revealed that the bridges (as in **[1,2-*b*]-43** and **[1,2-*b*]DHIF**) and the planification induced, do not significantly modify the E_{T1} of these compounds compared to the *para*-terphenyl parent.[24,27] This was an important finding, which has driven the molecular engineering works of the triplet state of this fragment.[24,27,119] Interestingly, μ_h of **[1,2-*b*]-43** has been measured at a relatively high value for a spiro compound, from 3.9×10^{-3} to 5.6×10^{-3} cm^2 V^{-1} s^{-1}. This value of μ_h was higher than that measured for **[1,2-*b*]-4** (10^{-3} cm^2 V^{-1} s^{-1}) and that measured for **[1,2-*b*]-5** (around 10^{-4} cm^2 V^{-1} s^{-1}).

[1,2-*b*]-43 was used as the host for the green phosphor Ir(ppy)$_2$(acac) in multi-layer PhosOLED1. With a V_{on} of 2.5 V, an EQE_{max} of 15.8% (CE: 60 cd A^{-1}, PE: 63 lm W^{-1}) and an EL spectrum in accordance with that of the green dopant without

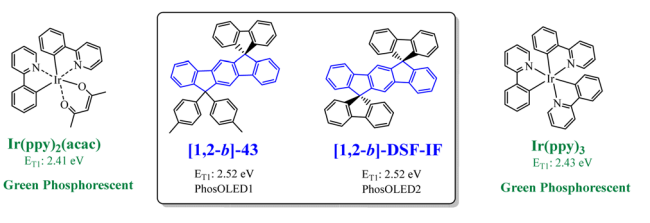

Fig. 6 [1,2-*b*]DHIF-based organic semiconductors used as the host for phosphorescent dopants in PhOLEDs (**[1,2-*b*]-43** and **[1,2-*b*]-DSF-IF**) and green phosphorescent Ir(ppy)$_2$(acac) and Ir(ppy)$_3$.

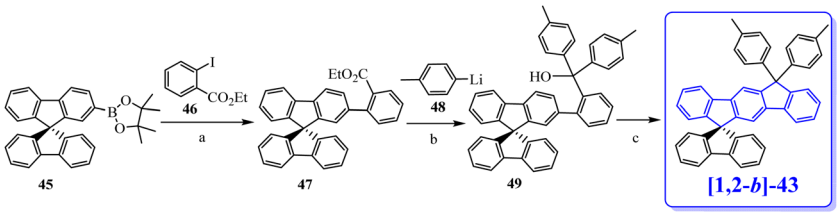

Scheme 13 Synthesis of **[1,2-*b*]-43**. (a) $Pd(PPh_3)_4$, P^tBu_3, K_3PO_4, toluene, reflux, (b)THF, −78 °C, and (c) $HOAc/H_2SO_4$.

emission of **[1,2-*b*]-43**, this first phosphorescent device based on the [1,2-*b*]DHIF fragment was promising.

In 2015, following a similar strategy, our group showed the efficiency of **[1,2-*b*]-DSF-IF** as the host for green PhOLED.[24] As the E_{T1} of **[1,2-*b*]-DSF-IF** (2.52 eV[24]) was similar to that of **[1,2-*b*]-43** (2.52 eV[117]), it was concluded that E_{T1} was driven by the [1,2-*b*]DHIF core and therefore adapted to the $Ir(ppy)_3$ green phosphorescent (E_{T1}: 2.43 eV}). PhosOLED2 emitted light since 3.5 V and reached EQE_{max}: 9.9% (CE_{max}: 31.4 cd A^{-1} and PE_{max}: 15.5 lm W^{-1}). After this work, modification of the terphenyl linkages appeared to be an efficient strategy to increase the E_{T1} (Part 4).

2.5. [1,2-*b*]DHIF-based organic semiconductors used in other electronic devices

The [1,2-*b*]DHIF core has also been used as the building unit in organic semiconductors for other electronic devices showing the versatility of this fragment. Thus, **[1,2-*b*]-32**–**[1,2-*b*]-34**[97] (Schemes 11 and 14) were used as the HTM in dopant-free perovskite solar cells (PSCs) (Table 5). All devices were prepared by spin-coating processes and the thickness of the HTM layer was optimized to tune the charge transport and device performances. Under the optimized conditions, the PSC1 with **[1,2-*b*]-32** as the HTM exhibited the best performances: a power conversion efficiency (PCE) of 17.6% with an open-circuit voltage (V_{OC}) of 1.05 V, short-circuit current density (J_{SC}) of 21.5 mA cm^{-2} and fill factor (FF) of 77.3%. The PSC2 device based on **[1,2-*b*]-33** was also efficient (PCE: 14.5%, V_{OC}: 0.96 V, J_{SC}: 20.8 mA cm^{-2}, and FF: 72.5%) contrary to the PSC3 device based on **[1,2-*b*]-34**, which exhibited lower values (PCE: 12.7%, V_{OC}: 0.92 V, J_{SC}: 20.8 mA cm^{-2} and FF: 66.6%). The higher V_{OC} obtained with **[1,2-*b*]-32** as the HTM (compared to devices using **[1,2-*b*]-33** or **[1,2-*b*]-34**) was linked to its deeper HOMO energy (HOMO: −5.22, −5.16 and −5.07 eV for **[1,2-*b*]-32**, **[1,2-*b*]-33** and **[1,2-*b*]-34** respectively). Moreover, **[1,2-*b*]-33** and **[1,2-*b*]-34** present a stronger tendency toward crystallization, which causes a negative effect on the intermolecular charge transport and reduces the FF values (72.5 or 66.6% with **[1,2-*b*]-33** or **[1,2-*b*]-34** as the HTM) in comparison to **[1,2-*b*]-32** (FF: 77.3%).

Other organic semiconductors based on a central [1,2-*b*]DHIF core were used as organic dyes for dye-sensitized solar cells (DSSCs). As examples, **[1,2-*b*]-44**-**[1,2-*b*]-46** (Scheme 14), with tetraethylhexyl-[1,2-*b*]DHIF as the linker, a diphenylamine unit as the donor and three different acceptor units (cyanoacrylic acid for **[1,2-*b*]-44**, thienyl-cyanoacrylic acid for **[1,2-*b*]-45** and furyl-cyanoacrylic acid for **[1,2-*b*]-46**) were prepared from [1,2-*b*]DHIF.[120] DSSCs were fabricated using **[1,2-*b*]-44**–**[1,2-*b*]-46** and nanocrystalline anatase TiO_2. The electrolyte used was composed of 0.05 M I_2/0.5 M *tert*-butylpyridine in acetonitrile. The device performances recorded under standard

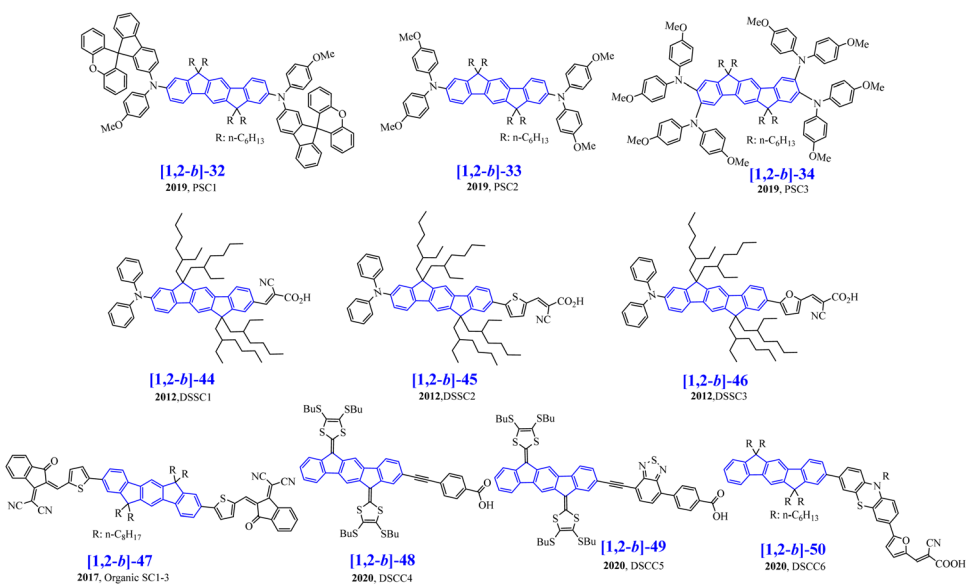

Scheme 14 **[1,2-*b*]DHIF**-based organic semiconductors used as the active material in different solar cells.

Table 4 Performance of green PhosOLED devices with [1,2-*b*]DHIF-based **[1,2-*b*]-43** or **[1,2-*b*]-DSF-IF** as the host

Device	Device architecture	V_{on} (V)	EQE (%)	CE (cd A^{-1})	PE (lm W^{-1})	CIE (x, y)	Ref.
PhosOLED1	ITO/PEDOT:PSS(30 nm)/NPB(15 nm)/TCTA(5 nm)/ **[1,2-*b*]-43**: $Ir(ppy)_2(acac)$ 10% (25 nm)/TPBI(50 nm)/LiF(0.5 nm)/Al(100 nm)	2.5	15.8	60	63	(0.32, 0.64)	117
PhosOLED2	ITO/CuPc(10 nm)/NPB(40 nm)/TCTA(10 nm)/ **[1,2-*b*]-DSF-IF**:$Ir(ppy)_3$ 10% (20 nm)/TPBI(40 nm)/LiF(1.2 nm)/Al(100 nm)	3.5	9.9	31.4	15.5	(0.33, 0.62)	24

2,2′,2″-(1,3,5-Benzinetriyl)-tris(1-phenyl-1-*H*-benzimidazole) (TPBI); Copper(II) phthalocyanine (CuPc).

global AM 1.5 solar conditions are summarized in Table 5 (devices DSSC1-DSSC3). The J_{SC}, V_{OC} and FF of the three devices were reported in the ranges of 6.95–8.20 mA cm^{-2}, 0.70–0.71 V and 69–71%, respectively corresponding to an overall conversion efficiency of 3.36–4.05%. **[1,2-*b*]-46**-based DSSC3 has the best PCE among all. Action spectra of the incident photon-to-current conversion efficiency (IPCE) as a function of wavelength were measured to evaluate the photo-response in the whole region. An IPCE performance of *ca.* 80% was observed from 400 to 550 nm for **[1,2-*b*]-45** and **[1,2-*b*]-46** with maximum values of 80% at 480 nm and 88% at 460 nm. The higher efficiency of **[1,2-*b*]-45** and **[1,2-*b*]-46** was attributed to the better light harvesting due to the extended π-conjugation and/or the higher dye density of **[1,2-*b*]-45** (4.04×10^{-7} mol cm^{-2}) and **[1,2-*b*]-46** (3.84×10^{-7} mol cm^{-2}) than **[1,2-*b*]-44** (3.34×10^{-7} mol cm^{-2}) on the TiO_2 surface.

In 2017, **[1,2-*b*]-47**[121] based on a central [1,2-*b*]-tetraoctyl-IF core decorated at C2 and C8 by two electrodeficient units (Scheme 14) was prepared from **[1,2-*b*]DHIF**. **[1,2-*b*]-47** showed intense and broad UV-vis absorption in the 470–690 nm wavelength region and suitable energy levels (HOMO: −5.42 eV and LUMO: −3.85 eV). The photovoltaic performances of **[1,2-*b*]-47** were tested with a highly efficient low gap polymer as the donor namely PTB7-Th. Organic solar cells (SC1-SC3) were fabricated by spin-coating from *o*-dichlorobenzene of PTB7-Th and **[1,2-*b*]-47** solution in an inverted configuration of ITO/ZnO/PFN/PTB7-Th:**[1,2-*b*]-47**/MoO_3/Al. Three devices with different ratios of PTB7-Th:**[1,2-*b*]-47** (SC1-SC3: 1/1, 1 : 1.5 and 1 : 2, respectively) were tested. The best performance was reached with SC2 with the ratio PTB7-Th:**[1,2-*b*]-47** of 1 : 1.5. The SCLC method was used to measure μ_e and μ_h in PTB7-Th:**[1,2-*b*]-47** (1 : 1.5) blended films showing balanced and moderate charge transport properties (μ_h: 8.24×10^{-5} cm^2 V^{-1} s^{-1} and μ_e: 3.02×10^{-5} cm^2 V^{-1} s^{-1}).

In 2020, two extended [1,2-*b*]DHIF-TTF based on **[1,2-*b*]-42** (Scheme 11) were synthesized (**[1,2-*b*]-48** and **[1,2-*b*]-49**, Scheme 14). The two donor–acceptor molecules possess **[1,2-*b*]-42** as the donor unit and either benzoic acid in **[1,2-*b*]-48** or benzothiadiazole-benzoic acid in **[1,2-*b*]-49** as the acceptor unit. The two molecules were used in dye-sensitized solar cells containing the I^-/I_3^- redox mediator (DSSC4 and DSSC5 in Table 5). The highest power conversion efficiency reached for DSSC5 sensitized by **[1,2-*b*]-49** was 6.4% with a photocurrent density of 10.1 mA cm^{-2} and photovoltage of 0.81 V. With **[1,2-*b*]-48**, the conversion efficiency was 4.8% with a photocurrent density of 7.3 mA cm^{-2} and photovoltage of 0.81 V (DSSC4). The best results obtained with **[1,2-*b*]-49** were due to better intramolecular charge separation caused by the stronger electron accepting unit on which the LUMO was mainly located.[122]

Table 5 Performances of devices using [1,2-*b*]DHIF-based materials (solar cells, dyes for DSSC, *etc.*

Device	Device architecture	J_{SC} (mA cm^{-2})	V_{OC} (V)	FF (%)	PCE (%)	Ref.
PSC1	Dopant-free perovskite solar cell FTO/C_{60}/perovskite ($CH_3NH_3PPbI_{3-x}Cl_x$)/ **[1,2-*b*]-32**/MoO_3/Ag	21.5	1.05	77.3	17.6	97
PSC2	Dopant-free perovskite solar cell FTO/C_{60}/perovskite ($CH_3NH_3PbI_{3-x}Cl_x$)/ **[1,2-*b*]-33**/MoO_3/Ag	20.8	0.96	72.5	14.5	97
PSC3	Dopant-free perovskite solar cell FTO/C_{60}/perovskite ($CH_3NH_3PPbI_{3-x}Cl_x$)/ **[1,2-*b*]-34**/MoO_3/Ag	20.8	0.92	66.6	12.7	97
DSSC1	Dye sensitized solar cell TiO_2/FTO/**[1,2-*b*]-44**/Platinized FTO	6.95	0.70	69	3.36	120
DSSC2	Dye sensitized solar cell TiO_2/FTO/**[1,2-*b*]-45** /Platinized FTO	8.10	0.70	71	4.04	120
DSSC3	Dye sensitized solar cell TiO_2/FTO/**[1,2-*b*]-46**/Platinized FTO	8.20	0.71	70	4.05	120
SC1	ITO/ZnO/PFN/PTB7-Th:**[1,2-*b*]-47**(1:1)/MoO_3/Al	11.87	0.90	45.8	4.89	121
SC2	ITO/ZnO/PFN/ PTB7-Th:**[1,2-*b*]-47**(1:1.5)/MoO_3/Al	12.71	0.92	54.2	6.33	121
SC3	ITO/ZnO/PFN/ PTB7-Th:**[1,2-*b*]-47**(1:2)/MoO_3/Al	11.85	0.90	53.5	5.74	121
DSSC4	Dye sensitized solar cell TiO_2/FTO/**[1,2-*b*]-48** + I^-/I_3^-/Platinized FTO	7.3	0.81	81	4.8–5.0	122
DSSC5	Dye sensitized solar cell TiO_2/FTO/**[1,2-*b*]-49** + I^-/I_3^-/Platinized FTO	10.1	0.81	81	6.4–7.1	122
DSSC6	Dye sensitized solar cell TiO_2/FTO/**[1,2-*b*]-50** + I^-/I_3^-/Platinized FTO	11.3	0.71	70.75	5.72	123

Fluorine-doped Tin Oxide (FTO); poly[9,9-bis(3′-(*N*,*N*-dimethyl)-propyl-2,7-fluorene)-*alt*-2,7-(9,9-dioctylfluorene)] (PFN); poly((4,8-bis[(5-(2-ethylhexyl)-2-thienyl]benzo[1,2-*b*:4,5-*b*′]dithiophene-2,6-diyl)(3-fluoro-2-[(2-ethylhexyl)carbonyl]thieno[3,4-*b*]thiophenediyl) (PTB7-Th)

More recently, **[1,2-*b*]-50** with extended [1,2-*b*]-IF moieties as the donor unit and a cyanoacrylic acid moiety as the acceptor unit was designed (Scheme 14).[123] The **[1,2-*b*]-50** absorption spectrum in solution showed two sets of bands: the first one in the 300–400 nm range (attributed to the transitions of the π–π* conjugated system) and the second in the 400–600 nm range (assigned to the intramolecular charge transfer (ICT) transition between the donor and the acceptor units). When recorded in the solid state, these two sets of absorption bands merged in a broad absorption band in the 350–700 nm range. In this work, the authors highlight the interest of **[1,2-*b*]-50** with its five hexyl units to control the aggregation and to reduce the exciton quenching. The photocurrent–voltage (*J*–*V*) characteristics of the DSSC6 based on **[1,2-*b*]-50** (Table 5) were recorded under simulated AM 1.5 G irradiation using the I^-/I_3^- redox couple as the electrolyte to evaluate the photovoltaic parameters. DSSC6 gives a J_{SC} of 11.3 mA cm^{-2}, V_{OC} of 0.71 V, FF of 70.75% and PCE of 5.72%. Compared to DSSC1-DSCC5, DSCC6 presents greater performances. The five hexyl chains present in the **[1,2-*b*]-50** skeleton play an important role in the electron injection efficiency. They act as an hydrophobic barrier to avoid the charge recombination of electrons from TiO_2 to oxide electrolyte and they reduce the intermolecular stacking.

Numerous π-conjugated organic molecules have been described as multi-photon absorbing materials due to their versatile applications in two-photon cellular imaging, optical power limiting, multiphoton pumper lasing, three-dimensional optical storage and photodynamic therapy.[124] Large two-photon absorption (TPA) cross-sections have often been related to their effective π-delocalization, which leads to an extended charge separation. Some organic semiconductors based on a central [1,2-*b*]DHIF core have been highlighted in the literature for their 2-photon or 3-photon absorption properties (see **[1,2-*b*]-51**–**[1,2-*b*]-61** in Scheme 15).

In 2008, **[1,2-*b*]-51**[125] was used for its 2-photon absorption and optical limiting properties. In **[1,2-*b*]-51**, the central **[1,2-*b*]**-tetra-butyl-IF was flanked on both sides by two dibutylamino groups with (*E*)-1-styryl-4-vinylbenzene bridges. Compared to the absorption spectrum of **[1,2-*b*]DHIF**,[40] that of **[1,2-*b*]-51** (334 *vs.* 423 nm in cyclohexane) was red-shifted by 89 nm due to the presence of the two arms at C2 and C8. Similarly, the emission was red-shifted from 356 nm for **[1,2-*b*]DHIF** to 462 nm for **[1,2-*b*]-51**[125] with a similar fluorescent quantum yield (around 0.6). Contrary to **[1,2-*b*]DHIF**, **[1,2-*b*]-51**[125] presented a positive solvatochromism in emission with increasing solvent polarity with a red shift from 462 nm in non-polar cyclohexane to 586 nm in more polar dimethylacetamide, showing charge transfer properties.

The TPA value of **[1,2-*b*]-51**,[125] in $CHCl_3$ at 775 nm, was 890 GM and the value measured by the nonlinear transmission method ($CHCl_3$) was 670 GM. TPA cross-section values at 775 nm, in five different solvents other than $CHCl_3$, were also determined (551 GM in cyclohexane, 853 GM in toluene, 685 GM in THF, 675 GM in CH_2Cl_2 and 723 GM in dimethylacetamide). The TPA-cross-section appears to be neither monotonically dependent on the polarity of the solvent nor of the optical dielectric constant of the solvents (Table 6).

In 2010, **[1,2-*b*]-52** was prepared with a series of TPA-active D–π–D fluorophores[126] with different central cores. **[1,2-*b*]-52** presents, in toluene, an absorption/emission band at 413/450 nm, both blue shifted compared to those of **[1,2-*b*]-51** (429/477 nm in toluene) and translating to a less extended conjugation in **[1,2-*b*]-52** than in **[1,2-*b*]-51**. The TPA cross-section of **[1,2-*b*]-52** was of 1280 GM (@775 nm), 1.5 more important than for **[1,2-*b*]-51** (853 GM @ 775 nm).

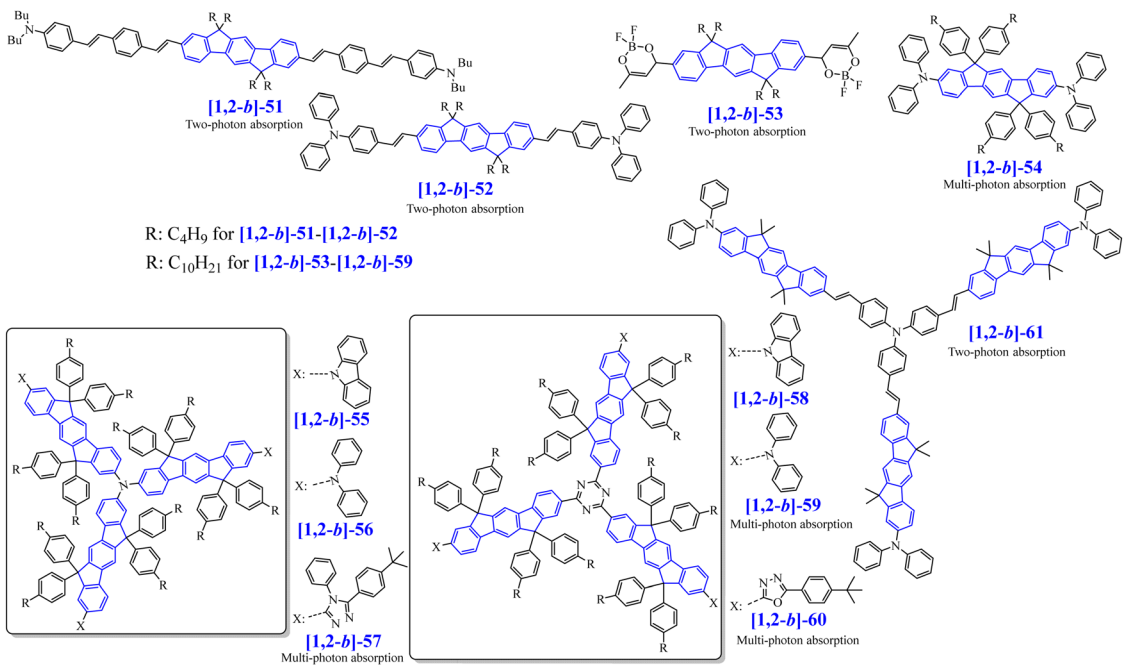

Scheme 15 **[1,2-*b*]DHIF**-based organic semiconductors presenting NLO properties.

Table 6 Linear and/or nonlinear optical properties of **[1,2-b]-51**-**[1,2-b]-61**

Compound	λ_{abs}	λ_{em}	QY	NLO properties	T_d (°C)	Ref.
[1,2-*b*]-51	λ_{abs}: 423 nm (CHX)	λ_{em}: 462 (493) nm (CHX)	QY(fluo): 0.60 (CHX)	2PA(775 nm): 551 GM (CHX)	—	125
	λ_{abs}: 429 nm (Toluene)	λ_{em}: 477 (508) nm (Toluene)	QY(fluo): 0.70 (Toluene)	2PA(775 nm): 853 GM (Toluene)		
	λ_{abs}: 428 nm ($CHCl_3$)	λ_{em}: 509 nm ($CHCl_3$)	QY(fluo): 0.64 ($CHCl_3$)	2PA(775 nm): 670 GM ($CHCl_3$)		
	λ_{abs}: 428 nm (THF)	λ_{em}: 533 nm (THF)	QY(fluo): 0.68 (THF)	2PA(775 nm): 685 GM (THF)		
	λ_{abs}: 430 nm (CH_2Cl_2)	λ_{em}: 543 nm (CH_2Cl_2)	QY(fluo): 0.69 (CH_2Cl_2)	2PA(775 nm): 675 GM (CH_2Cl_2)		
	λ_{abs}: 431 nm (DMA)	λ_{em}: 586 nm (DMA)	QY(fluo): 0.28 (DMA)	2PA(775 nm):723 GM (DMA)		
[1,2-*b*]-52	λ_{abs}: 413 nm (Toluene)	λ_{em}: 450 nm (Toluene)	QY(fluo): 0.66 (Toluene)	2PA(775 nm): 1280 GM (Toluene)	—	126
[1,2-*b*]-53	λ_{abs}: 440 nm (CH_3CN)	λ_{em}: 506 nm (CH_3CN)	QY(fluo): 0.67 (CH_3CN)	2PA(730 nm): 2800 GM (CH_3CN)	—	127
[1,2-*b*]-54	λ_{abs}: 405 nm (Toluene)	λ_{em}: 414, 443 nm (Toluene)	QY(fluo): 0.85 (Toluene)	2PA(810 nm): 59.6 GM (Toluene)	435	128 and 129
	λ_{abs}: 404 nm ($CHCl_3$)	λ_{em}: 421, 444 nm ($CHCl_3$)		3PA[a](1230 nm): 2.02 (Toluene)		
	λ_{abs}: 403 nm (DMF)	λ_{em}: 428 nm (DMF)				
[1,2-*b*]-55	λ_{abs}: 423 nm (Toluene)	λ_{em}: 443 nm (Toluene)	QY(fluo): 0.96 (Toluene)	2PA(700 nm): 1887 GM (Toluene)	438	130 and 131
	λ_{abs}: 416 nm ($CHCl_3$)	λ_{em}: 450 nm ($CHCl_3$)		3PA[a] (1270 nm): 2.2 (Toluene)		
	λ_{abs}: 419 nm (DMF)	λ_{em}: 469 nm (DMF)				
[1,2-*b*]-56	λ_{abs}: 429 nm (Toluene)	λ_{em}: 443 nm (Toluene)	QY(fluo): 0.86 (Toluene)	2PA(700 nm): 2579 GM (Toluene)	463	130 and 131
	λ_{abs}: 423 nm ($CHCl_3$)	λ_{em}: 451 nm ($CHCl_3$)		3PA[a] (1270 nm): 2.45 (Toluene)		
	λ_{abs}: 427 nm (DMF)	λ_{em}: 457 nm (DMF)				
[1,2-*b*]-57	λ_{abs}: 429 nm (Toluene)	λ_{em}: 450 nm (Toluene)	QY(fluo): 0.84 (Toluene)	2PA(700 nm): 1620 GM (Toluene)	400	129 and 130
	λ_{abs}: 431 nm ($CHCl_3$)	λ_{em}: 464 nm ($CHCl_3$)		3PA[a] (1270 nm): 3.35 (Toluene)		
	λ_{abs}: 425 nm (DMF)	λ_{em}: 493 nm (DMF)				
[1,2-*b*]-58	λ_{abs}: 400(399[129]) nm (Toluene)	λ_{em}: 426(430[129]) nm (Toluene)	QY(fluo): 0.98 (0.87[129])(Toluene)	2PA(770 nm): 5120 GM (Toluene)	448	129 and 131
	λ_{abs}: 399 nm ($CHCl_3$)	λ_{em}: 459 nm ($CHCl_3$)		3PA[a] (1200 nm): 3.3 (Toluene)		
	Non soluble in DMF	Non soluble in DMF				
[1,2-*b*]-59	λ_{abs}: 428(427[129]) nm (Toluene)	λ_{em}: 467(461[129]) nm (Toluene)	QY(fluo): 0.90 (Toluene)	2PA(820 nm): 3630 GM (Toluene)	426	129 and 131
	λ_{abs}: 426 nm ($CHCl_3$)	λ_{em}: 510 nm ($CHCl_3$)		3PA[a] (1260 nm): 1.6 (Toluene)		
	λ_{abs}: 427 nm (DMF)	λ_{em}: 591 nm (DMF)				
[1,2-*b*]-60	λ_{abs}: 381, 403 nm (Toluene)	λ_{em}: 415, 440 nm (Toluene)	QY(fluo): 0.89 (Toluene)	2PA(700 nm): 1420 GM (Toluene)	—	131
				3PA[a] (1200 nm): 2 (Toluene)		
[1,2-*b*]-61	λ_{abs}: 419 nm (THF)	λ_{em}: 479 nm (THF)	QY(fluo): 0.72 (THF)	2PA(720 nm): 5270 GM (THF)	—	132

[a] 3PA cross-section ($\times 10^{-76}$ cm^6 s^2); dimethylacetamide (DMA); Goeppert–Mayer (GM): 10^{-50} cm^4 s $photon^{-1}$.

[1,2-*b*]-53[127] belongs to the A–π–A fluorophores family as dioxaborine moieties are strong electron-acceptor units. This dye is a strong absorber with a long-wavelength maximum at 440 nm (in CH_3CN) and its blue emission was observed with a maximum at 506 nm and a quantum yield of 0.67. The large Stokes shift of 3200 cm^{-1} indicates a significant rearrangement in the excited state. The TPA spectrum of **[1,2-*b*]-53** reaches 2800 GM at 730 nm, which was in 2018 beyond the values reported for quadrupolar D–π–D and A–π–A architectures with similar conjugation and low molecular weight.[127] This highlights the efficiency of the [1,2-*b*]DHIF derivatives for such applications.

In 2012, **[1,2-*b*]-54** (Scheme 15), an organic semiconductor similar to **[1,2-*b*]-4**[67] (Scheme 4) (with four decylphenyl units instead of four tolyl units at C6 and C12) was synthesized and investigated for its multiphoton absorption properties.[128] **[1,2-*b*]-54** was obtained following a route different to that described to prepare **[1,2-*b*]-4** (Scheme 7) as the two diphenylamine donor units were incorporated on the terphenyl intermediate **52** (obtained from **50** and **51**) before the formation of the [1,2-*b*]DHIF core (Scheme 16).

The T_g and T_d of **[1,2-*b*]-54** (200 °C and 435 °C resp.) were slightly higher than those reported for **[1,2-*b*]-4**[67] (183 °C and 420 °C resp.) indicating an increase of the thermal stability due

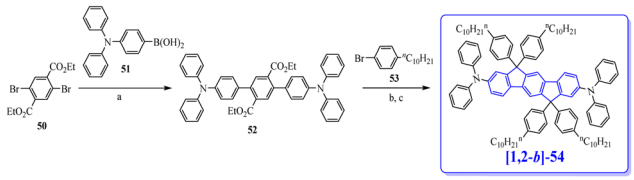

Scheme 16 Synthesis of **[1,2-*b*]-54**. (a) $Pd(AcO)_2$, PPh_3, K_2CO_3, toluene/methanol/H_2O, 85 °C. (b) ^{n}BuLi, THF, −78 °C then RT. (c) CF_3SO_3H in THF/CH_2Cl_2.

to the presence of the decyl groups in **[1,2-*b*]-54**. In toluene, **[1,2-*b*]-54** presented an UV-vis absorption centered at 405 nm (similar to **[1,2-*b*]-4**[67]) and two resolved emission bands at 414 and 443 nm with a high fluorescence quantum yield of 0.85 (slightly blue-shifted compared to **[1,2-*b*]-4** (423, 448 nm[67])). The absorption and emission spectra showed no significant red/blue shifts in different solvents ($CHCl_3$, DMF) suggesting nonpolar ground and excited states. This is due to its D–π–D structure. **[1,2-*b*]-54** exhibited multiphoton upconverted photoluminescence (two-, three-, four- and five-photon) when excited by near infrared femtosecond laser pulses. The multiphoton-excited photoluminescence spectral features were similar to those of the one-photon-excited showing that the emission energy levels were likely to be identical. **[1,2-*b*]-54** presented a 2PA cross-section of 59.6 GM at 810 nm and a 3PA cross-section of 2.02 GM at 1230 nm. In the same work,[128] **[1,2-*b*]-54** parent compounds with longer central ladder-type oligophenylenes (from 4 to 7 bridged phenyls instead of 3 bridged phenyls in **[1,2-*b*]-54**) were also prepared.[128] Their linear and nonlinear optical properties were studied and these longer ladder-type oligomers exhibited very strong multiphoton upconverted photoluminescence as well as blue lasing properties.

[1,2-*b*]-55-**[1,2-*b*]-57**[130] are star-shaped [1,2-*b*]DHIF based dendrimers (Scheme 15) composed of an amine-based central core, with three [1,2-*b*]DHIF arms decorated at C6 and C12 by four non-coplanar decyl-phenyl rings. They also possess either electron-donating carbazole (**[1,2-*b*]-55**), diphenylamine (**[1,2-*b*]-56**) or electron-accepting triazole (**[1,2-*b*]-57**) end caps. The three dendrimers exhibit two absorption bands. The strong absorption band between 380 and 440 nm correspond to the π–π* transition of the rigid [1,2-*b*]DHIF backbones. The weaker absorption around 300–325 nm is due to the n-π* transition of the central triarylamine unit. The emission spectrum presents a blue emission with a quantum yield over 0.84 peaking at 443–450 nm. The three star-shaped organic semiconductors exhibit extremely intense multiphoton induced blue photoluminescence upon excitation at 700, 1270 and 1800 nm corresponding to the two-, three- and four-photon absorption, respectively.

[1,2-*b*]-58[131] and **[1,2-*b*]-59**[131] are analogous to **[1,2-*b*]-55** and **[1,2-*b*]-56** respectively, with a central triazine unit instead of a central nitrogen atom (Scheme 15). Finally, **[1,2-*b*]-60**[131] also belongs to the **[1,2-*b*]-58** and **[1,2-*b*]-59** dendrimer family with a 2-(4-(*tert*-butyl)phenyl)-1,3,4-oxadiazole unit substituting the C7 atom of each of the three [1,2-*b*]DHIF units.

All these star-shaped structures based on the [1,2-*b*]DHIF unit exhibit remarkable efficient multiphoton absorption properties with a 2PA cross-section up to 2579 GM (@700 nm) for **[1,2-*b*]-56** in the nitrogen centered dendrimer series and 2PA cross-section up to 5120 GM (@770 nm) for **[1,2-*b*]-58** in the triazine centered dendrimer series. The comparison of the 2PA cross-section of **[1,2-*b*]-55** and **[1,2-*b*]-58** and that of **[1,2-*b*]-56** and **[1,2-*b*]-59** highlights the advantage of adopting the triazine center ring over the nitrogen atom for the star-shaped skeleton in view of 2PA enhancement. Furthermore, σ_3 of **[1,2-*b*]-58** with maximum 3.3 × 10^{-76} cm^6 s^2 (@1200 nm) is significantly higher than that of **[1,2-*b*]-55** (σ_3: 2.2 × 10^{-76} cm^6 s^2 (@1200 nm)) also showing the key role played by the triazine to improve the π-electron delocalization through the π-network and through-space excitonic interactions for large 3PA enhancements. The lower 2PA cross-section in **[1,2-*b*]-55**, **[1,2-*b*]-57** and **[1,2-*b*]-60** indicate that the end-groups also play a role in the efficiency of the multiphoton absorption.

Another star-shaped molecule based on the [1,2-*b*]DHIF core was also described in the literature.[132] **[1,2-*b*]-61** possesses a central triphenylamine unit linked through a vinyl fragment to three [1,2-*b*]DHIF units each of them substituted at C8 by a diphenylamine unit. The absorption spectrum of **[1,2-*b*]-61** presents a maximum around 420 nm and its emission spectrum was centered at 479 nm with a quantum yield of 0.72 (THF). With the 2PA cross-section up to 5270 GM (@720 nm), **[1,2-*b*]-61** appears to be a superior 2PA-absorbing molecule than all the previous **[1,2-*b*]-55**–**[1,2-*b*]-57**.[130] With a central nitrogen atom and the external diphenylamine units, the 2PA cross-section of **[1,2-*b*]-61** was twice that of **[1,2-*b*]-56** (2579 GM (@700 nm)).[130,131] The presence of less voluminous hexyl units at the bridges in **[1,2-*b*]-61** compared to tolyl units in **[1,2-*b*]-56** may have an influence on the 2PA efficiency of **[1,2-*b*]-61**.

2.6. Other [1,2-*b*]DHIF-based organic semiconductors

In the previous section, all the [1,2-*b*]DHIF-based organic semiconductors presented were incorporated in electronic devices. In this last part, we rapidly present some [1,2-*b*]DHIF-derivatives for which no device application was reported but which deserve to be briefly presented due to the singularity of their electronic properties (Scheme 17). This also allows us to show the versatility of the [1,2-*b*]DHIF core.

In 2005, two rod-like bimetallic ruthenium **[1,2-*b*]-62-Ru** and osmium **[1,2-*b*]-62-Os** complexes bridged by a "phenyl-[1,2-*b*]DHIF-phenyl" core have been synthesized.[133] For both compounds, the UV-vis absorption spectra (CH_3CN) presented first, at 290 nm, the singlet intraligand π–π* transition of the three bipyridine units, then close to 400 nm the absorbance of the "phenyl-[1,2-*b*]DHIF-phenyl" core. The third absorption centered at 466 nm for **[1,2-*b*]-62-Ru** and at 490 nm for **[1,2-*b*]-62-Os** corresponded to the MLCT absorption bands of the bimetallic complexes. Additionally, **[1,2-*b*]-62-Os** showed a weak absorption band (550–700 nm) that was assigned to spin-forbidden electronic transitions (^{3}MLCT) partly allowed due to strong spin-orbit coupling in the osmium complexes. The PL spectra were structureless with a maximum at 624 nm for **[1,2-*b*]-62-Ru** and at 748 nm for **[1,2-*b*]-62-Os**. The oxidation of the two compounds occurred in a single reversible bi-electronic wave

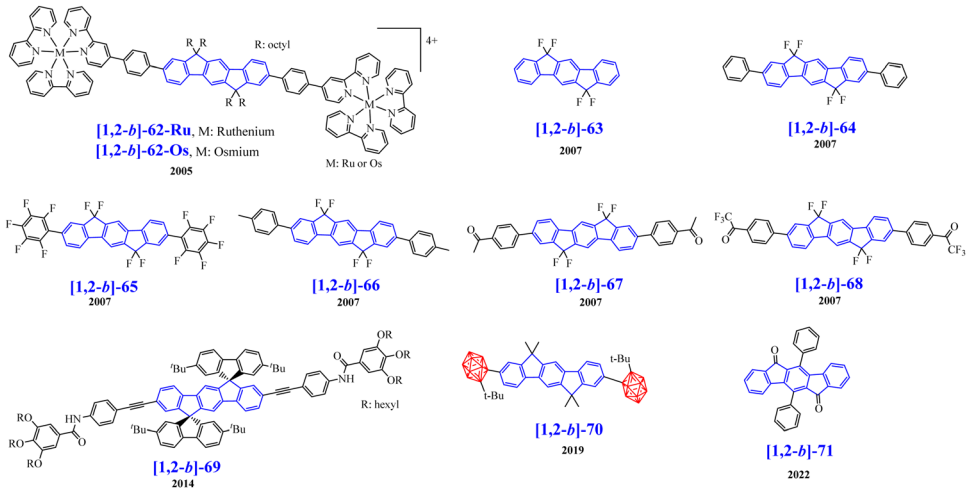

Scheme 17 Molecular structures of **[1,2-*b*]-62-[1,2-*b*]-71**.

centered on the metallic units with a peak at 1.28 V *vs.* SCE for **[1,2-*b*]-62-Ru** and at 0.86 V for **[1,2-*b*]-62-Os** whereas the reduction occurred in three successive reversible waves corresponding to the bipyridine ligand reductions with the first one localized on the phenylene-substituted pyridine. In **[1,2-*b*]-62-Ru** and **[1,2-*b*]-62-Os**, only a weak interaction exists between the two metal centers in the ground state. However, in the excited state, the electronic density is delocalized on the central "phenyl-[1,2-*b*]DHIF-phenyl" spacers.

In 2007, **[1,2-*b*]-63** and a series of extended difluoromethylene-[1,2-*b*]DHIF derivatives (**[1,2-*b*]-64**-**[1,2-*b*]-65**) were synthesized and their electronic properties were compared to those of **[1,2-*b*]-63**.[134] In reduction, **[1,2-*b*]-63** showed a reduction peak potential at −2.46 V *vs.* Fc/Fc^+ whereas that of **[1,2-*b*]DHIF** was at −2.96 V *vs.* Fc/Fc^+.[40] This positive shift of 0.5 V indicates that the electron affinity increases upon the substitution of hydrogen atoms by fluorine atoms at the two bridged positions of **[1,2-*b*]-63**. The UV-vis absorption spectrum of **[1,2-*b*]-63** showed the lowest energy band peaking at 325 nm (THF), blue-shifted compared to **[1,2-*b*]DHIF** (334 nm in THF). A different effect was observed for the emission spectrum, which appeared more red-shifted for **[1,2-*b*]-63** (400 nm in THF) compared to **[1,2-*b*]DHIF** (341, 353 nm in THF), despite no explanation being provided to explain this feature.

The extension of the [1,2-*b*]DHIF core by the substitution at C2 and C8 found in **[1,2-*b*]-64**–**[1,2-*b*]-68**, also leads to modification of the optical properties as exposed above. Compared to the maximum absorption band of **[1,2-*b*]-63** (325 nm) all the absorption maxima were red-shifted upon extension of conjugation with the shift increasing from 22 nm for **[1,2-*b*]-64** with the addition of two phenyl units to 33 nm in **[1,2-*b*]-68** with the addition of two trifluorophenylethanone units. The five extended-[1,2-*b*]DHIF, **[1,2-*b*]-64**–**[1,2-*b*]-68** show blue emission with maxima between 410 nm for **[1,2-*b*]-65** with two pentafluorophenyl units to 436 nm for **[1,2-*b*]-66** with two tolyl units, all red-shifted compared to the maximum highlighted at 400 nm for **[1,2-*b*]-63**. Single crystals of the compounds confirmed the planarity of the central tetrafluoro-[1,2-*b*]DHIF unit and showed different torsion angles between this core and the external phenyl units varying between 7.6° for **[1,2-*b*]-68** and 35.8° for **[1,2-*b*]-64**, driving not only the extension of conjugation but also the π–π intermolecular interactions. The introduction of the carbonyl group on the phenyl in **[1,2-*b*]-67** and **[1,2-*b*]-68** improved the planarity of the molecule as well as the face-to-face packing.

In 2014, our group reported the luminescence modulation in liquid crystalline phases containing the extended **[1,2-*b*]-69**.[135] This organic semiconductor was obtained in a good yield *via* a palladium(0)-catalyzed cross-coupling reaction between the **2,8-Br$_2$-[1,2-*b*]-7** (**28**, Scheme 10) and *N*-(4-ethynylphenyl)-3,4,5-tris(hexadecyloxy)benzamide in *n*-propylamine as a base and solvent. The grafting of *N*-(ethynylphenyl)benzamide fragments carrying hexadecyl carbon chains on the bulky **[1,2-*b*]-7** core has allowed the emergence of strongly luminescent liquid crystalline phases.

In 2019, a planar terphenyl-based *o*-carboranyl compound, **[1,2-*b*]-70** (Scheme 17) was synthesized. It possesses a central [1,2-*b*]-tetramethyl-IF core decorated by two electron-withdrawing *o*-carborane units at C2 and C8.[136] **[1,2-*b*]-70** exhibits low-energy absorption bands at 340 and 356 nm in THF and demonstrates intense emission at 375 and 548 nm. Compared to **[1,2-*b*]DHIF** emission (339, 347, 356 nm),[40] that of **[1,2-*b*]-70** was red-shifted and presented an intense ICT transition between *o*-carborane cages and the central [1,2-*b*]DHIF core.

Finally, in 2022, the optical properties of the aromatic ketone **[1,2-*b*]-71**[137] (Scheme 17) were studied in solution and in crystalline nanostructured films. From those studies it was demonstrated that the crystalline films exhibit enhanced light absorption, amplified emission quantum yields and longer excited state lifetimes compared to diluted solutions. These properties, termed as aggregation-induced delayed fluorescence (AIDF) are promising. AIDF materials are promising emitting layers in non-doped OLEDs.

3. Modification of the indenofluorenyl core using the geometry

3.1. Introduction to the 11,12-dihydroindeno[2,1-*a*]fluorene core: the *para–syn* isomer of [1,2-*b*]DHIF

Despite the **[1,2-*b*]DHIF** isomer being the most studied isomer, another arrangement of the three phenyl units has also been studied in the literature keeping nevertheless the *para*-terphenyl linkages. This isomer, the 11,12-dihydroindeno[2,1-*a*]-fluorene, labelled as **[2,1-*a*]DHIF** (colored in red in Scheme 18) presents different properties than its **[1,2-*b*]DHIF** counterpart. Despite two different routes to indeno[2,1-*a*]fluorenone, **[2,1-*a*]IF(=O)$_2$**, being published in 1934[140] and in 1939,[141] the first synthesis of **[2,1-*a*]DHIF** was described in 1951 by Deuschel[32] (Scheme 18). This first approach consisted in the reduction of **[2,1-*a*]IF(=O)$_2$** obtained by a Diels-Alder addition and aromatization of **54** and **55** leading to **56** itself cyclized in fluorenone **57**, which led to the dione **[2,1-*a*]IF(=O)$_2$**.

In 1963, another access to **[2,1-*a*]DHIF** was described by Schroth *et al.*[138] from the 2,2′-diindenyl **58** and maleic anhydride **55**. In 2010, our group detailed the access to **[2,1-*a*]DHIF** following different routes (Scheme 18).[21] These routes both started with a cycloaddition reaction between 1,4-diphenyl-1,3-butadiene **59** and dimethyl-but-2-ynedioate **60** leading to the 1,4-dihydroterphenyl derivative **61**, itself dehydrogenated to build the terphenyldicarboxylate **62**. The reduction of **62** led to its corresponding diol **64**. The last step was the cyclisation of **64** in **[2,1-*a*]DHIF**. The second route involved the synthesis of **[2,1-*a*]IF(=O)$_2$** by intramolecular cyclisation of **63** in acidic medium, the last step being its reduction in **[2,1-*a*]DHIF**. In 2013, a new route to **[2,1-*a*]DHIF** was described starting from the 2,2′-diindenyl **58** in the presence of (*E*)-1,2-dichloroethene **65**.[139] Finally, in 2014, **[2,1-*a*]DHIF** was obtained in a mixture with **[1,2-*b*]DHIF** (in a 1:4 ratio) through double annulation of terphenyl **13** using a cationic gold complex **14**.[38]

The main physicochemical properties of **[2,1-*a*]DHIF** have been reported by our group in 2010[21] and compared to those of **[1,2-*b*]DHIF** presented above.[40] The structural analysis shows that the positioning of the two bridges in a *syn* arrangement leads to a contraction of the DHIF core compared to **[1,2-*b*]DHIF** (10.76 *vs.* 11.05 Å). This contraction and particularly the short distance between the two bridges in a *syn* arrangement (3.35 Å) will play a key role in the development of the **[2,1-*a*]DHIF** isomer (see below). The UV-vis absorption spectrum of **[2,1-*a*]DHIF** (THF) presents well-defined absorption bands with maxima at 307, 315 and 322 nm, blue-shifted by 12 nm compared to that of **[1,2-*b*]DHIF** (319, 328, 334 nm) providing a gap expansion (3.76 eV for **[2,1-*a*]DHIF** *vs.* 3.61 eV for **[1,2-*b*]DHIF**).[40] This indicates a better delocalization of π-electrons in **[1,2-*b*]DHIF** than in **[2,1-*a*]DHIF**. Similarly, the emission spectrum of **[2,1-*a*]DHIF** presents two main bands at 326 and 343 nm, hypsochromically shifted by 13 nm compared to **[1,2-*b*]DHIF**. Due to its rigid and planar structure, the Stokes shift was very small (4 nm) and **[2,1-*a*]DHIF** was highly fluorescent ($\varnothing^{sol}$: 0.6 in THF).

The first oxidation of **[2,1-*a*]DHIF** (Fig. 7A) is reversible and occurs at a potential of 1.31 V *vs.* SCE identical to the one reported for **[1,2-*b*]DHIF**.[48] The HOMO and LUMO levels of **[2,1-*a*]DHIF** were of −5.62 and −1.94 eV, quite similar to those reported for **[1,2-*b*]DHIF** (−5.61 and −1.99 eV). After this first oxidation, an irreversible wave is observed (1.98 V, Fig. 7B) almost identical to that reported for its positional isomer (2.01 eV).[48] Recurrent scans involving the two oxidation waves lead to a regular electropolymerization process (see the arrows in Fig. 7C).[21] As described in Fig. 7D, poly**[2,1-*a*]DHIF** appears

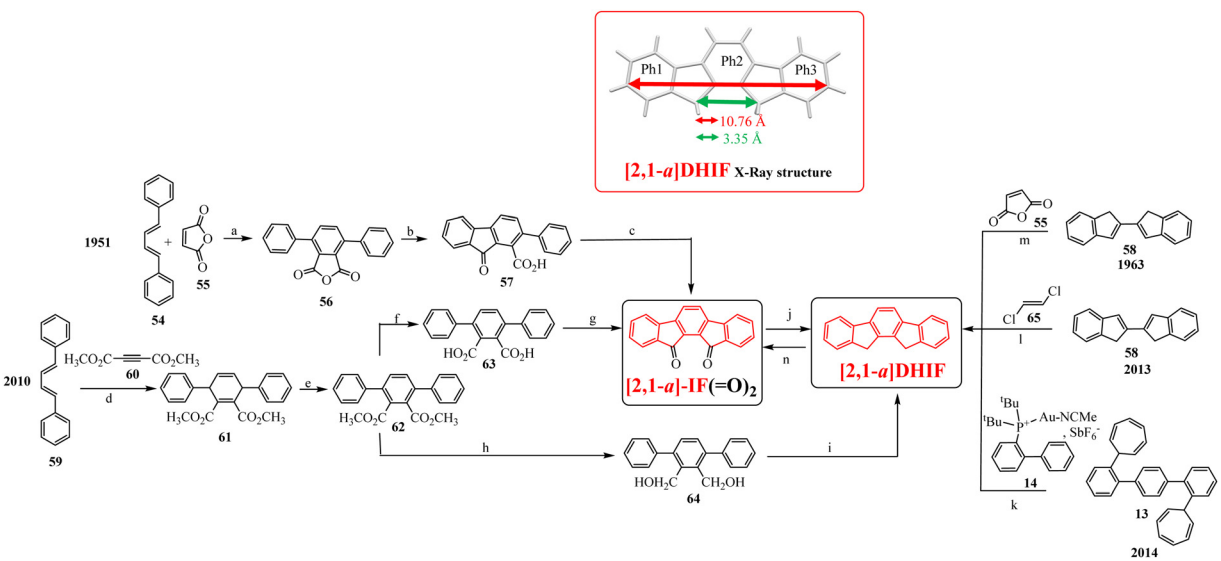

Scheme 18 Different routes to [2,1-*a*]DHIF[21,32,38,138,139] or [2,1-*a*]IF(=O)$_2$[32,140,141] and [2,1-*a*]DHIF X-ray structures. (a) Experimental conditions not available, (b) $AlCl_3$, CS_2, (c) $SOCl_2$, CCl_4, H_2SO_4, (d) toluene, reflux, (e) toluene, Pd/C reflux, (f) NaOH /EtOH, reflux, (g) H_2SO_4, 140 °C, (h) DIBAL, DCM, (i) PPA, 1,2-dichlorobenzene, 140 °C, (j) NH_2-NH_2, H_2O/KOH, diethyleneglycol 180 °C, (k) DCE, 120 °C, (l) 230 °C in sealed glass tube, (m) not available, and (n) CrO_3, acetic anhydride.

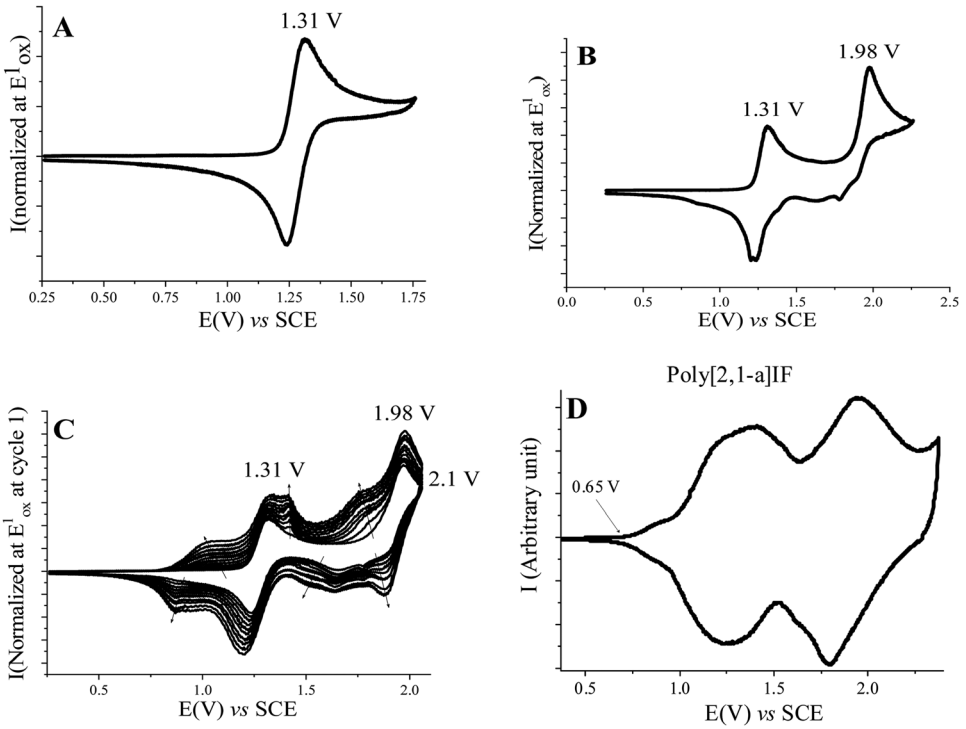

Fig. 7 Cyclic voltammetry at 100 mV s^{-1} in CH_2Cl_2/[NBu_4][]PF_6] 0.2 M. A. **[2,1-*a*]DHIF**, 1 cycle between 0.25 and 1.76 V, B. **[2,1-*a*]DHIF**, 1 cycle between 0.25 and 2.27 V, C. **[2,1-*a*]DHIF**, 10 cycles between 0.25 and 2.1 V and D. modified electrode (5 cycles between 0.25 and 2.27 V in the presence of [2,1-*a*]DHIF) investigated in the absence of [2,1-*a*]DHIF, with 3 cycles between 0.4 and 2.4 V.

stable in a wide potential range between 0.4 and 2.4 V *vs.* SCE, larger than that reported for poly**[1,2-*b*]DHIF**,[48] indicating the higher stability of the polymer and also a lower HOMO level (−5.04 eV *vs.* −5.15 eV).

Contrary to [1,2-*b*]DHIF derivatives, which have been used as active materials in different OE devices (OLED, PhOLED, OFET, OPV, *etc.*, see above), [2,1-*a*]DHIF derivatives have been principally used as active materials in fluorescent OLEDs. As the synthesis of **[2,1-*a*]DHIF** is not even currently widely developed, this could be the reason for this lack of application. The main characteristic used to date is its geometry with the two bridges on the same side of the [2,1-*a*]DHIF plane. This can allow us to force π–π interactions between two fragments attached at these positions. The examples using such an approach are described below.[19,20,22,75,142]

3.2. Excimer emission of [2,1-*a*]DHIF-based organic semiconductors

The first isolation of a [2,1-*a*]DHIF-based molecule, in our group, was not expected.[19] Indeed, in 2008, during the synthesis of **[1,2-*b*]-DSF(^{t}Bu)$_4$-IF**, starting from the 2,2''-diiodoterphenyl **26** and the 2,7-di^{t}Bu-fluorenone, a second isomer with a [2,1-*a*]DHIF core was also isolated (Scheme 19).

The two isomers were formed during the bicyclization of the difluorenol intermediate. In 2009, our group decided to investigate the regioselectivity of this reaction and we observed that the *anti*/*syn* ratio of isomers formed could be modified as a function of different parameters: the temperature, the solvent and the substituents attached on the fluorenone. This reaction and the physicochemical properties of different couples of isomers have been then intensively studied and detailed in different publications.[19,20,22,59,75,142,143]

We have proposed that the bicyclization of the difluorenol intermediate (Fig. 8, Left) unfolds sequentially.[143] The first ring closure gives a 2-substituted spirobifluorene (see pro-conformers in Fig. 8) and the second one provides the corresponding [2,1-*a*]DHIF and [1,2-*b*]DHIF core (*via* a pro-Wheland intermediate).

In this second step, the cyclisation can occur either on the opposite sides leading to the *anti* isomer with the [1,2-*b*]DHIF geometry or on the same side of the first cyclisation, leading to the *syn* isomer with the [2,1-*a*]DHIF geometry. This powerful reaction was then further investigated to develop structurally related materials for electronics (another mechanistic study was also reported in 2019[144]).[20,22,27,59,75,142]

The most influential parameter on the selectivity of this cyclization reaction is the nature of the R groups attached (see some examples in Scheme 19). As R becomes more encumbering (from R═H to R═3,5-di-^{t}butylphenyl), the distribution shifts towards the formation of [2,1-*a*]-isomers at the expense of [1,2-*b*]-isomers. With a very bulky substituent attached, R = 3,5-di-^{t}butylphenyl, the reaction becomes regioselective exclusively providing **[2,1-*a*]-DSF(3,5-di-^{t}BuPh)$_4$-IF** (see the structure in Scheme 19). Thus, despite the [2,1-*a*] isomers being less energetically stable than their [1,2-*b*] counterparts, their formation was favoured by sterically hindered substituents.[143]

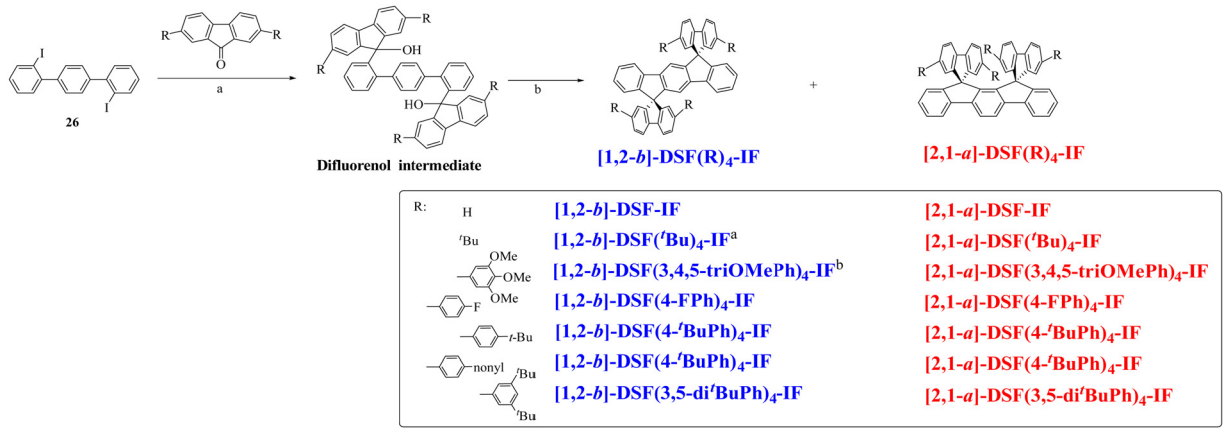

Scheme 19 Synthesis of **[1,2-*b*]-DSF(R)$_4$-IF** and **[2,1-*a*]-DSF(R)$_4$-IF**. (a) ^{n}BuLi, THF, −78 °C to RT, (b) CH_3CO_2H/HCl, 100 °C ([a]: named **[1,2-*b*]-7** in Scheme 4,[b]: named **[1,2-*b*]-9** in Scheme 4).

Mechanistic investigations have shed light on this intriguing feature and have revealed that the selectivity towards [2,1-*a*] isomers is increased by the solvent, substituent and temperature. This involves the relative locking of the sterically hindered rotamers in the more stable *pro*-[2,1-*a*]-conformation due to a high energy barrier for the interconversion to the *pro*-[1,2-*b*]-conformation (Fig. 8).[143,144] Thus, in this reaction, the [2,1-*a*] isomers are favoured by (i) high polarity solvents, (ii) high temperature and (iii) bulky R groups providing an interesting degree of control.

The photophysical properties of the two families of regioisomers have also appeared to be very different as a function of the substituents attached on the fluorenes. With non-aryl substituents at C2/C7 of the fluorenyl units (H or ^{t}Bu, see the structures in Scheme 19), the physicochemical properties of the two isomers remain similar (see the emission of **[1,2-*b*]-DSF-IF**/**[2,1-*a*]-DSF-IF** in blue/red straight lines, Fig. 9A1/A2). However, if aryl units are attached on the fluorenes as in the couples **[1,2-*b*]-DSF(4-^{t}BuPh)$_4$-IF** – **[2,1-*a*]-DSF(4-^{t}BuPh)$_4$-IF** or **[1,2-*b*]-DSF(4-FPh)$_4$-IF** – **[2,1-*a*]-DSF(4-FPh)$_4$-IF**, the emission properties of the two regioisomer families become different. Indeed, **[1,2-*b*]-DSF(4-^{t}BuPh)$_4$-IF** and **[1,2-*b*]-DSF(4-FPh)$_4$-IF** are violet emitters (blue dotted lines in the 350–450 nm wavelength range in Fig. 9A1) whereas **[2,1-*a*]-DSF(4-^{t}BuPh)$_4$-IF** and **[2,1-*a*]-DSF(4-**

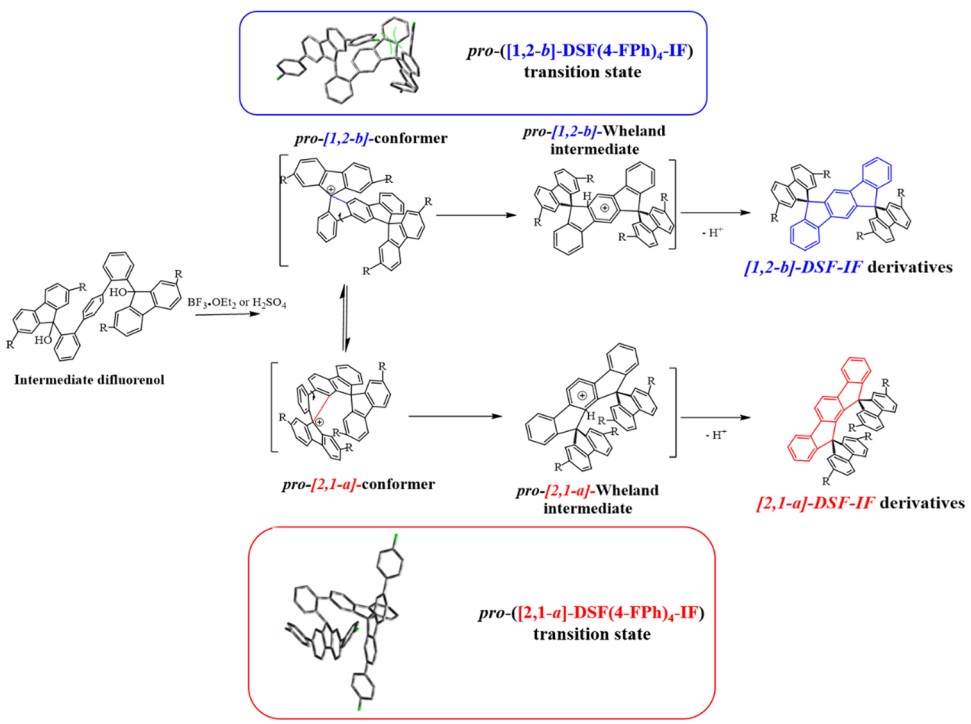

Fig. 8 Middle: Cyclization reaction of difluorenols with the corresponding intermediates hypothesized.[143] Top and Bottom: Modelization of *pro*-**([1,2-*b*]-DSF(4-FPh)$_4$-IF)** and *pro*-(**[2,1-*a*]-DSF(4-FPh)$_4$-IF**) transition states[144] showing the postulated steric hindrance at the origin of the selectivity observed.

FPh)$_4$-IF are blue emitters (red dotted lines in Fig. 9A2). The modulation of the emitted light colour is also highlighted in Fig. 9B for **[1,2-*b*]-DSF(4-FPh)$_4$-IF**/**[2,1-*a*]-DSF(4-FPh)$_4$-IF** isomers. This feature is due to emission arising in the case of the **[2,1-*a*]-DSF(aryl)$_4$-IF**, from the interactions between the two cofacial "aryl-fluorene-aryl" arms. This is directly induced by the particular geometry of the indeno[2,1-*a*]fluorenyl core.[75]

The **[2,1-*a*]-DSF(aryl)$_4$-IF** family also presents original tuneable emission properties since the emission wavelength can be modulated by the steric hindrance induced between the substituted phenyl rings. When the substituent borne by the phenyl unit is bulky such as a *tert*-butyl group in **[2,1-*a*]-DSF(4-^{t}BuPh)$_4$-IF**, the two "aryl-fluorene-aryl" arms move away from each other lessening the cofacial interaction. This results in an hypsochromic shift of the emission band *vs.* **[2,1-*a*]-DSF(FPh)$_4$-IF**.[75]

The two **DSF(R)$_4$-IF** families (R: H; Alkyl or Aryl) also present different electrochemical properties as presented in Fig. 9E. In the case of **[1,2-*b*]-DSF(R)$_4$-IF**, the first oxidation occurs either on the [1,2-*b*]-IF core or on the external "aryl-fluorene-aryl" arms or even on the three π-systems depending on the nature of the substituents borne by the fluorenyl units.[59] Due to these effects, the first oxidation potential varies between 1.16 V for **[1,2-*b*]-9** to 1.47 V for **[1,2-*b*]-DSF-IF** (Scheme 19). In the case of the **[2,1-*a*]-DSF(R)$_4$-IF** family, the specific geometry leads to a face-to-face arrangement of the "aryl-fluorene-aryl" arms and shifts the first oxidation potential to lower values (between 1.07 V for **[2,1-*a*]-DSF(3,4,5-tri-OMePh)$_4$-IF** to 1.36 V for **[2,1-*a*]-DSF-IF**). Depending on the interaction between the face-to-fac e "aryl-fluorene-aryl" in the **[2,1-*a*]-DSF(aryl)$_4$-IF** family, the first oxidation was assigned to an oxidation centered on the "aryl-fluorene-aryl" cofacial dimer. The intramolecular interaction in **[2,1-*a*]-DSF(4-FPh)$_4$-IF** is clearly highlighted in its X-ray structure provided in Fig. 9C.

In 2011 and 2012, our group synthesized two specific blue emitting fluorophores based on the [2,1-*a*]-IF core, incorporating pending fluorene units **[2,1-*a*]-73**[142] or trimethoxyphenyl units **[2,1-*a*]-74**[22] following the route presented above in Scheme 19. These two derivatives, presented in Fig. 10 with their respective **[1,2-*b*]**-isomers **[1,2-*b*]-72** and **[1,2-*b*]-9**, were used as the EML in fluorescent OLEDs. The idea was to show that intramolecular interactions occurring in [2,1-*a*]-derivatives can be used to produce blue light in a device.

The two isomers were stable with T_d of 215 and 320 °C for **[2,1-*a*]-73** and **[1,2-*b*]-72** respectively. The UV-vis absorption spectrum of **[1,2-*b*]-72** displayed one maximum at 347 nm whereas that of **[2,1-*a*]-73** displayed a maximum at 343 nm (THF). The low energy bands were similar to those of the terfluorene[145] or other terfluorenyl oligomers,[146–150] showing that the electronic properties were driven by the terfluorenyl fragments. Thus, **[2,1-*a*]-73** and **[1,2-*b*]-72** presented a similar optical gap of 3.15 eV close to that of terfluorenyl derivatives. Both isomers exhibited deep blue emission in solution with however different spectra. The **[1,2-*b*]-72** spectrum was well defined with maxima at 395 and 417 nm fitting the emission spectrum of the terfluorene and indicating an emission from terfluorenyl arms. The **[2,1-*a*]-73** emission spectrum was different. It was larger, less structured and red-shifted (402, 422 nm). The shoulder at *ca.* 450 nm was also more intense with a tail up to *ca.* 600 nm. This emission shoulder at 450 nm has been assigned to frustrated intramolecular interactions between the two face-to-face terfluorenyl units (see above, Fig. 9). In this

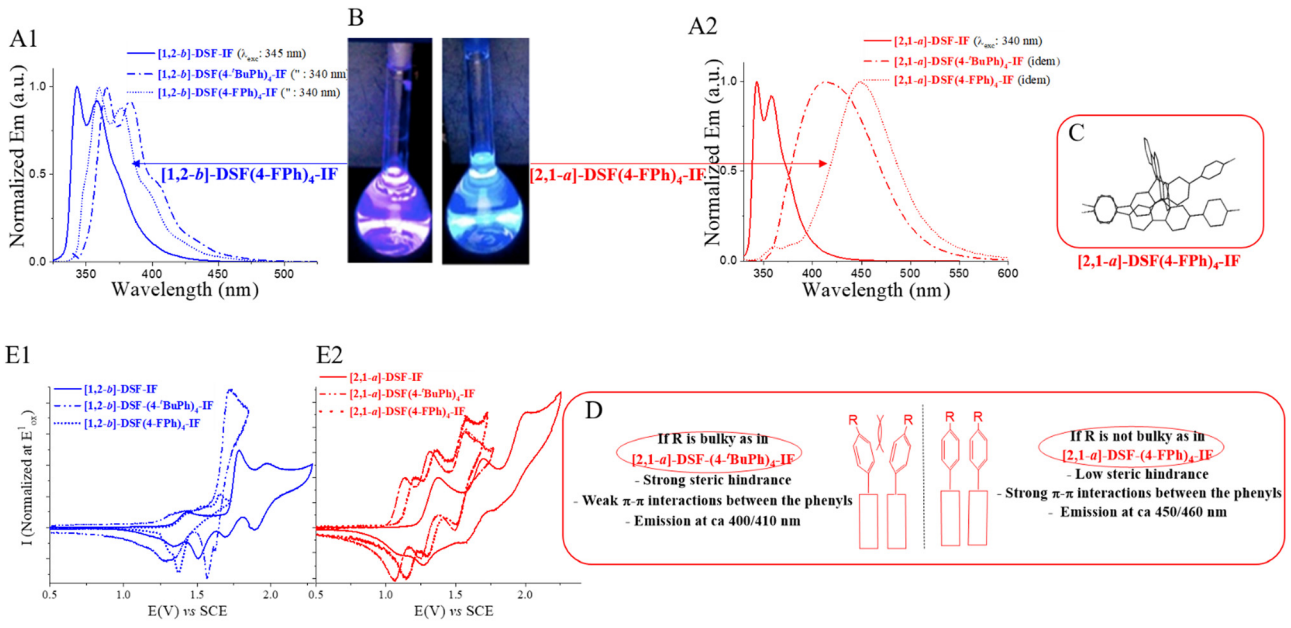

Fig. 9 (A) Emission spectra in THF of **[1,2-*b*]-DSF(R)$_4$-IF** derivatives (A1 in blue) and **[2,1-*a*]-DSF(R)$_4$-IF** derivatives (A2 in red), (B) photograph of the light emitted by **[1,2-*b*]-DSF(4-FPh)$_4$-IF** (left) and of **[2,1-*a*]-DSF(4-FPh)$_4$-IF** (right) (λ_{exc} = 365 nm), (C) X-Ray structure of **[2,1-*a*]-DSF(4-FPh)$_4$-IF**, (D) schematic representation of the impact of the substituent on the structural and electronic properties of the **[2,1-*a*]-DSF(aryl)$_4$-IF** series, (E) cyclic voltammetry in the oxidation of **[1,2-*b*]-DSF(R)$_4$-IF** derivatives (E1 in blue) and **[2,1-*a*]-DSF(R)$_4$-IF** derivatives (E2 in red).

case, the long octyl chains were considered responsible for the sterically hindered environment. Before using the two isomers as the EML in fluorescent OLED, their solid state emission spectra and their stability with the temperature were studied. For **[1,2-*b*]-72**, at room temperature, the solid state emission spectrum was similar to that in solution indicating no specific intermolecular interactions involving the π-systems in the film. This spectrum remained stable from RT to 150 °C, however at higher temperature, a green emission band[11,56,58,151–155] started to grow and became intense after one night at 200 °C. In contrast, the solid state emission spectrum of **[2,1-*a*]-73** appeared different to its solution spectrum with a non-structured main band centred at 464 nm and weak shoulders at 405 and 437 nm. The main emission was attributed to intramolecular excimer formation arising from stacked face-to-face terfluorenyl units and the shoulder to non-stacked terfluorenyl units.

[2,1-*a*]-73 was finally used as the EML in a single layer OLED device (SL-OLED30, Table 7).[142] Despite very low performances, the EL spectrum was in perfect accordance with the **[2,1-*a*]-73** emission spectrum. The blue emission arose from the electro-generated intramolecular terfluorenyl excimers.

As another example, **[1,2-*b*]-9** and **[2,1-*a*]-74** both possessing four 3,4,5-trimethoxyphenyl units grafted at C2/C7 of their two fluorene units (Fig. 10) have shown that the emission of such compounds was mainly driven by the "aryl-fluorene-aryl" arms in **[1,2-*b*]-9** and by face-to-face "aryl-fluorene-aryl" dimers in **[2,1-*a*]-74**. Interestingly, as for **[2,1-*a*]-73**, the emission of **[2,1-*a*]-74** in the solid state was almost unchanged compared to its solution spectrum showing the stability of this type of emission.

SL-OLED31 and OLED32, Table 7, both using **[2,1-*a*]-74** as the EML have been studied and compared to that using **[1,2-*b*]-9** as the EML (SL-OLED13 and OLED14) (Table 1). Comparing SL-OLED13 and SL-OLED31, one notes a lowering of the V_{on} (7.2 *vs.* 5.0 V) and a global increase of the other characteristics particularly the luminance, which was doubled. Concerning the EL spectra, that of SL-OLED31 (CIE: 0.19, 0.19) appears shifted to a shorter wavelength compared to that of SL-OLED13 (CIE: 0.24, 0.24) indicating the efficiency of excimer emission to achieve purer blue light. A comparison of the performance of OLED14 with **[1,2-*b*]-9** as the EML and OLED32 with **[2,1-*a*]-74** as the EML also shows the interest of the intramolecular excimer emission from **[2,1-*a*]-74** compared to **[1,2-*b*]-9** with a lower V_{on}, a higher luminance and an emission at shorter wavelength.

Beyond the performances, which were very low, these studies have evidenced the possibility to generate stable blue light with intramolecular interactions arising from the [2,1-*a*]DHIF core.

3.3. Other organic semiconductors based on the [2,1-*a*]DHIF core

Despite several other organic semiconductors based on the [2,1-*a*]DHIF core being described in the literature (see the examples in Scheme 20), none of them have been used as the active material in OE devices. The particular geometry of the core has been however beneficially used to construct different molecules with specific properties. For example, in 2011, the electrophilic transannular cyclization of octadehydrodibenzo[12]annulene (**66**) was examined and revealed the formation of an *anti* and a *syn* isomer of the IF-dione. More precisely, the reaction of **66** in the presence of iodine leads to a mixture of **[2,1-*a*]-75** and its [1,2-*b*]-isomer in one step. On the other hand, the reaction of **66** in the presence of bromide leads to **[2,1-*a*]-76** and its [1,2-*b*]-isomer in two steps. The ratio of one isomer *vs.* the other was not reported in the publication.

In 2016, the polycyclic hydrocarbon **[2,1-*a*]-77** with a twisted cyclooctatetraene (COT) core fused by two [2,1-*a*]DHIF units was synthesized by stepwise cycloaddition of the *in situ* generated non-aromatic bromo derivative **11-Br-[2,1-*a*]DHIF** obtained from its dibromo-parent **11,12-Br$_2$-[2,1-*a*]DHIF** by HBr elimination. X-Ray crystallographic analysis of **[2,1-*a*]-77** indicated the twisted conformation of the central COT core (see the inset in Scheme 20). This central core was moderately antiaromatic as indicated by the NICS value (+11.9). **[2,1-*a*]-77** is a highly conjugated molecule which displays an absorption at 634 nm extending to about 850 nm in accordance with the gap of 2.21 eV theoretically estimated by the DFT calculations.[157]

In 2017, a nanohoop, **[2,1-*a*]-78** incorporating three **[2,1-*a*]IF(=O)$_2$** units has been synthesized using the "banana shape" of the [2,1-*a*]DHIF core. **[2,1-*a*]-78** has been synthesized from a preformed macrocycle **68** constituted of 9 phenyl rings linked in *para* positions in which three phenyls were disubsti-

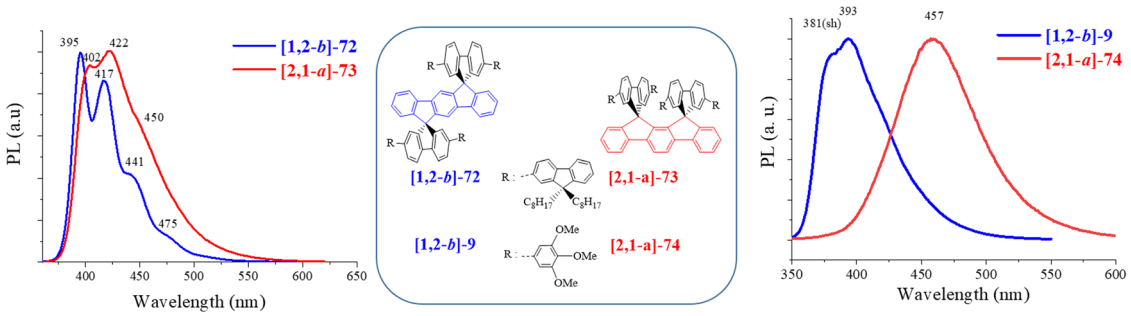

Fig. 10 [2,1-*a*]DHIF-based organic semiconductors used as the EML in fluorescent OLEDs (**[2,1-*a*]-73** and **[2,1-a]-74**) and their respective [1,2-*b*]-isomers(**[1,2-*b*]-72** and **[1,2-*b*]-9**), fluorescent spectra of the four compounds.

Table 7 Performance of devices with [2,1-*a*]DHIF-based (**[2,1-*a*]-73-[2,1-*a*]-74**) as the EML

Device	Device architecture	V_{on} (V)	CE (cd A^{-1})	PE (lm W^{-1})	Luminance (cd m^{-2})	λ_{max} (nm) CIE (x, y)	Ref.
SL-OLED30	ITO/PEDOT:PSS/**[2,1-*a*]-73** (50 nm)/Ca	7.0	0.05	—	100	464 nm (0.19, 0.23)	142
SL-OLED31	ITO/PEDOT:PSS/**[2,1-*a*]-74** (30 nm)/Ca	5.0	0.037	0.018	100	447 (0.19, 0.19)	22
OLED32	ITO/PEDOT:PSS/NPB (40 nm)/**[2,1-*a*]-74** (45 nm)/Ca	5.8	0.1	0.002	510	462 (0.19, 0.18)	22

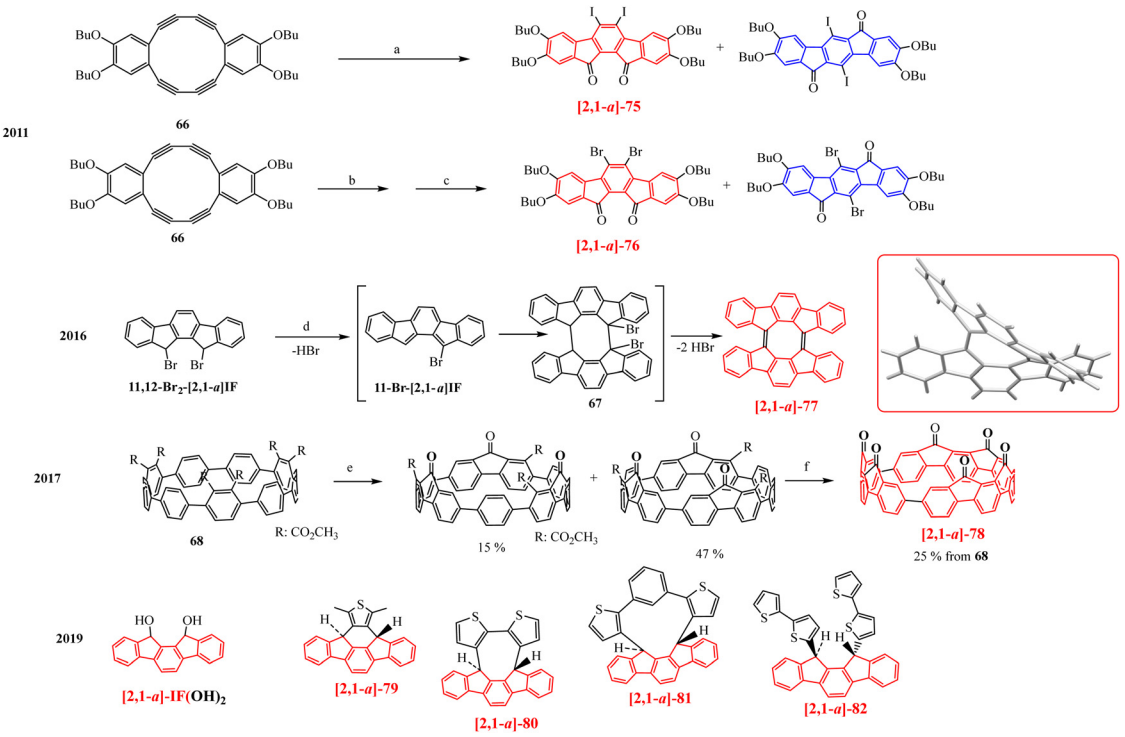

Scheme 20 Synthesis of different [2,1-*a*]DHIF-based organic semiconductors reported in literature.[156–159] Synthesis of **[2,1-*a*]-75**: (a) I_2, O_2 in benzene. Synthesis of **[2,1-*a*]-76**; (b) Br_2 in DCM then, (c) NaOAc, AcOH in DCM. Synthesis of **[2,1-*a*]-77**: (d) ^{t}BuOK in THF. The inset is the X-ray structure of **[2,1-*a*]-77** from Cambridge Data Base No. 1474507. Synthesis of **[2,1-*a*]-78**: (e) trifluoroacetic acid, trifluoroacetic anhydride in MeOH, 75 °C; f) P_2O_5, MsOH, 75 °C.

tuted in the *ortho* position by two CO_2CH_3 groups. Different synthetic pathways were described in this work finally leading to **[2,1-*a*]-78** from **68** in a 25% yield in a two-step process. The UV-vis absorption spectrum of **[2,1-*a*]-78** displayed several bands at 288, 379 and 408 nm and the fluorescence spectrum had bands at 448 and 606 nm. Although fluorene[160] and other bridged oligophenylenes such as carbazole[161] have been integrated in nanohoops, **[2,1-*a*]-78** is to date the only example of this macrocycle incorporating a [2,1-*a*]DHIF building unit. The presence of three carbonyls in the present ring is of interest for further functionalization of this macrocycle and more generally for the development of nanohoops in electronics.

Finally, in 2019, [2,1-*a*]-IF-derivatives decorated by thiophene cyclic compounds, **[2,1-*a*]-79-82**, were synthesized by superelectrophilic Friedel–Crafts reaction between **[2,1-*a*]-IF(OH)$_2$** and thiophene building units.[159] The photophysical properties of the four **[2,1-*a*]-79-82** were studied and compared to that of **[2,1-*a*]-IF(OH)$_2$**. The UV-vis absorption and emission spectra of **[2,1-*a*]-79-81** were almost similar with λ_{abs} at *ca.* 310 and 325 nm and λ_{em} at *ca.* 350 nm. Moreover, compared to **[2,1-*a*]-IF(OH)$_2$** and **[2,1-*a*]-82**, **[2,1-*a*]-79-81** presented a higher fluorescence quantum yield (2/5% for **[2,1-*a*]-IF(OH)$_2$**/**[2,1-*a*]-82** *vs.* 29/47/52% for **[2,1-*a*]-79/80/81**) which may be correlated to the rigidity of the molecular structures.

4. Modification of the indenofluorenyl core *via* terphenyl linkages: dihydroindeno[1,2-*a*]fluorenyl-, dihydroindeno[2,1-*b*]fluorenyl- or dihydroindeno[2,1-*c*]fluorenyl-based organic semiconductors

Modification of the indenofluorenyl core *via* the arrangement of the phenyl linkages from *para*-terphenyl (described above in [1,2-*b*]DHIF derivatives or in [2,1-*a*]DHIF derivatives) to *meta*-terphenyl provides the *meta* isomers, namely, 7,12-dihydroindeno[1,2-*a*]fluorene

(called the *meta–anti* isomer) and 5,7-dihydroindeno[2,1-*b*]fluorene (called the *meta–syn* isomer) (see **[2,1-*b*]DHIF** and **[1,2-*a*]DHIF** in orange and green in Scheme 1). These two positional isomers have revealed, over the years, the importance of the linkage and the geometry on the electronic properties.[23–25] The 5,8-dihydroindeno[2,1-*c*]fluorene is the last isomer in the DHIF family. This isomer displays a *syn* geometry induced by the central *ortho*-terphenyl core. The *ortho* linkage gives this isomer unique characteristics and notably, from a structural point of view, a helicoidal turn of the DHIF unit (see **[2,1-*c*]DHIF** in pink, Scheme 1). Their properties and specific use in OE are described in the last part of this review.

4.1. Synthesis of [1,2-*a*]DHIF, [2,1-*b*]DHIF and [2,1-*c*]DHIF

The oldest synthesis to **[1,2-*a*]DHIF** involve both the synthesis of the dione **[1,2-*a*]IF(=O)$_2$** following two different routes starting from the bis-indene-dione **69** (Radulescu in 1939[162]) or from the (*o*-chlorobenzylidene)-9-fluorene **72** (Chardonnens in 1955[163]), Scheme 21. In 1967, Kemp *et al.*[164] prepared **[1,2-*a*]DHIF** directly from the bis-indene **75**. The diene system of **75** reacted with maleic anhydride **55** to give **76**, which was aromatized in **[1,2-*a*]DHIF** following the Altman and Ginsburg method.[165] In 1970, Chardonnens[166] reported another access to **[1,2-*a*]DHIF** also involving **[1,2-*a*]IF(=O)$_2$**. This synthesis started by the condensation of the α-methylchalcone **77** and the diethylcetone **78** leading to the trimethyl-2,4,6-diphenyl-3,5-cyclohenen-2-one **79**, which was then transformed into the triacid **80** following a four steps process. The double cyclisation of **80** led to the dione **71**, which was converted in **[1,2-*a*]IF(=O)$_2$** as reported in 1939 by Radulescu.[162]

The first synthesis of **[2,1-*b*]DHIF** was reported in 1945 (see Scheme 22) from a trinuclear by-product of ellagic acid **81** through zinc dust distillation.[167] The name of ellagene was given early to **[2,1-*b*]DHIF**. In 1951, Deuschel reported the access to **[2,1-*b*]DHIF**[168] starting by the condensation of **82** and **83** leading to **84**, which was aromatized in **85**. The [2,1-*b*]DHIF core was constructed by double cyclization of **85** giving **86**, itself dehydroxylated in **[2,1-*b*]DHIF**. Different routes to **[2,1-*b*]DHIF**, all involving, in the last step, the hydrogenation of the dione **[2,1-*b*]IF(=O)$_2$**, were then described starting from different terphenyls[168–170] or fluorene derivatives.[171]

The condensation of **82** with the diethylcetone **78** leads to the *meta*-terphenyl **87**, of which double cyclization led to **[2,1-*b*]IF(=O)$_2$** and to **[2,1-*b*]DHIF**.[169] Access to the dione was also described, in 1959, from the 2-substituted fluorenone **88** or the 2-substituted fluorene **89** (*via* the monocetone **[2,1-*b*]IF(=O) 90**).[171] More recently, in 2015, our group prepared the **[2,1-*b*]IF(=O)$_2$** from the terphenyl **91**.[170]

Finally, the synthesis of the last positional isomer, **[2,1-*c*]DHIF**, also originates from the sixties (Scheme 23) and involves either the condensation of bis-indene **92** and maleic anhydride **55**[172] or, in a longer process, the syntheses of dione **[2,1-*c*]IF(=O)$_2$** from the propiophenone **94**.[173]

Other [2,1-*c*]-IF-based π-conjugated systems, differently substituted, have also been synthesized together with some oligomers and polymers.[174–176] Although their photophysical and electrochemical properties have been, in some cases, evaluated, no device applications of the monomers were reported.

The literature only reports a few properties of the five DHIF isomers themselves and no comparative studies of these properties. Concerning the thermal properties, the literature reports a melting point of 140 °C for **[2,1-*c*]DHIF** and of 203 °C/212–213 °C or 215–220 °C for **[2,1-*a*]DHIF**/**[1,2-*a*]DHIF** or **[2,1-*b*]DHIF** respectively. The only data available is a high decomposition temperature of 200 °C reported for **[1,2-*b*]DHIF**.[40]

The UV-vis absorption spectra reported in different studies show a red-shift of the lowest energy absorption bands from 314 nm for **[2,1-*c*]DHIF**[165] to 334 nm for **[1,2-*b*]DHIF**[40] with intermediate values of 321/322 and 332 nm for **[1,2-*a*]DHIF**[164]/**[2,1-*a*]DHIF**[21] and **[2,1-*b*]DHIF**[170] respectively. These values are in accordance with an extension of conjugation in the DHIF core from the less conjugated *ortho*-DHIF to the more conjugated *para*-DHIF with a weaker modulation in the *para–syn*-isomer and in the two *meta* isomers.

As far as we know, emission properties have only been reported for three isomers (no data found for **[2,1-*c*]DHIF** or

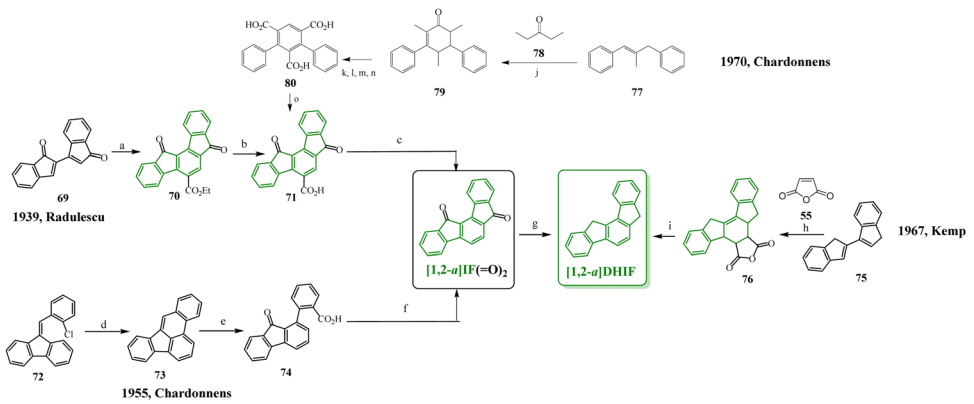

Scheme 21 Different routes to **[1,2-*a*]DHIF**[164] or **[1,2-*a*]IF(=O)$_2$**.[162,163,166] Access to **[1,2-*a*]IF(=O)$_2$** from **69**: (a) EtOH, NaOEt, $ICH_2CH_2CO_2C_2H_5$, (b) KOH, HCl, (c) heating in sublimation apparatus; or from **72**: (d) conditions not available, (e) $Na_2Cr_2O_7$, 60 °C, (f) H_2SO_4, 140 °C; or from **77**: (j) C_2H_5ONa, (k) Dioxane, 75 °C, $NaBH_4$, (l) H_2O, PdC, 295–315 °C, (m) pyridine/H_2O, $KMnO_4$, (n) Na_2CO_3 25%, $KMnO_4$, and (o) H_2SO_4. Access to **[1,2-*a*]DHIF** from **[1,2-*a*]IF(=O)$_2$**: (g) zinc reduction or from **75**: (h) *p*-xylene, reflux, (i) Cu powder, $Ba(OH)_2$ and soda-glass, heating to 400 °C in an inert atmosphere.

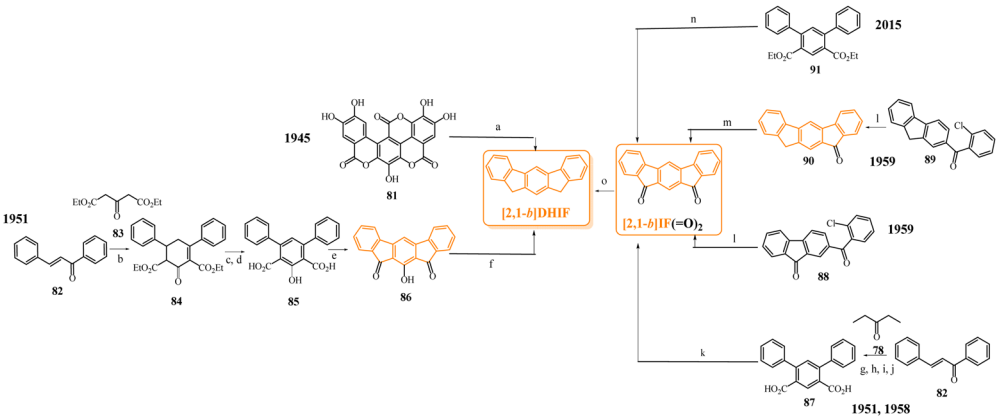

Scheme 22 Different routes to **[2,1-*b*]DHIF**[167,168] or **[2,1-*b*]IF(=O)$_2$**[168–171] described in the literature. Access to **[2,1-*b*]DHIF** from **81**: (a) zinc dust distillation or from **82**: (b) ethanol, piperidin, 40 °C, (c) ethylacetate, N-bromosuccinimide, Br_2, (d) KOH 20% in methanol, (e) H_2SO_4 concentrated, and (f) pyridine, zinc dust, H_2SO_4. Access to **[2,1-*b*]DHIF** *via* **[2,1-*b*]IF(=O)$_2$**, from **82**: (g) NaOH/EtOH, reflux H_2SO_4/H_2O, (h) Ether/H_2O, Na, cooling to 0 °C then H_2SO_4 concentrated, (i) Pd/C, 280–300 °C, (j) pyridine/H_2O, 90 °C, then $KMnO_4$, (k) H_2SO_4 concentrated 70–80 °C, or from **88**: (l) quinoline, NaOH/H_2O, 250 °C, then RT and transfer in HCl 12%, or from **89**: (l) quinoline, NaOH/H_2O, 250 °C, then RT and transfer in HCl 12%, (m) oxidation or from **91**: (n) MsOH 120 °C. Reduction of **[2,1-*b*]IF(=O)$_2$** in **[2,1-*b*]DHIF**, (o): NH_2NH_2/KOH.

for **[1,2-*a*]DHIF**). The three compounds present structured emission spectra with small Stokes shifts (below 5 nm) and emission maximum increasing from 326 to 337 and 339 nm for **[2,1-*a*]DHIF**, **[2,1-*b*]DHIF** and **[1,2-*b*]DHIF** in accordance with an increase of the π-conjugation. For the three compounds the fluorescent quantum yield was reported around 0.6.

4.2. Impact of the positional isomerism on the electronic properties: the example of the five dispirofluorene-indenofluorene (DSF-IF) isomers

The IF cores display different geometries, which lead to very different and unusual electronic properties, which have been reported by our group since 2006. The five dispirofluorene-indenofluorene (DSF-IF) regioisomers (dihydroindenofluorenes substituted on the bridges by fluorenyl units, Fig. 11) have been the investigated compounds for this structure/properties relationship study. In these examples, two parameters drive the properties: the nature of the linkage (*ortho*, *meta*, *para*) and the position of the bridges (*syn*, *anti*). Synthesis of the five DSF-IF isomers and the main physicochemical properties, summarized in Table 8, will only be briefly summarized hereafter as they have been described in detail in previous publications[21,24,40,45] and in a dedicated account.[27]

The five positional isomers display different electrochemical behaviours, highlighting the impact of the positional isomerism on the electron transfers. Comparing first the isomers based on the *para*-terphenyl core, **[1,2-*b*]-DSF-IF** presents two oxidation waves with maxima at 1.47 and 1.87 V *vs.* SCE, whereas **[2,1-*a*]-DSF-IF** possesses three waves at 1.36, 1.69, and 1.99 V *vs.* SCE. For both isomers, the first monoelectronic oxidation wave has been assigned to the oxidation of the IF core. Compared with **[1,2-*b*]-DSF-IF**, two differences are noted for **[2,1-*a*]-DSF-IF:** (i) the first oxidation (1.36 V *vs.* SCE) is shifted toward less anodic potentials and (ii) an additional oxidation process is observed at 1.69 V *vs.* SCE. The shift between the first oxidation potentials of **[1,2-*b*]-DSF-IF** and **[2,1-*a*]-DSF-IF** is due to the specific arrangement of the two fluorenyl units. In fact, in **[2,1-*a*]-DSF-IF**, the central IF core is

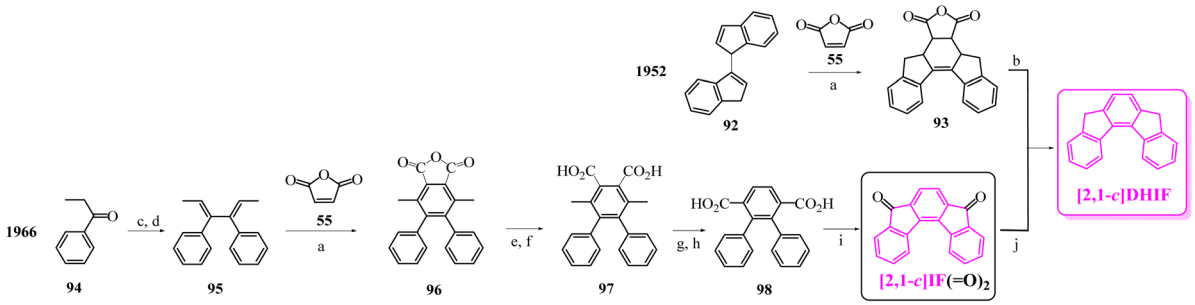

Scheme 23 Two routes to **[2,1-*c*]DHIF**[172] and **[2,1-*c*]IF(=O)$_2$**.[173] Access to **[2,1-*c*]DHIF** from **92**: (a) *p*-xylene, reflux, and (b) Cu powder, $Ba(OH)_2$, 400 °C. Access to **[2,1-*c*]DHIF** *via* **[2,1-*c*]IF(=O)$_2$** from **94**: (c) Al reduction, (d) H_2O, (a) *p*-xylene, reflux, (e) sulfur, 280 °C, (f) NaOH 0.1 M, 100 °C, (g) quinoline, $Cu_2Cr_2O_5$, Cu powder, 220 °C then HCl/H_2O, (h) pyridine/H_2O, $KMnO_4$, (i) concentrated H_2SO_4, 70–80 °C, and (j) KOH, diethylene glycol, H_2NNH_2, 180–190 °C.

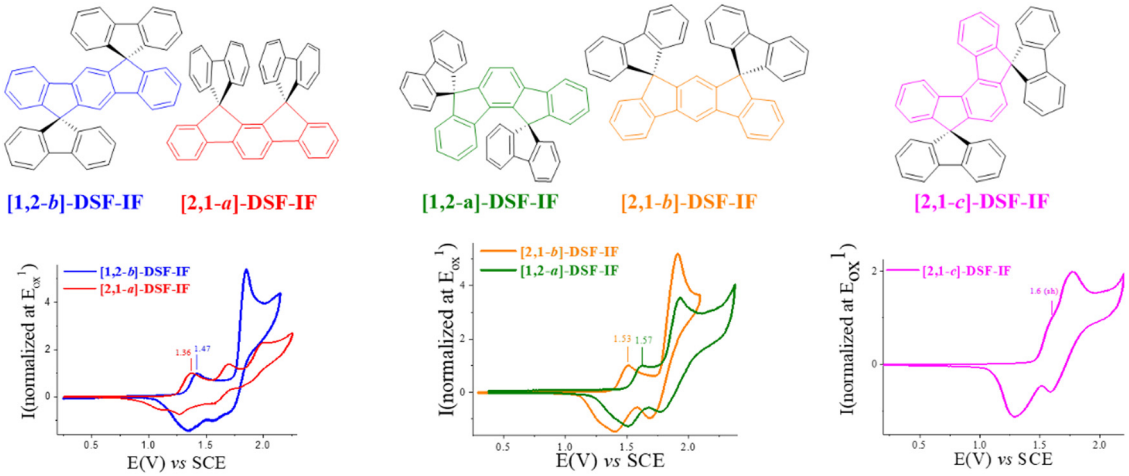

Fig. 11 Molecular structure of the five DSF-IF isomers and their respective cyclic voltammetries in oxidation.

subjected to a less important withdrawing effect of the cofacial fluorenyl units which are in strong interaction (*vs.* the two non-interacting fluorenyl units in **[1,2-*b*]-DSF-IF**). The additional oxidation detected at 1.69 V *vs.* SCE for **[2,1-*a*]-DSF-IF** was ascribed to the oxidation of this cofacial fluorene dimer. Thus, the different ring bridge arrangements of **[1,2-*b*]-DSF-IF** and **[2,1-*a*]-DSF-IF** and the different geometries induced lead to distinct electrochemical properties. As these two molecular systems are built on an identical *para*-terphenyl fragment this indicates that the linkage is not the only parameter implied in the electronic properties. Indeed, the *syn* arrangement significantly modified these properties by contracting the [1,2-*b*]-IF core.

[1,2-*a*]-DSF-IF and **[2,1-*b*]-DSF-IF** isomers provide a different example. Both compounds possess two oxidation waves at 1.57/1.88 V *vs.* SCE for **[1,2-*a*]-DSF-IF** and at 1.53/1.94 V *vs.* SCE for **[2,1-*b*]-DSF-IF**. The first monoelectronic oxidation has been assigned to the oxidation of the IF core, and the second multi-electronic wave to the concomitant oxidation of fluorenyl units and of the IF core radical cation. The shift of the first oxidation potential to more positive values from **[1,2-*b*]-DSF-IF**/**[2,1-*a*]-DSF-IF** to **[1,2-*a*]-DSF-IF**/**[2,1-*b*]-DSF-IF** has been assigned to a linkage effect (*para vs. meta* linkages). Linkage effects were particularly studied in the field of phosphorescent OLEDs to design high E_{T1} materials. Our group has notably investigated the differences induced by *ortho*, *meta* and *para* linkages on the parameters, which drive the OLEDs performances (ie: HOMO/LUMO energy levels, E_{S1}, E_{T1}, ...) for many different π-conjugated positional isomers.[42,44,177,178]

The slight shift in the first oxidation potential from **[2,1-*b*]-DSF-IF** to **[1,2-*a*]-DSF-IF**, despite their identical *meta* linkages, has been assigned to the contraction and deformation of the [1,2-*a*]DHIF core of **[1,2-*a*]-DSF-IF**, which induces poorer delocalization of the π electrons and hence a more anodic oxidation potential.

Finally, isomer **[2,1-*c*]-DSF-IF** displays a singular behaviour, its first oxidation being detected as a shoulder at 1.6 V. The *ortho*-terphenyl linkage of **[2,1-*c*]-DSF-IF** causes a deformation of the IF core, leading to an inversion of the HOMO and HOMO-1 compared with the other isomers.[24]

In conclusion, the linkages are strongly involved in the π-delocalization and therefore the electrochemical properties. However, the ring bridging is also of chief importance with two main consequences: (i) it changes the geometry (*syn vs. anti*) and can force the two cofacial fluorene moieties to interact such as in **[2,1-*a*]-DSF-IF** and (ii) it can increase the deformation of the IF core such as in **[2,1-*c*]-DSF-IF**.

The positional isomerism of the IF core also has important consequences on the optical properties. In THF, the five isomers display very similar low-energy absorption maxima between 338 and 344 nm (Fig. 12 and Table 8). **[1,2-*b*]-DSF-IF** and **[2,1-*a*]-DSF-IF** possess similar well-resolved absorption spectra, which is a characteristic of highly rigid structures. Compared to **[1,2-*b*]-DSF-IF**, the UV-vis spectrum of **[2,1-*a*]-DSF-IF** exhibits a slightly shifted main absorption band (344/339 nm for **[1,2-*b*]-DSF-IF**/**[2,1-*a*]-DSF-IF**). This blue shift has been assigned to a better delocalization of the π electrons in **[1,2-*b*]-DSF-IF** compared to **[2,1-*a*]-DSF-IF**. In contrast to the electrochemistry, **[1,2-*b*]-DSF-IF** and **[2,1-*a*]-DSF-IF** display similar behaviours in absorption spectroscopy, and the cofacial fluorenes of **[2,1-*a*]-DSF-IF** have only a limited influence on the electronic transitions. The spectrum of **[2,1-*b*]-DSF-IF** was also similar in shape but was red-shifted by 3 nm compared with the *para–syn* homologue **[2,1-*a*]-DSF-IF**. Hence, *para*-substituted compounds do not always present longer π-conjugated pathways *vs.* their *meta*-substituted analogues. This indicates that the linkages are not the only feature driving the electronic properties and that the bridging is also of key importance.

The specific absorption spectrum of **[1,2-*a*]-DSF-IF** highlights the role played by the ring bridging (structural deformation) in the transitions. Indeed, isomers **[1,2-*b*]-DSF-IF**, **[2,1-*a*]-DSF-IF** and **[2,1-*b*]-DSF-IF** all possess low energy absorption bands with high ε whereas very weak bands at 333 and 342 nm with low ε were displayed for the isomer **[1,2-*a*]-DSF-IF** (Fig. 12). Indeed, **[1,2-*a*]-DSF-IF** has no symmetry axis/plane, and its constrained structure leads to a deformation of

Table 8 Selected electronic properties of the five DSF-IF isomers[27]

	[1,2-*b*]-DSF-IF	[2,1-*a*]-DSF-IF	[1,2-*a*]-DSF-IF	[2,1-*b*]-DSF-IF	[2,1-*c*]-DSF-IF
T_d (°C)	355	—	330	359	—
E^{ox} (V)[a] *vs.* SCE	1.47, 1.87	1.36, 1.69, 1.99	1.57, 1.88	1.53, 1.94	1.6(sh), 1.77
HOMO[b] (eV)	−5.76	−5.64	−5.86	−5.80	−5.87
E^{red} (V) *vs.* SCE	−2.32[c]	−2.48[c]	−2.86[d]	−2.84[d]	−2.59[d]
LUMO[e] (eV)	−2.17	−2.03	−1.70	−1.75	−2.00
λ_{abs}[f] (nm)	298, 310, 328, 336, 344	296, 311, 323, 339	298, 308, 333, 342	298, 310, 326, 334, 342	298, 309, 317, 338
λ_{em}[f] (nm)	343, 358	345, 363, 381, 403	341, 354	346, 354, 363	344, 358
$\varnothing_{sol}$[fg]	0.62	0.60	0.23	0.54	0.50
E_T[h] (eV)	2.52	2.52	2.76	2.76	2.63

[a] In CH_2Cl_2 + Bu_4NPF_6 0.2 M. [b] From E^{ox}_{onset}. [c] In DMF + Bu_4NPF_6 0.1 M. [d] In THF + Bu_4NPF_6 0.1 M. [e] From E^{red}_{onset}. [f] In THF. [g] Quinine sulfate as the reference. [h] In methylcyclohexane/2-methylpentane.

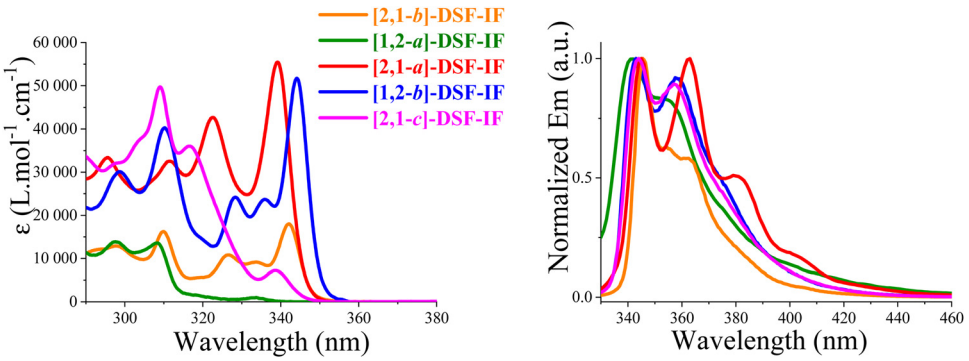

Fig. 12 Absorption (left) and emission (right) spectra of the five DSF-IF isomers in THF. Adapted with permission from ref. 27. Copyright 2023 American Chemical Society.

its **[1,2-*a*]**-central core, which modifies this first π–π* transition. **[2,1-*c*]-DSF-IF**, which also possesses a highly distorted IF backbone, displays an identical characteristic with a weak band at 338 nm.

With regard to the emission properties, **[1,2-*b*]-DSF-IF**, **[2,1-*a*]-DSF-IF** and **[2,1-*b*]-DSF-IF** possess well-resolved spectra with a very small Stokes shift. **[2,1-*a*]-DSF-IF** presents the most important Stokes shift, which has been related by theoretical calculations to structural modifications. Indeed, in the ground state **[2,1-*a*]-DSF-IF** shows a staggered conformation of the fluorenes, whereas in the first singlet excited state a cofacial eclipsed arrangement was detected.[21] Compared to the other isomers, **[1,2-*a*]-DSF-IF** was found to have the lowest quantum yield (0.23) and its emission decay occurred with two lifetimes instead of one. This unusual emission translates to unconventional processes, such as multiple emissive states or partially decoupled excited states and points to the impact of the regioisomerism on the photophysics.

The phosphorescence contribution was also very informative. The two *para*-isomers (**[1,2-*b*]-DSF-IF** and **[2,1-*a*]-DSF-IF**) and the two *meta*-isomers (**[1,2-*a*]-DSF-IF** and **[2,1-*b*]-DSF-IF**) possess almost identical phosphorescence contributions, indicating that the triplet state is driven by the linkages (*para* or *meta*) with a very limited influence of the ring bridging. The E_{T1} value were therefore identical for **[1,2-*b*]-DSF-IF** and **[2,1-*a*]-DSF-IF** (2.52 eV) and for **[1,2-*a*]-DSF-IF** and **[2,1-*b*]-DSF-IF** (2.76 eV). E_{T1} of the *ortho*-isomer **[2,1-*c*]-DSF-IF** was reported to be 2.63 eV. Thus, it has been shown that E_{T1} is only very weakly dependent on the bridging. This was an important result, which has driven further studies on this fragment. Thanks to an E_{T1} above 2.5 eV, all these materials have been incorporated as host materials in green and/or blue PhOLEDs (see below).

4.3. Uses of [1,2-*a*]-, [2,1-*b*]- or [2,1-*c*]DHIF-based organic semiconductors in OLED or PhOLEDs

Despite being largely less developed than the [1,2-*b*]DHIF- and [2,1-*a*]DHIF-based organic semiconductors described above in parts 2 and 3, the literature also reports some examples of electronic devices using [1,2-*a*]-, [2,1-*b*]- or [2,1-*c*]-IF-based organic semiconductors. First, **[1,2-*a*]-DSF-IF** and **[2,1-*b*]-DSF-IF** have been used as the EML in fluorescent multilayer OLED33-OLED34. OLED34 using **[2,1-*b*]-DSF-IF** as the EML displays higher performances than OLED33 with **[1,2-*a*]-DSF-IF** reaching a CE of 0.7 cd A^{-1}. Interestingly, both devices display a violet emission with CIE coordinates of (0.193, 0.128) for OLED33 and (0.201, 0.188) for OLED34.

[2,1-*b*]-83[76] (Scheme 24) is an isomer of **[1,2-*b*]-11** (Scheme 4) and has been used as a dopant in ML-OLED with host-guest EMLs (see OLED35-OLED37). With similar architectures to those used with **[1,2-*b*]-11** in OLED22-OLED24 (Table 1), OLED35-OLED37 with **[2,1-*b*]-83** doped in MADN as the EML were largely less efficient. In fact, EQE_{max} was reported close to 6% for OLEDs22–24 whereas EQE_{max} reached less than 1.5% for OLEDs35–37. The different IF core in **[2,1-*b*]-83** and **[1,2-*b*]-11**

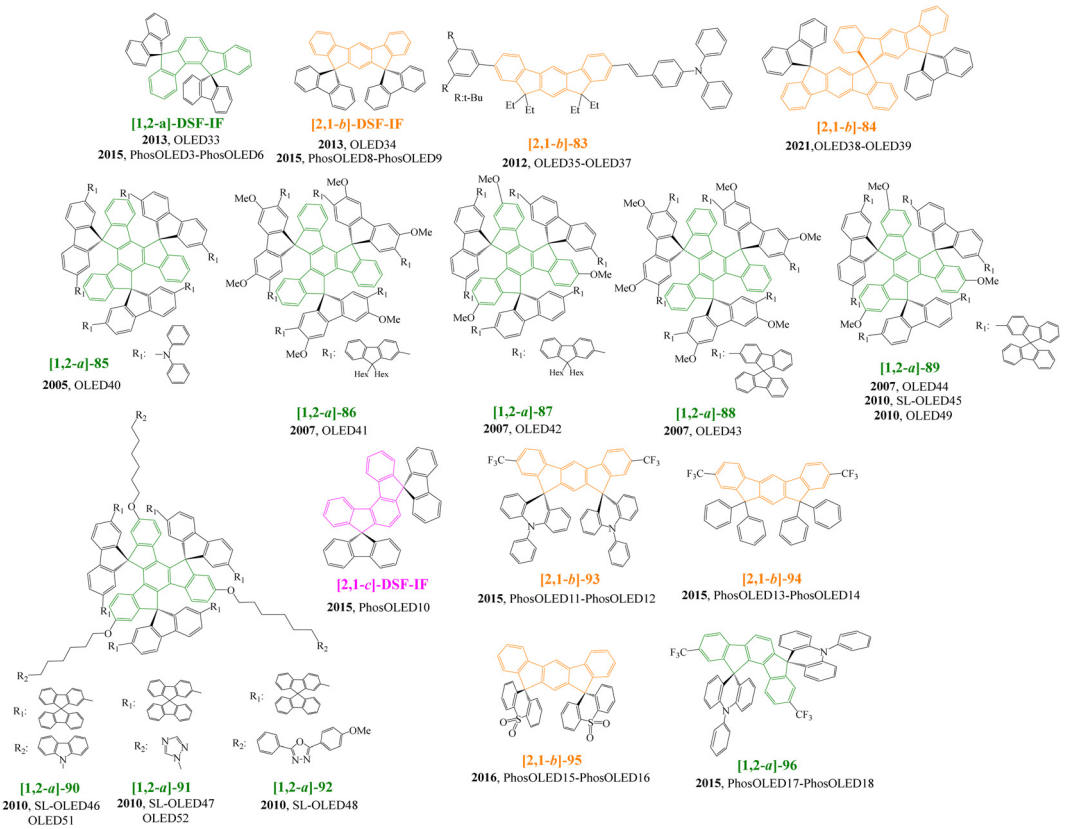

Scheme 24 Molecular structure of organic semiconductors based on **[2,1-*b*]**-, **[1,2-*a*]**- or **[2,1-*c*]**-indenofluorenyl cores used in OLED or PhOLEDs.

leads to a different gap for the two isomers[76] (2.93/2.85 eV for **[1,2-*b*]-83**/**[1,2-*b*]-11**). The shortest conjugation has an influence on the efficiency of the devices. The red shift of the emission of **[1,2-*b*]-11**/**[1,2-*b*]-83**, from 464 nm to 492 nm was also observed in the EL spectra of the devices, which were red-shifted from 453/455 nm for OLEDs22–24 (blue emission, CIE: 0.14; 0.2) to 507/508 nm for OLEDs35–37 (bluish-green emission, CIE: 0.22, 0.36).

[2,1-*b*]-84[179] is built on the linkage of two [2,1-*b*]DHIF units *via* a spiro bridge. This 3D rigid blue emitter was prepared from its dione parent.[180] The length of each [2,1-*b*]DHIF core, measured on the X-Ray structure, was 10.68/10.62 Å similar to that of **[2,1-*b*]-DSF-IF** (10.63 Å) and the distance of the spiro bridge in each [1,2-*b*]DHIF unit was 5.22/5.25 Å, slightly shorter than the one measured for **[2,1-*b*]-DSF-IF** (5.27 Å). TGA measurements show that **[2,1-*b*]-84** was highly thermally stable with a T_d of 450 °C, nearly 100 °C superior to that of **[2,1-*b*]-DSF-IF** (359 °C) which can be seen as "half" of this molecule. Also, except the thermal properties, all the other physicochemical properties (optical, electrochemical) were similar for the two compounds. **[2,1-*b*]-84** was used as the host for the yellow fluorescent emitter 4CzPNPh (3,4,5,6-tetrakis(3,6-diphenylcarbazol-9-yl)-1,2-dicyanobenzene) in a double EML OLED configuration: 4CzPNPh doped **[2,1-*b*]-84**/non-doped **[2,1-*b*]-84**. With the first 5% doping level for 4CzPNPh in **[2,1-*b*]-84**, OLED38 reaches very high performances CE(cd A^{-1})/PE(lm W^{-1})/EQE(%) of 32.5/15.3/11. Blue and yellow emission peaks were observed in the EL spectrum of OLED38 at 400 nm (blue emission of **[2,1-*b*]-84**) and at 550 nm (yellow emission of 4CzPNPh). The blue emission was however weak at a low voltage (4.7 V) and increases moderately with the voltage (up to 13.7 V). A second device was tested with a lower 4CzPNPh concentration, 0.5% in OLED39, and both blue and yellow emission were observed however the OLED performances were significantly lower (CE(cd A^{-1})/PE(lm W^{-1}) /EQE(%) of less than 18/10/7.5). In the EL spectrum of OLED39, the blue/yellow ratio emission was higher than in OLED38 (Table 9).

In 2005, Takagi's group[181] synthesized **[1,2-*a*]-85** based on a central planar truxene core,[184] which can be seen as an extended [1,2-*a*]DHIF core (Scheme 24). Three 2,7-diphenylaminofluorenes are spirolinked to the central truxene backbone. This compound was used as the HTL in a green fluorescent OLED using Alq3 as the emitter (OLED40). This OLED emits green light from Alq3 at V_{on} lower than 3 V and reaches luminance as high as 37 000 cd m^{-2} at 14 V. The lifetime of OLED40 was studied at a luminance of 200 cd m^{-2} and showed that the device could work for a thousand hours. Therefore, **[1,2-*a*]-85** appears to be a thermally durable HTL in combination with Alq3 in green fluorescent OLEDs.

In 2007, **[1,2-*a*]-86-87** and **[1,2-*a*]-88-89** all based on the **[1,2-*a*]**-IF-based truxene core were prepared and used as the blue emitting layer in ML-OLEDs.[182] These organic semiconductors were highly stable with T_d > 400 °C. Their UV-vis absorption emission spectra were rather similar and appear to be directed

Table 9 Performance of OLED devices with **[1,2-*a*]-** or **[2,1-*b*]**DHIF-based organic semiconductors

Device	Device architecture	V_{on} (V)	EQE[a] (%)	CE[a] (cd A^{-1})	PE[a] (lm W^{-1})	Luminance (cd m^{-2})	λ (EL spectrum) nm CIE(x, y)	Ref.
OLED33	ITO/CuPc/NPB/TCTA/**[1,2-*a*]-DSF-IF**/TPBI/LiF/Al	4.5	0.5	0.4	—	200[b]	390–400 nm (0.193, 0.128)	23
OLED34	ITO/CuPc/NPB/TCTA/**[2,1-*b*]-DSF-IF**/TPBI/LiF/Al	4.9	0.9	0.7	—	704[b]	390–400 nm (0.201, 0.188)	23
OLED35	ITO/DNTPD(60 nm)/NPB(30 nm)/**[2,1-*b*]-83** 3% in MADN (30 nm)/Alq3 (20 nm)/LiF(1 nm)/Al	4.0	0.91	2.21	1.59	7 394	507 (0.222, 0.376)	76
OLED36	ITO/DNTPD(60 nm)/NPB(30 nm)/**[2,1-*b*]-83** 5% in MADN (30 nm)/Alq3 (20 nm)/LiF(1 nm)/Al	3.5	0.89	1.99	1.18	9 490	508 (0.217, 0.362)	76
OLED37	ITO/DNTPD(60 nm)/NPB(30 nm)/**[2,1-*b*]-83** 7% in MADN (30 nm)/Alq3 (20 nm)/LiF(1 nm)/Al	3.5	1.37	3.68	3.71	9 114	507 (0.216, 0.355)	76
OLED38	ITO/MoO_3(6 nm)/NPB(70 nm)/mCP(5 nm)/**[2,1-*b*]-84**:4CzPNPh 5%(20 nm)/**[2,1-*b*]-76**(5 nm)/ TPBI(30 nm)/LiF(1 nm)/Al	—	11	32.5	15.3	—	—	179
OLED39	ITO/MoO_3(6 nm)/NPB(70 nm)/mCP(5 nm)/**[2,1-*b*]-84**:4CzPNPh 0.5%(20 nm)/**[2,1-*b*]-76**(5 nm)/ TPBI(30 nm)/LiF(1 nm)/Al	—	7.5	18	10	—	—	179
OLED40	ITO/**[1,2-*a*]-85**(60 nm)/Alq3(60 nm)/LiF(0.5 nm)/ Al(150 nm)	<3.0	—	3.4	—	37 000 (@14 V)	530 nm	181
OLED41	ITO/PEDOT/PVK/**[1,2-*a*]-86**/TPBI/Ba/Al	5.3	2.0	—	—	774 (@8.4 V)	432 nm 0.17, 0.08	182
OLED42	ITO/PEDOT/PVK/**[1,2-*a*]-87**/TPBI/Ba/Al	3.9	1.4	—	—	1717 (@7.4 V)	424 nm 0.17, 0.08	182
OLED43	ITO/PEDOT/PVK/**[1,2-*a*]-88**/TPBI/Ba/Al	5.8	2.9	—	—	480 (@7.8 V)	442 nm 0.16, 0.09	182
OLED44	ITO/PEDOT/PVK/**[1,2-*a*]-89**/TPBI/Ba/Al	5.0	2.4	—	—	997 (@6.7 V)	432 nm 0.17, 0.10	182
SL-OLED45	ITO/PEDOT(40 nm)/**[1,2-*a*]-89**(60 nm)/Ba(4 nm)/ Al(150 nm)	—	—	0.01	—	—	—	183
SL-OLED46	ITO/PEDOT(40 nm)/**[1,2-*a*]-90**(60 nm)/Ba(4 nm)/ Al(150 nm)	4.7	—	0.04	—	230	0.20, 0.21	183
SL-OLED47	ITO/PEDOT(40 nm)/**[1,2-*a*]-91**(60 nm)/Ba(4 nm)/ Al(150 nm)	5.2	—	0.10	—	150	0.17, 0.12	183
SL-OLED48	ITO/PEDOT(40 nm)/**[1,2-*a*]-92**(60 nm)/Ba(4 nm)/ Al(150 nm)	5.2	—	0.08	—	250	0.17, 0.11	183
OLED49	ITO/PEDOT(40 nm)/PVK(40 nm)/**[1,2-*a*]-87**(60 nm)/ Ba(4 nm)/Al (150 nm)	6.9	—	0.39	—	1980	0.17, 0.07	183
OLED50	ITO/PEDOT(40 nm)/PVK(40 nm)/**[1,2-*a*]-90**(60 nm)/ Ba(4 nm)/Al (150 nm)	6.9	—	0.43	—	1550	0.18, 0.10	183
OLED51	ITO/PEDOT(40 nm)/PVK(40 nm)/**[1,2-*a*]-91**(60 nm)/ Ba(4 nm)/Al (150 nm)	8.1	—	0.80	—	463	0.17, 0.08	183
OLED52	ITO/PEDOT(40 nm)/PVK(40 nm)/**[1,2-*a*]-92**(60 nm)/ Ba(4 nm)/Al (150 nm)	6.6	—	0.56	—	414	0.17, 0.07	183

[a] @10 mA cm^{-2}. [b] Maximum value.

by the more conjugated system (terfluorene) surrounding the central truxenyl unit. Indeed, their spectra are similar to those of other organic semiconductors possessing terfluorenyl driving systems as for example **[1,2-*b*]-72** (Fig. 10).[142] OLEDs41–44 based on these organic semiconductors exhibit blue light and color stability at different operating voltages. OLED43-OLED44 based on **[1,2-*a*]-88** and **[1,2-*a*]-89** with an EQE of 2.9/2.4% were slightly more efficient than OLED41-OLED42, based on **[1,2-*a*]-86** and **[1,2-*a*]-87** with an EQE of 2.0/1.4%. The presence of external spirobifluorene in **[1,2-*a*]-88-89** instead of dialkylfluorene in **[1,2-*a*]-86-87** may change the packing and therefore the charge transport in the materials.

Then, in 2010, three organic semiconductors based on a similar truxene central core possessing three flexible alkoxy chains (**[1,2-*a*]-90** to **[1,2-*a*]-92**[183]) have been designed. Electron-rich units (carbazole in **[1,2-*a*]-90**[183]) or electron-deficient moieties (1,2,4-triazole in **[1,2-*a*]-91**[183] or 2,5-diphenyl-1,3,4-oxadiazole in **[1,2-*a*]-92**[183]) were introduced on the flexible alkoxy chains (Scheme 24). The three organic semiconductors display similar optical properties to **[1,2-*a*]-89** mainly governed by the external highly conjugated SBF-fluorenyl-SBF arms. This indicates that the substitution of the central truxene by different electron-rich or electron-deficient units *via* non-conjugated alkoxy chains does not affect the main photophysical properties of **[1,2-*a*]-90** to **[1,2-*a*]-92**. The HOMO/LUMO levels of the three organic semiconductors were determined by cyclic voltammetry on solid films. The HOMO levels of **[1,2-*a*]-90**-**[1,2-*a*]-92** were similar (−5.6 eV), but their LUMO levels were different: −2.4/−2.7/−2.6 eV for **[1,2-*a*]-90**/**[1,2-*a*]-91**/**[1,2-*a*]-92** respectively. The authors ascribed the HOMO to the external highly conjugated SBF-fluorenyl-SBF arms whereas the LUMO was ascribed to the alkoxy-electron-deficient moieties.

SL-OLEDs with **[1,2-*a*]-90** to **[1,2-*a*]-92** as the EML (SL-OLEDs46–48) display higher performances than SL-OLED45 based on **[1,2-*a*]-89** showing that the introduction of the side chains on the truxenyl core has a positive effect on the performances. The performances remained however very low: 0.01 < CE < 0.1 cd A^{-1} for the four SL-OLED devices but higher device efficiencies (0.3 < CE < 0.8 cd A^{-1}) were reached introducing a thin layer (40 nm) of PVK (working as the HTL/EBL) between the anode and the EML (OLEDs49–52).

The potential of several [1,2-*a*]DHIF-, [2,1-*b*]DHIF- or [2,1-*c*]DHIF-based organic semiconductors have also been then tested as hosts for phosphorescent dopants (Table 10). First,

Table 10 Performance of devices using **[1,2-*a*]-DSF-IF**, **[2,1-*b*]-DSF-IF**, **[2,1-*c*]-DSF-IF** or **[1,2-*a*]-93** to **[2,1-*b*]-97** as hosts in phosphorescent OLEDs

Device	Device architecture	V_{on} (V)	EQE[b] (%)	CE[b] (cd A^{-1})	PE[b] (lm W^{-1})	Luminance (cd m^{-2})	CIE (x, y)	Ref.
PhosOLED3	ITO/CuPc(10 nm)/NPB(40 nm)/TCTA(10 nm)/**[1,2-*a*]-DSF-IF**:Ir(ppy)$_3$ 10% (20 nm)/TPBI(40 nm)/LiF(1.2 nm)/Al(100 nm)	2.8	14.8	57.3	30.3	31 500@240 mA cm^{-2}	0.30, 0.63	24
PhosOLED4	ITO/CuPc(10 nm)/NPB(40 nm)/TCTA(10 nm)/**[1,2-*a*]-DSF-IF**:FIrpic 25% (20 nm)/TPBI(40 nm nm)/LiF (1.2 nm) /Al(100 nm)	3.2	7.5	21.1	11.9	—	0.18, 0.45	24
PhosOLED5	ITO/CuPc(10 nm)/NPB(40 nm)/TCTA(10 nm)/**[1,2-*a*]-DSF-IF**:FIrpic 19% (20 nm)/TPBI(40 nm)/LiF (1.2 nm)/Al(100 nm)	3.2	6.1	16.7	8.9	—	0.18, 0.45	24
PhosOLED6	ITO/CuPc(10 nm)/NPB(40 nm)/TCTA(10 nm)/**[1,2-*a*]-DSF-IF**:FIrpic 20% (20 nm)/TPBI(40 nm)/ LiF(1.2 nm)/Al(100 nm)	4.0	5.7	15.4	8.5	4600@100 mA cm^{-2}	0.18, 0.44	25
PhosOLED8	ITO/CuPc(10 nm)/NPB(40 nm)/TCTA(10 nm)/**[2,1-*b*]-DSF-IF**:Ir(ppy)$_3$ 10% (20 nm)/TPBI(40 nm)/ LiF(1.2 nm)/Al(100 nm)	3.7	12.3[a]	49.6[a]	18.5[a]	30 000@220 mA cm^{-2}	0.32, 0.62	25
PhosOLED9	ITO/CuPc(10 nm)/NPB(40 nm)/TCTA(10 nm)/**[2,1-*b*]-DSF-IF**:FIrpic 20% (20 nm)/TPBI(40 nm)/ LiF(1.2 nm)/Al(100 nm)	3.9	5.3	14.7	8.4	3300@60 mA cm^{-2}	0.20, 0.44	25
PhosOLED10	ITO/CuPc(10 nm)/NPB(40 nm)/TCTA(10 nm)/**[2,1-*c*]-DSF-IF**:Ir(ppy)$_3$ 10% (20 nm)/TPBI(40 nm)/ LiF(1.2 nm)/Al(100 nm)	3.0	13.3	49.0	26.6	—	0.31, 0.63	24
PhosOLED11	ITO/CuPc(10 nm)/NPB(40 nm)/TCTA(10 nm)/**[2,1-*b*]-93**:Ir(ppy)$_3$ 10% (20 nm)/TPBI(40 nm)/LiF (1.2 nm)/Al(100 nm)	3.8	6.5	23.3	15	11 200@170 mA cm^{-2}	0.32, 0.62	25
PhosOLED12	ITO/CuPc(10 nm)/NPB(40 nm)/TCTA(10 nm)/**[2,1-*b*]-93**:FIrpic 20% (20 nm)/TPBI(40 nm)/LiF (1.2 nm)/Al(100 nm)	3.6	2.9	7.0	4.5	1 800@90 mA cm^{-2}	0.19, 0.41	25
PhosOLED13	ITO/CuPc(10 nm)/NPB(40 nm)/TCTA(10 nm)/**[2,1-*b*]-94**:Ir(ppy)$_3$ 10% (20 nm)/TPBI(40 nm)/LiF (1.2 nm)/Al(100 nm)	3.3	12.8	44.1	30.3	26 100@170 mA cm^{-2}	0.33, 0.62	25
PhosOLED14	ITO/CuPc(10 nm)/NPB(40 nm)/TCTA(10 nm)/**[2,1-*b*]-94**:FIrpic 20% (20 nm)/TPBI(40 nm)/LiF (1.2 nm)/Al(100 nm)	4.8	3.4	9.0	4.5	2500@70 mA cm^{-2}	0.19, 0.43	25
PhosOLED15	ITO/CuPc(10 nm)/NPB(40 nm)/TCTA(10 nm)/**[2,1-*b*]-95**:Ir(ppy)$_3$ 10% (20 nm)/TPBI(40 nm)/LiF(1.2 nm)/Al(100 nm)	3.2	13.8	52.2	33.5	—	0.33, 0.62	26
PhosOLED16	ITO/CuPc(10 nm)/NPB(40 nm)/TCTA(10 nm)/**[2,1-*b*]-95**:FIrpic 20% (20 nm)/TPBI(40 nm)/LiF(1.2 nm)/Al(100 nm)	3.9	4.8	15.2	8.4	—	0.20, 0.47	26
PhosOLED17	ITO/CuPc(10 nm nm)/NPB(40 nm)/TCTA(10 nm)/**[1,2-*a*]-96**:Ir(ppy)$_3$ 10% (20 nm)/TPBI(40 nm)/LiF (1.2 nm)/Al(100 nm)	3.9	15.9	55.7	33.3	32 250@140 mA cm^{-2}	0.30, 0.63	25
PhosOLED18	ITO/CuPc(10 nm)/NPB(40 nm)/TCTA(10 nm)/**[1,2-*a*]-97**:FIrpic 20% (20 nm)/TPBI(40 nm)/LiF (1.2 nm)/Al(100 nm)	3.9	7.9	19.6	10.9	6400@80 mA cm^{-2}	0.18, 0.42	25

[a] @10mA cm^{-2}. [b] Maximum value.

[1,2-*a*]-DSF-IF, **[2,1-*b*]-DSF-IF** and **[2,1-*c*]-DSF-IF** (Fig. 11) with an E_{T1} value of 2.76 eV for the two former and 2.63 eV for the latter were tested as the host for green PhOLEDs. **[1,2-*a*]-DSF-IF** as the host for green phosphorescent Ir(ppy)$_3$ has been tested in PhosOLED3 with a similar architecture to PhosOLED2 using **[1,2-*b*]-DSF-IF** as the host (Table 4). PhosOLED3 emits light at a low voltage of 2.8 V with a CE_{max} as high as 57.3 cd A^{-1}, a PE_{max} of 30.3 lm W^{-1} and an EQE_{max} of 14.8%. These performances were higher than that of PhosOLED2 (CE_{max}/PE_{max}/EQE_{max}: 31.4 cd A^{-1} /15.5 lm W^{-1} /9.9%) showing that the higher E_{T1} of **[1,2-*a*]-DSF-IF** may help in the efficiency of the device. With an E_{T1} of 2.76 eV, **[1,2-*a*]-DSF-IF** has also been used as the host for the sky-blue phosphor FIrpic, which E_{T1}: 2.64 eV allows the triplet exciton transfer from the host to the guest. With different doping levels (25% in PhosOLED4, 19% PhosOLED5 or 20% in PhosOLED6), the best performance was recorded for PhosOLED4 (CE_{max}/PE_{max}/EQE_{max}: 21.1 cd A^{-1} /11.9 lm W^{-1} /7.5% and V_{on}: 3.2 V). These results showed that despite an extended π-conjugated core, the E_{T1} can be kept sufficiently high in a [1,2-*a*]-indenofluorenyl core.

It must be noted, that in 2015, the performance of PhosOLED3 was the third most efficient green device using a pure hydrocarbon (PHC) host (top one: EQE: 17.3% with a trimer of Spirobifluorene as the host[185] and top two: EQE: 15.8% with **[1,2-*b*]-43**[117] (see PhOLED 1 in Table 4)). Since then, thanks to the optimization of the device architectures and to the design of new efficient PHC hosts, EQE_{max} now surpass 27% for the three colours.[186,187] These pioneering works on indenofluorenyl derivatives have significantly contributed to the development of PHC host materials in PhOLEDs, which is now a very promising approach.[116,186]

With an E_{T1} of 2.76 eV, **[2,1-*b*]-DSF-IF** was also adapted to host both green and blue phosphors. With an architecture similar to that used with both **[1,2-*b*]-DSF-IF** and **[1,2-*a*]-DSF-IF**, the green PhosOLED8 appears as efficient as PhosOLED3 indicating that the charge injection and the energy transfer from the host to guest are similar for the two isomers. However, the blue PhosOLED9 appears slightly less efficient than PhosOLED4 highlighting the difference between the isomers as a function of the phosphor used.

[2,1-*c*]-DSF-IF, with an E_{T1} of 2.63 eV has only been used to host Ir(ppy)$_3$ in PhosOLED10. Compared to PhosOLED2 and PhosOLED8, this device presents the lowest V_{on} (3.0 V) and the highest EQE_{max} (13.3%) showing the interest of using the [2,1-*c*]-DHIF core. PhOLED10 with **[2,1-*c*]-DSF-IF** as the host is however slightly less efficient than PhOLED3 with **[1,2-*a*]-DSF-IF** as the host with a larger V_{on} (3.0 *vs.* 2.8 V) and the lowest EQE (13.3 *vs.* 14.8%).

In order to increase the devices efficiency using host materials with a DHIF backbone, our group synthesized, in 2015, the donor–acceptor derivatives **[2,1-*b*]-93** and **[1,2-*a*]-96** (Scheme 24), in which each central IF core was, on one hand, substituted by two electron-acceptor groups CF_3 and on the other hand spiro-bridged to two donor moieties (phenylacridine).[25] The main idea behind this work was to improve the injection and transport of charges through the incorporation of donor and acceptor units keeping the E_{T1} controlled by the IF core. Indeed, the development of the Donor/Acceptor host has been an important step to reach high performance PhOLED, particularly single layer devices.[188] The oxidation of **[2,1-*b*]-93**, Fig. 13, involves first the oxidation of the phenylacridine units whereas its reduction involves the central electron-deficient IF core. Compared to **[2,1-*b*]-DSF-IF**, the oxidation and reduction both involve the IF core, the HOMO and LUMO of **[2,1-*b*]-93** were respectively higher and lower leading to a strong contraction of the electrochemical gap from **[2,1-*b*]-DSF-IF** (4.05 eV) to **[2,1-*b*]-93** (3.14 eV).

For the same reasons, the gap of **[1,2-*a*]-96** (3.10 eV) was more contracted than that of **[1,2-*a*]-DSF-IF** (4.06 eV). Looking at the phosphorescence spectra, the E_{T1} values were

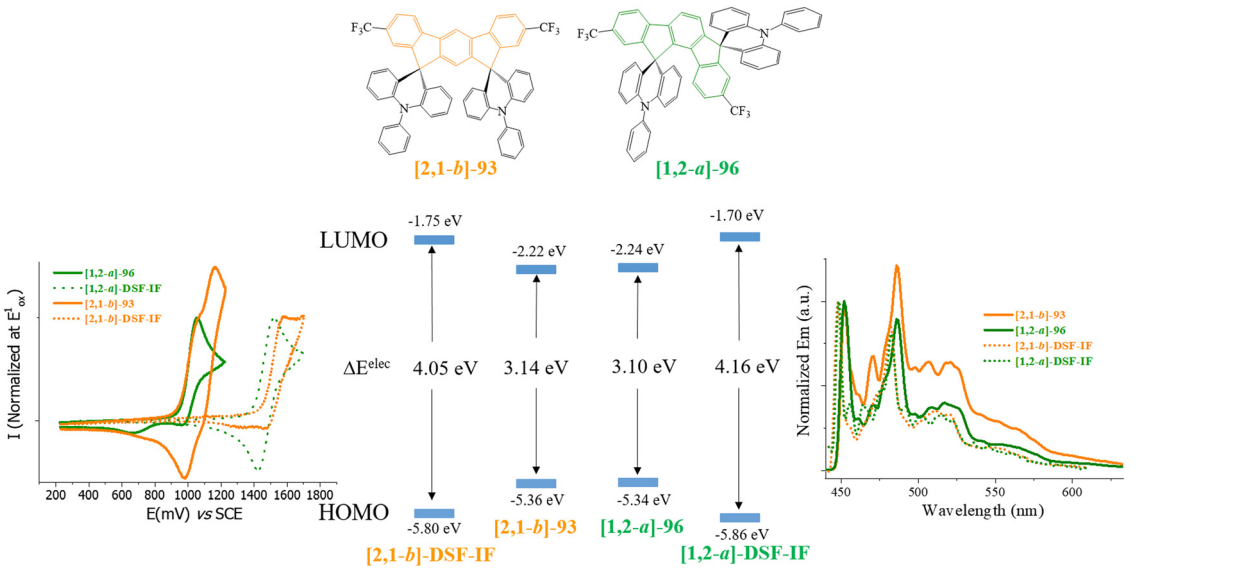

Fig. 13 Anodic oxidation (Left), phosphorescence spectra (Right) and electrochemical HOMO/LUMO levels of **[2,1-*b*]-93** (in orange) and **[1,2-*a*]-96** (in green) and of their related DSF-IF parents.

nevertheless similar (2.76/2.74 eV for **[2,1-*b*]-DSF-IF**/**[2,1-*b*]-93** and for **[1,2-*a*]-DSF-IF**/**[1,2-*a*]-96**) indicating that for both isomers, the incorporation of CF_3 groups and of phenylacridine (instead of fluorene) has only weak influence on the E_{T1} values (0.02 eV). This shows that the HOMO and LUMO energy levels can be controlled and tuned, maintaining the high E_{T1} of the IF core.

With such high E_T, **[2,1-*b*]-93**, **[2,1-*b*]-94** and **[1,2-*a*]-96** have been used as hosts for green ($Ir(ppy)_3$) and blue (FIrpic) phosphors. For both blue and green devices, the most efficient devices were those based on **[1,2-*a*]-96** as the host (green PhosOLED17 and blue PhosOLED18) followed by those based on **[2,1-*b*]-94** (green PhosOLED13 and blue PhosOLED14) and finally those based on **[2,1-*b*]-93** (green PhosOLED11 and blue PhosOLED12). Compared to the devices based on the non-substituted core **[1,2-*a*]-DSF-IF** or **[2,1-*b*]-DSF-IF**, the donor/acceptor design has a positive effect on the device performance for **[1,2-*a*]-96** but a negative effect for **[2,1-*b*]-93**. To unravel this intriguing feature, hole mobilities were measured using the SCLC technique for both **[2,1-*b*]-93** and **[1,2-*a*]-96** and the results showed that **[2,1-*b*]-93** possesses a modest μ_h of about 1.4×10^{-6} cm^2 V^{-1} s^{-1} whereas that of **[1,2-*a*]-96** was impressively enhanced and reaches about 1.5×10^{-4} cm^2 V^{-1} s^{-1}.[25] There are therefore two orders of magnitude difference in μ_h between the two hosts, which was the arguments made by the authors to explain the different performances.

It should also be mentioned that regioisomers **[2,1-*b*]-93** and **[1,2-*a*]-96** have also been successfully studied by ion mobility mass spectroscopy. As these isomers have been both synthesized in the same chemical reaction, this technique is particularly relevant to readily detect these isomers.[189]

Keeping the same molecular design strategy, *i.e.* modulation of the HOMO/LUMO levels without modifying the E_{T1} value, another organic semiconductor based on the [2,1-*b*]DHIF core has been designed by our group. In **[2,1-*b*]-95**,[26] the fluorenyl units, present in **[2,1-*b*]-DSF-IF**, have been changed in dioxothioxanthene (TXO_2) units (Scheme 24). The electron-withdrawing effect of the TXO_2 units deepened the HOMO level from −5.8 eV in **[2,1-*b*]-DSF-IF** to −6.04 eV in **[2,1-*b*]-95** and lowered the LUMO from −1.75 eV in **[2,1-*b*]-DSF-IF** to −2.06 eV in **[2,1-*b*]-95**. These two effects lead to a slight decrease of the gap from 4.05 eV for **[2,1-*b*]-DSF-IF** to 3.98 eV for **[2,1-*b*]-95**. The E_{T1} of **[2,1-*b*]-95**, 2.76 eV, was nevertheless kept similar to that of **[2,1-*b*]-DSF-IF** as imposed by the [2,1-*b*]-IF core. Therefore, **[2,1-*b*]-95** has been used as the host for green (PhosOLED15) and for blue phosphors (PhosOLED16). A comparison of the performances of these two devices to that using **[2,1-*b*]-DSF-IF** as the host (PhosOLED8-PhosOLED9) reveals, for the green PhosOLED15, a decrease of V_{on} (3.2 V) and an increase of the EQE_{max} showing the efficiency of the design strategy. Indeed, the HOMO/LUMO gap was decreased (and decreases in turn the V_{on} of the PhOLED) but the E_T, controlled by the [2,1-*b*]DHIF core, was kept high.

In conclusion, among the 18 PhOLEDs presented in this part (Table 4 and Table 10), **[1,2-*a*]-96** appears to be the most efficient matrix to host both the green (PhosOLED17) and blue phosphors (PhosOLED18). With its donor/acceptor design, **[1,2-*a*]-96** used as the host for green $Ir(ppy)_3$ and blue FIrpic PhOLEDs has led to an EQE of 15.9 and 7.9% respectively. Despite these performances being far from the best reported to date (EQE surpassing 30% for blue[190–194] or green[195–197] devices) these works have shown that the *meta*-substituted indenofluorenyl core can be used to design high E_T host materials. With further molecular design consideration, it is clear that these performances could be easily improved.

4.4. Uses of [2,1-*b*]DHIF-based organic semiconductors in TADF OLEDs

Thermally activated delayed fluorescence (TADF) emitters have demonstrated remarkable potential towards application in organic displays.[198] Owing to the efficient reverse intersystem crossing (RISC), TADF emitters could harvest non-emissive triplet excitons, which results in a 100% internal quantum efficiency (IQE). When employed as emitters, external quantum efficiencies (EQEs) of over 30% could be achieved.[199–201] Among others, spiroacridine is an important core which has been used to construct donor–acceptor type TADF emitters. For example, the acridine unit has been used to connect the two bridges of the [2,1-*b*]DHIF core to donor or acceptor units (**[2,1-*b*]-97** to **[2,1-*b*]-102**) leading to efficient TADF emitters and interesting TADF-OLED device performances. These OSCs are presented in Scheme 25 with some of their characteristics and the related TADF-OLED performances are summarized in Table 11.

In 2021, the group of Z. Wang and C. Yang synthesized a donor–acceptor derivative, **[2,1-*b*]-97**, in which the two units (^{t}Bu-Ph as the donor and triphenyltriazine as the acceptor) were linked through two acridine units themselves connected to a [2,1-*b*]-DHIF core. **[2,1-*b*]-97** was obtained from the dione **[2,1-*b*]IF(=O)$_2$** first converted in dispiroacridine-[2,1-*b*]-IF, itself substituted step by step by a *tert*-butylphenyl on one acridine and then by the triphenyltriazine unit on the second acridine. The [1,2-*b*]IF core was used to arrange the donor and acceptor in a face-to-face geometry forcing the acridine units to be perpendicular to the indenofluorenyl core. Calculations show that the LUMO is located on the electron-deficient triphenyltriazine unit linked to one acridine unit whereas the HOMO is spread on the other acridine unit connected to the *tert*-butylphenyl. The triazine unit weakens the electron-donating properties of its acridine. The calculated Natural Transition Orbital (NTO) indicates that S_1 and T_1 originate from the transition between this acridine and the triazine. The energies of S_1 and T_1 were calculated at 2.595 and 2.586 eV with a small ΔE_{ST} of 0.009 eV, which facilitate a fast triplet → singlet up-conversion. A local excited triplet state (^{3}LE) centred on the [2,1-*b*]-DHIF core is also observed with an energy of 2.658 eV facilitating an RISC process. Photophysical studies confirm the calculations with measurements of the singlet E_{S1} and triplet E_{T1} energy levels at 2.86 and 2.76 eV respectively, resulting in a short ΔE_{ST} of 0.1 eV (measured from the onset of fluorescence and phosphorescence at 77 K in the spectra). The PL quantum yield was measured at 98% in the solid state in a matrix of bis[2-(diphenylphosphino)phenyl ether oxide (DPEPO).

Scheme 25 Molecular structure of organic semiconductors based on [2,1-*b*]DHIF cores used in TADF OLEDs.

A transient PL decay spectrum confirms the TADF characteristic of **[2,1-*b*]-97** with two components of 28 ns and 2.1 μs which originate from prompt and delayed fluorescence respectively. All these properties were promising for the use of **[2,1-*b*]-97** as a TADF emitter in an OLED.

The first OLED based on a multi-layer architecture was fabricated (TADF-OLED1) with **[2,1-*b*]-97** doped in DPEPO in 20 wt% as the EML. This first TADF-OLED reached a very high EQE of 27.1%,[202] which was in 2021 among the best EQE reached for bluish-green doped TADF-OLEDs.[200,203–214] The same group studied then the influence of **[2,1-*b*]-97** concentration in DPEPO (from 10 to 70 wt%) on the performance of the devices (TADF-OLED2 to TADF-OLED6).[215] This study showed that EQE increases from 22.1 to 27.1% increasing the concentration from 10 to 20 wt% and then decreases up to 22.3% for a concentration of 70 wt%. The efficiencies of these devices were all significantly higher than that using a non-doped **[2,1-*b*]-97** EML (TADF-OLED7, EQE: 12.4%[215]) showing the interest of the DPEPO doping.

A second series of TADF emitters constructed on the [2,1-*b*]-DHIF core was synthesized in 2022 (**[2,1-*b*]-98**–**[2,1-*b*]-100**).[216] Compared to **[2,1-*b*]-97**, both **[2,1-*b*]-98** and **[2,1-*b*]-99** possess a carbazole donor unit (instead of a ^{t}Bu group), respectively in the *para* and *meta* position of the phenyl acridine core. In **[2,1-*b*]-100** one of the three phenyl units, decorating the triazine group in **[2,1-*b*]-98**, is changed in a cyclohexane unit. All these structural modifications influence the photophysical properties of **[2,1-*b*]-98**–**[2,1-*b*]-100** compared to **[2,1-*b*]-97**. The presence of the carbazole induced a weak blue shift of the absorption spectra from (400 nm) for **[2,1-*b*]-97** to (393/394/387 nm) for **[2,1-*b*]-98**/**[2,1-*b*]-99**/**[2,1-*b*]-100**. In emission, a red shift of 25 nm was measured from **[2,1-*b*]-97** (489 nm) to **[2,1-*b*]-98** and **[2,1-*b*]-99** (514 nm) whereas the red shift is only of 15 nm from **[2,1-*b*]-97** (489 nm) to **[2,1-*b*]-100** (504 nm). A weak increase of ΔE_{ST} (measured from the onset of fluorescence and phosphorescence at 77 K in the spectra) from 0.1 eV for **[2,1-*b*]-97** to (0.14/0.12/0.17 eV) for **[2,1-*b*]-98**/**[2,1-*b*]-99**/**[2,1-*b*]-100** is observed. For each emitter, **[2,1-*b*]-98**–**[2,1-*b*]-100**, TADF-OLEDs were constructed with the TADF emitter in 10, 20 or 30 wt% concentration in DPEPO. The most efficient OLED reaching an EQE of 26.3% was TADF-OLED15 with **[2,1-*b*]-100** 20 wt% in DPEPO as the EML. The two other TADF emitters led to less efficient devices (25.6% for TADF-OLED10 with **[2,1-*b*]-98** 30 wt% in DPEPO as the EML and 22.3% for TADF-OLED12 with **[2,1-*b*]-99** 20 wt% in DPEPO as the EML) despite these EQE remaining high. The highest performances of **[2,1-*b*]-97** *vs.* the three other TADF OSCs (**[2,1-*b*]-98** - **[2,1-*b*]-100**) may be correlated to its lower ΔE_{ST}. One should also note an extension of conjugation in those OSCs compared to **[2,1-*b*]-97**. This extension of conjugation leads to an increase of the ratio of prompt fluorescence in comparison with the delayed fluorescence (see the k_r and k_{RISC} values in Scheme 25) decreasing the TADF emission yield.

Based on these observations and in order to decrease the conjugation, the same group recently synthesized two new TADF emitters also constructed on the [2,1-*b*]-DHIF core with

Table 11 Performance of TADF-OLED devices with the **[2,1-*b*]**DHIF-based organic semiconductor

Device	Device architecture	V_{on} (V)	EQE[a] (%)	CE[a] (cd A^{-1})	PE[a] (lm W^{-1})	Luminance (cd m^{-2})	λ (EL spectrum) nm CIE (x, y)	Ref.
TADF-OLED1	ITO/MoO_3 (1 nm)/TAPC (40 nm)/TcTa (10 nm)/mCP (10 nm)/DPEPO:20 wt% **[2,1-*b*]-97** (25 nm)/DPEPO (5 nm)/Bphen (30 nm)/LiF (1 nm)/Al (1100 nm)	3.2	27.1	69.2	63.9	14 752	490 0.20, 0.45	202
TADF-OLED2	ITO/MoO_3 (1 nm)/TAPC (40 nm)/TcTa (10 nm nm)/mCP (10 nm)/DPEPO: 10 wt% **[2,1-*b*]-97** (25 nm)/DPEPO (5 nm)/Bphen (30 nm)/LiF (1 nm)/Al (1100 nm)	4.0	22.7	52.6	33	3222	— 0.189, 0.402	215
TADF-OLED3	ITO/MoO_3 (1 nm)/TAPC (40 nm)/TcTa (10 nm)/mCP (10 nm)/DPEPO: 20 wt% **[2,1-*b*]-97** (25 nm)/DPEPO (5 nm)/Bphen (30 nm)/LiF (1 nm)/Al (1100 nm)	3.4	27.1	69.1	63.9	10 130	— 0.199, 0.448	215
TADF-OLED4	ITO/MoO_3 (1 nm)/TAPC (40 nm)/TcTa (10 nm)/mCP (10 nm)/DPEPO: 30 wt% **[2,1-*b*]-97** (25 nm)/DPEPO (5 nm)/Bphen (30 nm)/LiF (1 nm)/Al (1100 nm)	3.2	24.5	64.9	54.0	14 752	— 0.208, 0.473	215
TADF-OLED5	ITO/MoO_3 (1 nm)/TAPC (40 nm)/TcTa (10 nm)/mCP (10 nm)/DPEPO: 40 wt% **[2,1-*b*]-97** (25 nm)/DPEPO (5 nm)/Bphen (30 nm)/LiF (1 nm)/Al (1100 nm)	3.2	24.5	66.5	65.2	18 153	— 0.211, 0.488	215
TADF-OLED6	ITO/MoO_3 (1 nm)/TAPC (40 nm)/TcTa (10 nm)/mCP (10 nm)/DPEPO: 70 wt% **[2,1-*b*]-97** (25 nm)/DPEPO (5 nm)/Bphen (30 nm)/LiF (1 nm)/Al (1100 nm)	3.2	22.3	60.1	55.5	18 289	— 0.213, 0.492	215
TADF-OLED7	ITO/MoO_3 (1 nm)/TAPC (40 nm)/TcTa (10 nm)/mCP (10 nm)/**[2,1-*b*]-97** (25 nm)/DPEPO (5 nm)/Bphen (30 nm)/LiF (1 nm)/Al (1100 nm)	3.0	12.4	31.7	32.4	8064	— 0.197, 0.443	215
TADF-OLED8	ITO/MoO_3 (1 nm)/TAPC (40 nm)/TcTa (10 nm)/mCP (10 nm)/DPEPO: 10 wt% **[2,1-*b*]-98** (25 nm)/DPEPO (5 nm)/Bphen (30 nm)/LiF (1 nm)/Al (1100 nm)	3.8	20.4	45.9	34.2	2296	488 0.183, 0.384	216
TADF-OLED9	ITO/MoO_3 (1 nm)/TAPC (40 nm)/TcTa (10 nm)/mCP (10 nm)/DPEPO: 20 wt% **[2,1-*b*]-98** (25 nm)/DPEPO (5 nm)/Bphen (30 nm)/LiF (1 nm)/Al (1100 nm)	3.4	22.0	54.5	42.5	6183	492 0.192, 0.425	216
TADF-OLED10	ITO/MoO_3 (1 nm)/TAPC (40 nm)/TcTa (10 nm)/mCP (10 nm)/DPEPO: 30 wt% **[2,1-*b*]-98** (25 nm)/DPEPO (5 nm)/Bphen (30 nm)/LiF (1 nm)/Al (1100 nm)	3.4	25.6	66.6	61.6	10 849	496 0.200, 0.454	216
TADF-OLED11	ITO/MoO_3 (1 nm)/TAPC (40 nm)/TcTa (10 nm)/mCP (10 nm)/DPEPO: 10 wt% **[2,1-*b*]-99** (25 nm)/DPEPO (5 nm)/Bphen (30 nm)/LiF (1 nm)/Al (1100 nm)	4.0	18.6	42.9	30.9	2174	490 0.186, 0.388	216
TADF-OLED12	ITO/MoO_3 (1 nm)/TAPC (40 nm)/TcTa (10 nm)/mCP (10 nm)/DPEPO: 20 wt% **[2,1-*b*]-99** (25 nm)/DPEPO (5 nm)/Bphen (30 nm)/LiF (1 nm)/Al (1100 nm)	3.4	22.3	55.6	50.5	6159	492 0.197, 0.431	216
TADF-OLED13	ITO/MoO_3 (1 nm)/TAPC (40 nm)/TcTa (10 nm)/mCP (10 nm)/DPEPO: 30 wt% **[2,1-*b*]-99** (25 nm)/DPEPO (5 nm)/Bphen (30 nm)/LiF (1 nm)/Al (1100 nm)	3.4	21.4	53.9	47	7447	492 0.201, 0.445	216
TADF-OLED14	ITO/MoO_3 (1 nm)/TAPC (40 nm)/TcTa (10 nm)/mCP (10 nm)/DPEPO: 10 wt% **[2,1-*b*]-100** (25 nm)/DPEPO (5 nm)/Bphen (30 nm)/LiF (1 nm)/Al (1100 nm)	4.0	22.2	43.5	32.6	1093	478 0.171, 0.321	216
TADF-OLED15	ITO/MoO_3 (1 nm)/TAPC (40 nm)/TcTa (10 nm)/mCP (10 nm)/DPEPO: 20 wt% **[2,1-*b*]-100** (25 nm)/DPEPO (5 nm)/Bphen (30 nm)/LiF (1 nm)/Al (1100 nm)	3.4	26.3	55.3	51.5	2775	484 0.173, 0.347	216
TADF-OLED16	ITO/MoO_3 (1 nm)/TAPC (40 nm)/TcTa (10 nm)/mCP (10 nm)/DPEPO: 30 wt% **[2,1-*b*]-100** (25 nm)/DPEPO (5 nm)/Bphen (30 nm)/LiF (1 nm)/Al (1100 nm)	3.4	23.6	52.2	46.6	3950	488 0.180, 0.375	216
TADF-OLED17	ITO/MoO_3 (1 nm)/TAPC (40 nm)/TcTa (10 nm)/mCP (10 nm)/DPEPO: 10 wt% **[2,1-*b*]-101** (25 nm)/DPEPO (5 nm)/Bphen (30 nm)/LiF (1 nm)/Al (1100 nm)	3.6	32.6	95	—	42 055	—	217
TADF-OLED18	ITO/MoO_3 (1 nm)/TAPC (40 nm)/TcTa (10 nm)/mCP (10 nm)/DPEPO: 20 wt% **[2,1-*b*]-101** (25 nm)/DPEPO (5 nm)/Bphen (30 nm)/LiF (1 nm)/Al (1100 nm)	3.2	35.6	108.6	—	76 964	—	217
TADF-OLED19	ITO/MoO_3 (1 nm)/TAPC (40 nm)/TcTa (10 nm)/mCP (10 nm)/DPEPO: 10 wt% **[2,1-*b*]-102** (25 nm)/DPEPO (5 nm)/Bphen (30 nm)/LiF (1 nm)/Al (1100 nm)	3.6	35.8	105.5	—	51 590	—	217
TADF-OLED20	ITO/MoO_3 (1 nm)/TAPC (40 nm)/TcTa (10 nm)/mCP (10 nm)/DPEPO: 20 wt% **[2,1-*b*]-102** (25 nm)/DPEPO (5 nm)/Bphen (30 nm)/LiF (1 nm)/Al (1100 nm)	3.2	36.1	111.6	—	105 907	—	217
TADF-OLED21	ITO/HATCN (5 nm)/TAPC (30 nm)/TcTa (15 nm)/mCBP (10 nm)/PPF: 10 wt% **[2,1-*b*]-103** (25 nm)/PPF (10 nm)/ANT-BIZ (30 nm)/LiF (1 nm)/Al (1100 nm)	3.6	25.3	70.4	—	22 400	—	218
TADF-OLED22	ITO/HATCN (5 nm)/TAPC (30 nm)/TcTa (15 nm)/mCBP (10 nm)/PPF: 20 wt% **[2,1-*b*]-103** (25 nm)/PPF (10 nm)/ANT-BIZ (30 nm)/LiF (1 nm)/Al (1100 nm)	3.2	34.2	104.8	—	69 357	—	218

ANT-BIZ: 1-(4-(10-([1,1′-biphenyl]4-yl)anthracene-9-yl)phenyl)-2ethyl-1*H*-benzo[d]imidazole.

however only one acridine unit between this core and the acceptor unit (triphenyltriazine) and either a fluorene (in **[2,1-*b*]-101**) or two methyl units (in **[2,1-*b*]-102**) decorating the second bridge of the [2,1-*b*]-DHIF core.[217] Both OSCs were doped in DPEPO as the EML in TADF-OLEDs. The EQEs surpassed those previously reached and the four devices are in the top 10 of the more efficient bluish green TADF-OLEDs,[200,201,210] especially TADF-OLED20 using **[2,1-*b*]-102** as the dopant which reaches an extremely high EQE of 36.1%. Those results show that a well-thought-out structural modification may offer fine control of the photophysical properties which is useful to optimize the TADF emitters and the device performances. As revealed in Scheme 25, the new OSCs possess a lower ΔE_{ST} value and k_r and k_{RISC} values similar to the one of **[2,1-*b*]-97**. The structural modifications from **[2,1-*b*]-97** to **[2,1-*b*]-98** (increase conjugation and decrease electron-donating properties) or from **[2,1-*b*]-97**-**[2,1-*b*]-98** to **[2,1-*b*]-101**-**[2,1-*b*]-102** (decrease conjugation) or finally from **[2,1-*b*]-101**-**[2,1-*b*]-102** (enhance electron-donating properties) have allowed the authors to construct TADF-OLED20 which reaches excellent performances.

Finally, **[2,1-*b*]-103** with a 4π-3spiro architecture (four π-systems connected thanks to 3 spiro-bridges) was very recently designed and tested in TADF-OLED21–22 also with interesting performances.[218] As expected, the HOMO and HOMO-1 are spread on the two acridine units and the LUMO on the triphenyltriazine substituent. For this emitter ΔE_{ST} is 0.02 eV, the decay profile exhibits two components corresponding to prompt (27 ns) and delayed fluorescence (3.2 μs) and the rate constant of radiative decay and reverse intersystem crossing are similar to those of **[2,1-*b*]-101**-**[2,1-*b*]-102** (Scheme 25) suggesting efficient device performances. In fact, TADF-OLED22 with **[2,1-*b*]-103** (10 wt% doped in dibenzo[*b*,*d*]furan-2,8-diylbis(diphenylphosphine oxide) (PPF)) as the EML reaches an EQE of 34.2%. Due to the difference in host materials (PPF in TADF-OLED21 and 22 or DPPO in the other TADF-OLEDs, the comparison is not simple, however all these results show the interest of the [2,1-*b*]-DHIF core to construct efficient TADF bluish-green emitters.

4.5. Uses of [1,2-*a*]- or [2,1-*b*]DHIF-based organic semiconductors in OFET, OPV, DSSC, *etc.*

Chemical modification of the bridges and/or of the DHIF core has allowed us to drastically tune the electronic properties of the resulting organic semiconductors and this strategy has highlighted the potential of the DHIF-based organic semiconductors in other OE devices. This is what we aim to describe in this last part. As presented above in section 3 (Scheme 22), access to **[2,1-*b*]IF(=O)$_2$** dates from 1951,[168] however its physicochemical properties were only reported in 2015 with those of its parents compounds **[2,1-*b*]-104**, **[2,1-*b*]-105** (Scheme 26) and **[2,1-*b*]DHIF**.[170] Electrochemical data showed that, due to the presence of strong electron-deficient groups (carbonyl or dicyanovinylene), **[2,1-*b*]IF(=O)$_2$** (−5.96 eV), **[2,1-*b*]-104** (−5.90 eV) and **[2,1-*b*]-105** (−5.91 eV) possessed HOMO levels deeper than that of **[2,1-*b*]DHIF** (−5.71 eV). Their LUMO levels recorded between −3.52 eV for **[2,1-*b*]IF(=O)$_2$** and −3.93 eV for **[2,1-*b*]-104** were strongly deepened compared to that of **[2,1-*b*]DHIF** (−2.04 eV). Despite the presence of two dicyanovinylene groups in **[2,1-*b*]-105**, its LUMO level was surprisingly higher than that of **[2,1-*b*]-104** with only one dicyanovinylene (−3.81 eV *vs.* −3.93 eV). This unexpected behaviour has been assigned to the deformation of the [2,1-*b*]DHIF core induced by steric hindrance or to electronic repulsion between the adjacent cyano groups.[170]

The potential of the three electron-deficient organic semiconductors as active layers of n-channel OFETs was estimated with bottom-gate bottom-contact OFETs. As noticed above for **[1,2-*b*]IF(=O)$_2$**[86] in OFET 3 (Table 3), no field-effect was observed for OFET64 (Table 12) using **[2,1-*b*]IF(=O)$_2$**.[170] The introduction of one CN group in **[2,1-*b*]-104** has allowed us to measure in OFET65 a modest μ_e of 4.6×10^{-6} cm^2 V^{-1} s^{-1}, with a threshold voltage (V_T) of 18.4 V, a subthreshold slope (SS) of

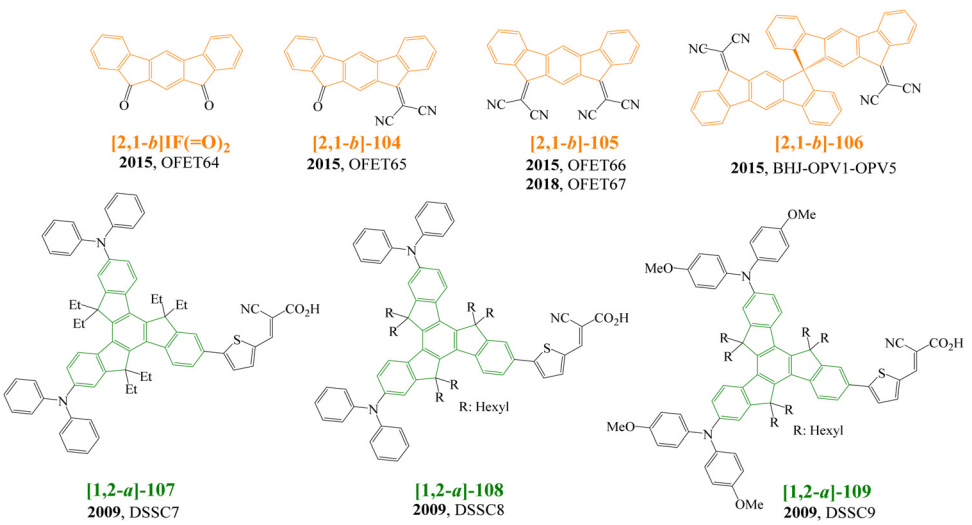

Scheme 26 Molecular structure of the organic semiconductors based on **[2,1-*b*]DHIF** or **[1,2-*a*]DHIF** cores used in OFETs, OSCs or DSSCs.

Table 12 Performance of devices (OFETs, BHJ-OPVs, and DSSCs) using different **[2,1-*b*]**-DHIF- or **[1,2-*a*]**-DHIF-based organic semiconductors

OFETs

Device	Device architecture	μ_{FET} ($cm^2\ V^{-1}\ s^{-1}$)	V_T (V)	SS ($V\ dec^{-1}$)	I_{on}/I_{off}	Ref.
OFET64	Bottom-gate bottom-contact structure **[2,1-*b*]IF(=O)$_2$**	No-gate effect				170
OFET65	Bottom-gate bottom-contact structure **[2,1-*b*]-104**	4.6×10^{-6}	18.4	5.74	10^3–10^4	170
OFET66	Bottom-gate bottom-contact structure **[2,1-*b*]-105**	1.02×10^{-3}	7.2	2.16	6.3×10^5	170
OFET67	Bottom-gate/bottom-contact device in a glove box under ambient nitrogen Al/SU-8/Au/**[1,2-*b*]-105**	μ_{FET} linear: 0.0009 $cm^2\ V^{-1}\ s^{-1}$	20	2.3	8×10^4	99
		μ_{FET} saturation: 0.002 $cm^2\ V^{-1}\ s^{-1}$	17	3.2	7×10^4	

BHJ OPVs

Device	Device architecture	V_{oc} (V)	J_{SC} ($mA\ cm^{-2}$)	FF	PCE(%)	Ref.
BHJ-OPV1 prepared in TCE	ITO/PEDOT:PSS/PTB7:**[2,1-*b*]-106**(1:2)/ Ca/Al	0.87	1.13	0.49	0.64	180
BHJ-OPV2 prepared in TCE	ITO/PEDOT:PSS/PTB7:**[2,1-*b*]-106**(1:1)/ Ca/Al	0.89	1.41	0.48	0.80	180
BHJ-OPV3 prepared in TCE/DCB	ITO/PEDOT:PSS/PTB7:**[2,1-*b*]-106** (1:1)/ Ca/Al	0.89	0.22	0.19	0.05	180
BHJ-OPV4 prepared in DCB	ITO/PEDOT:PSS/PTB7:**[2,1-*b*]-106** (1:1)/ Ca/Al	0.09	0.10	0.09	0.01	180
BHJ-OPV5 prepared in TCE/3%DIO	ITO/PEDOT:PSS/PTB7:**[2,1-*b*]-106** (1:1)/ Ca/Al	0.42	0.03	0.20	0.00	180

Dye-sensitized solar cells

Device	Device architecture	V_{oc} (V)	J_{SC} ($mA\ cm^{-2}$)	FF	PCE (%)	Ref.
DSSC7	FTO/TiO_2/**[1,2-*a*]-107**/Platinized FTO	0.689	7.75	0.73	3.90	220
DSSC8	FTO/TiO_2/**[1,2-*a*]-108**/Platinized FTO	0.731	7.89	0.74	4.27	220
DSSC9	FTO/TiO_2/**[1,2-*a*]-109**/Platinized FTO	0.752	6.86	0.70	3.61	220

DIO: 1,8-diiodooctane

5.74 V dec^{-1} and a I_{on}/I_{off} of 10^3–10^4. Although low, the performance of OFET65 highlighted the effect of the integration of one dicyanovinylene unit on the [2,1-*b*]DHIF core. OFET66 based on **[2,1-*b*]-105** has allowed us to reach higher values with μ_e of 1.02×10^{-3} $cm^2\ V^{-1}\ s^{-1}$, V_T of 7.2 V, SS of 2.16 V dec^{-1} and a I_{on}/I_{off} of 6.3×10^5. Thus, incorporation of CN units instead of oxygen atoms has allowed us to consistently increase the electron mobility and other OFET parameters.

Electrical stability of OFET66 has been studied using a gate bias stress and it was shown that (i) the instability of the OFETs was only linked to charges trapped in the insulator and not in the **[2,1-*b*]-105** active layer, and (ii) the SS related to defects in the interface between **[2,1-*b*]-105** and the insulating layer was almost constant under gate bias stress indicating that no defect state was created at this interface. This study provided an interesting finding about the origin of the instability in OFETs using the active layer of DHIF. As the μ_e of **[2,1-*b*]-105** was constant under applied stress, the electrical stability of OFET66 was then promising for its integration in a circuit. Pseudo CMOS inverters with **[2,1-*b*]-105**-based OFETs have been successfully fabricated and characterized.[170]

Performance improvements of OFETs based on **[2,1-*b*]-105** have been then evaluated by optimization of the fabrication process.[219] The μ_e was improved reaching 2.2×10^{-3} $cm^2\ V^{-1}\ s^{-1}$. The μ_{FET} improvement after post-annealing treatment can be attributed to some reasons: (i) eliminated vacancies and/or lattice defects in **[2,1-*b*]-105**, (ii) structural arrangement of **[2,1-*b*]-105** film and (iii) better matching at the SU-8/**[2,1-*b*]-105** interface resulting in higher mobility. The annealing effect on the electrical properties of **[2,1-*b*]-105** was more precisely studied by characterizing the devices at different temperatures from 300 to 380 K, allowing us to evaluate the activation energy of the mobility (E_a) and the density of states DOS.[100] After annealing treatment, a reduction of E_a was observed. Defects at the electrodes/organic semiconductor interface, accelerating the charge injection in the active layer, have been involved in this decrease. A reduction in the width of the band tail of the calculated DOS was also observed which could be linked to the increase ordering of **[2,1-*b*]-105** molecules after annealing treatment. In order to understand the charge transport phenomena in the **[2,1-*b*]-105** layer, the temperature dependence mobility and the current characteristics (U–V) were modeled using the VRH model. Good coherence between experimental and theoretical results was obtained, showing the validity of the VRH model to represent the charge conduction in the **[2,1-*b*]-98** layer.

[2,1-*b*]-105 was also tested in OFET67[99] built in similar conditions than OFET61 based on **[1,2-*b*]-40** (Table 3). As shown in Table 12, μ_e extracted from OFET67 was one order of magnitude lower than that from OFET61. This shows that switching from the *syn* geometry found in **[2,1-*b*]-105** to the *anti* geometry in **[1,2-*b*]-40** coupled to the addition of pentyl side chains have beneficial effects on both μ_{FET} (2×10^{-3} *vs.* 2.1×10^{-2} $cm^2\ V^{-1}\ s^{-1}$), I_{on}/I_{off} ratio (7×10^4 *vs.* 5×10^5) and SS (3.2 *vs.* 1.9 V dec^{-1}) without a negative consequence on V_{TH} (17 *vs.* 20 V).[99] This shows the key role played by isomerism in the design of organic semiconductors. However, despite better electrical parameters, **[1,2-*b*]-40** leads to less stable OFETs than **[2,1-*b*]-105** showing that the most efficient device is not always

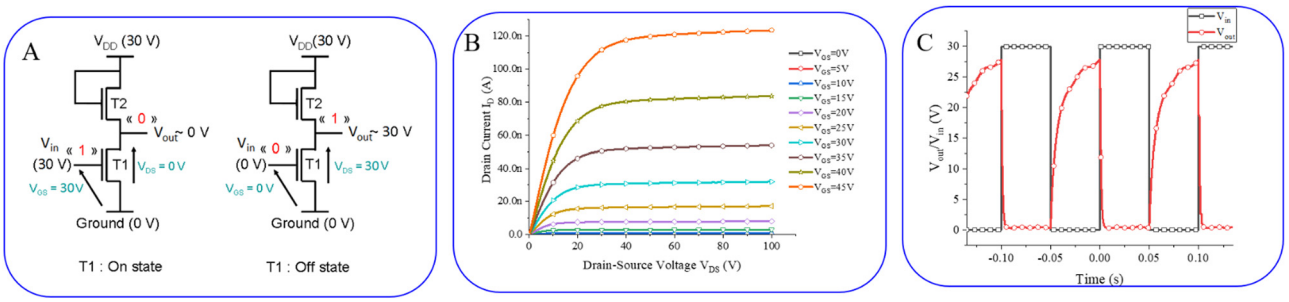

Fig. 14 (A) Schematic of the pseudo CMOS inverter and (B) T1 associated output characteristics, (C) inverter made of n-type OFETs with *W*/*L* = 1000/2 and 250/20 for the active charge. Adapted from ref. 170 with permission from the Royal Society of Chemistry.

the most stable one. This is an important consideration for real electronic applications. Comparing OFET61 and OFET67, it has been highlighted that the V_{TH} shift of the OFETs has a different origin. At low gate bias stress, the carrier trapping inside the insulator is at the origin of the instability of OFET61. Oppositely, in OFET67, both the carrier trapping in the insulator and the defect density formation in the active layer are responsible for the instability. At high bias stress, the authors proposed a different situation. This time, only the carrier trapping in the insulator layer is implied for both **[1,2-*b*]-40** and **[2,1-*b*]-105**-based OFETs. In this work the authors have also shown that, under the same gate bias stress, the **[1,2-*b*]-40**-based OFET displays a larger V_{TH} shift than the **[2,1-*b*]-105**-based OFET, which was assigned to a higher gate leakage current in the former. This feature was related to the different insulator/organic semiconductor interfaces. Thus, in this work, it was shown that minor structural modifications of the molecular structure of the organic semiconductor (**[1,2-*b*]-40** *vs.* **[2,1-*b*]-105**) can induce electrical instabilities of the corresponding OFET (OFET61 *vs.* OFET67) arising from different features showing the importance of the DHIF core.

Pseudo CMOS inverters made of n-type **[2,1-*b*]-105**-based OFETs have been also constructed (Fig. 14A) and characterized (Fig. 14C).[170] Generally, the response efficiency of the logic gate as the inverter is related to on/off states of p type and n type OFETs. The on/off states are defined by the R_{DSon} and R_{DSoff} ratios corresponding to the (I_{DS}, V_{DS}) slope. These studies were performed with n-type OFETs. In a circuit, there is a switch of the OFETs from the saturated to the linear regime. This switch is a very important parameter and is directly connected to the difference between linear R_{DS} (R_{DSon}) and saturated R_{DS} (R_{DSoff}). The R_{DSon}/R_{DSoff} ratio was evaluated in this work at 1.5×10^3. This value is significantly high to discriminate well between the off and the on state.

Pseudo CMOS inverters were fabricated and characterized with a 10 Hz square signal applied as the input voltage (V_{in}). The output voltage V_{out} followed a classical inverter behaviour with a high value of about 27.5 V when V_{in} = 0 V and a low value of about 0.5 V when V_{in} = 30 V (Fig. 14C). In addition, for a V_{DD} of 30 V, the V_{out} was measured at *ca.* 27.5 V, which was promising for embedded circuits. These preliminary data show that the **[2,1-*b*]-105** based OFET can be used under real polarization with no degradation of on and off voltage for V_{out} (12 hours polarization).

[2,1-*b*]-106 (Scheme 26) is a 3D small molecule acceptor, which has been used as a non-fullerene electron acceptor in bulk-heterojunction (BHJ) solar cells.[180] TGA analysis reveals for **[2,1-*b*]-106** a T_d of 460 °C, almost identical to the one measured for **[2,1-*b*]-84** (450 °C)[179] showing that very good thermal properties were maintained despite different bridge substitution. The LUMO of **[2,1-*b*]-106** was measured by cyclic voltammetry at −3.63 eV, slightly higher than that measured for **[2,1-*b*]-105** under similar conditions (−3.81 eV). This is directly connected to the number of dicyanovinylene fragments linked to each [2,1-*b*]-DHIF core, one in **[2,1-*b*]-106** and two in **[2,1-*b*]-105**.

To demonstrate the potential application of **[2,1-*b*]-106** as an acceptor in photovoltaic devices, **[2,1-*b*]-106** was blended with polythieno[3,4-*b*]-thiophene-*co*-bezodithiophene (PTB7) as an electron-donor polymer. PTB7 polymer absorption is partially complementary to the absorption of **[2,1-*b*]-106**.[180]

BHJ organic photovoltaic (OPV) devices with the structure ITO/PEDOT:PSS/PTB7:**[2,1-*b*]-106**/Ca/Al were fabricated varying the mode of preparation in modifying (i) the donor–acceptor weight ratio (1 : 1 or 1 : 2) and (ii) the solvent used to prepare the device (tetrachloroethane (TCE), dichlorobenzene (DCB) or a mixture TCE/DBE or TCE/3% 1,8-diiodooctane (DIO)). BHJ-OPV1 prepared from TCE with a donor:acceptor ratio, PTB7:**[2,1-*b*]-106** of 1 : 2 exhibited an open-circuit voltage (V_{OC}) of 0.87 V, a short-circuit current density (J_{SC}) of 1.13 mA cm^{-2}, a fill factor (FF) of 0.49 and a power conversion efficiency (PCE) of 0.64%. In BHJ-OPV2, the donor:acceptor ratio was 1 : 1 and led to an increase of the whole performances with a PCE reaching 0.8%. Changing the solvent for the three last devices (BHJ-OPV3 to BHJ-OPV5) was not efficient or even did not work. However, BHJ-OPV2 even with modest performances demonstrate that **[2,1-*b*]-106** could be an alternative to fullerene-based acceptors.

To end, **[1,2-*a*]-107**, **[1,2-*a*]-108** and **[1,2-*a*]-109** (Scheme 26) all based on a central truxene were used in DSSCs. These three dyes possess thienyl-2-cyanoacrylic acid as the acceptor and starbust diarylamine as the donor. The central truxene was substituted either by ethyl groups in **[1,2-*a*]-107** or by longer hexyl-substituents in **[1,2-*a*]-108** and **[1,2-*a*]-109**. In solution in DCM, all organic semiconductors exhibit two prominent

absorption bands between 300–360 nm (localized π–π* transitions) and between 400–450 nm (charge transfer transition). The extinction coefficients of **[1,2-*a*]-109** (4.13×10^{-4} L mol^{-1} cm^{-1} at 430 nm and 6.65×10^{-4} L mol^{-1} cm^{-1} at 365 nm) appear more intense than those of the two others (2.75×10^{-4} L mol^{-1} cm^{-1} at 406 nm and 5.42×10^{-4} L mol^{-1} cm^{-1} at 361 nm for **[1,2-*a*]-107** and 2.49×10^{-4} L mol^{-1} cm^{-1} at 420 nm and 5.44×10^{-4} L mol^{-1} cm^{-1} at 360 nm for **[1,2-*a*]-108**) due to the stronger electron-donating capability of **[1,2-*a*]-109** with methoxy groups. Thin films were deposited on TiO_2 surfaces and the absorption spectra present for each organic semiconductor a large absorption band centered at *ca.* 425 nm. The maximum absorption spectrum of **[1,2-*a*]-107** in the solid state was shifted from 406 nm (in solution) to 422 nm and the spectrum was broadened indicating a certain degree of π–π aggregation for **[1,2-*a*]-107**, which does not exist for the two other dyes possessing longer alkyl substituents on the central truxenyl core (hexyl instead of ethyl).

Due to the four methoxy groups decorating **[1,2-*a*]-109**, its HOMO level was higher (−4.98 eV) than that of the two other dyes (−5.22/−5.15eV for **[1,2-*a*]-107**/**[1,2-*a*]-108**). The LUMOs (calculated from their HOMO and optical gaps) were reported at −2.91/−2.84 and −2.72 eV respectively for the three dyes indicating that the electron injection process from the excited dyes to the TiO_2 conduction band (−4.4 eV) was energetically achievable. The performance of DSSCs shows the highest PCE for DSSC8 based on **[1,2-*a*]-108**) (4.27%), higher than the one of DSSC7 (3.90%) based on **[1,2-*a*]-107**) highlighting the positive effect of the hexyl chains on the electron injection efficiency because of the weak π–π aggregation. The higher V_{OC} for DSSC8 and DSSC9 than for DSCC7 indicate that the charge recombination process was retarded in the devices based on **[1,2-*a*]-108** and **[1,2-*a*]-109** due to the cone-shape sensitizer, which could constitute a compact layer at the TiO_2 surface to avoid the approach of the redox couple. The present results remain nevertheless modest. However, modulation of the DSSCs performances by the molecular structural modification remains the more important effect in this work.

5. Conclusion

The development of the dihydroindeno[1,2-*b*]fluorene molecular fragment as a building unit for the design of organic semiconductors has been important in the last two decades. This fragment has found applications in the three main devices of organic electronics, namely OLEDs, OFETs and OPVs, showing its real versatility. Positional isomerism, more and more used in the design of organic semiconductors, has allowed, over the years, to consider four other positional isomers of dihydroindeno[1,2-*b*]fluorene with different phenyl connections (*ortho*, *meta* or *para* linkages), which not only provide different π-conjugation pathways but also different geometries. The five positional isomers have been a fertile playground for molecular chemists to construct organic semiconductors. However, it is clear that the structural diversity provided by these isomers has not been fully exploited yet.

In this review, the five isomers and more than one hundred of their derivatives have been reviewed and the description of their uses as active components in different devices have highlighted their high interest for use in electronics. For each isomer family, the physicochemical properties were discussed and compared to relevant building units, in order to highlight the importance of molecular design on the electronic and physical properties, *i.e.* HOMO/LUMO energy levels, singlet/triplet energy, charge carrier mobility, decomposition temperature, *etc.* We show how substitution of either bridges and/or phenyl units offers many design combinations, which can be fitted for a specific application.

However, the [1,2-*b*] isomer has been far more developed than the other positional isomers, surely due to synthetic features. Nevertheless, the other isomers present very interesting properties due either to their different geometries or to their intrinsic electronic characteristics. For example, modulation of the linkages from *para* linkages in the [1,2-*b*] isomer to *meta* linkages in [1,2-*a*] and [2,1-*b*] isomers has been an efficient tool to tune the electronic properties. This has allowed a significant increase in the triplet state energy allowing the design of host materials for blue PhOLED applications. This was particularly interesting as most of the time high triplet host materials display a very short π-conjugated pathway. However, only a very limited number of examples are described in the literature and in future years, these cores might be decorated for that purpose (incorporating for example high-efficiency functional units such as electron-accepting phosphine oxides and electron-donating phenylacridine). Similarly, although considerable efforts have been made, only a limited number of compounds have reached high mobility values. This shows that significant improvements in terms of molecular design are still possible with these fragments.

Another interesting direction for the future consists of the use of different π-conjugated systems of different isomers to control the ICT between a donor- and an acceptor-fragment. Indeed, if many donor/acceptor molecules based on the [1,2-*b*] isomer, with functional units attached at each extremity, have been reported, the number of molecules incorporating the other isomers is very limited.

The different geometry of these isomers is also an important point still understudied. The best example is the [2,1-*a*] isomer in which the arrangement of the two bridges allow us to force interaction between attached substituents, providing singular optical and electrochemical properties. In the [2,1-*b*] isomer, the two bridges also present a similar arrangement but further apart. This particularity has nevertheless not been exploited yet.

In recent years, other applications of dihydroindenofluorene building units, not linked to electronics, have been reported in the literature, showing the versatility of this fragment. For example, in 2017, Wuest and coworkers have reported predictably ordered materials based on the [1,2-*b*] isomer.[221] These materials crystallized to form open hydrogen-bonded networks with a significant volume available for accepting guest molecules. Using the other isomers may offer very different arrangements, which can tune the materials cavity.

In 2021, an organic cathode material using **[1,2-*b*]IF(=O)$_2$** for lithium batteries was reported. Each carbonyl presents a four-electron

reduction giving a high energy density of 1392 W h kg^{-1}.[222] This organic electrode material is among the most efficient reported to date and show the real potential of the dihydroindenofluorene backbone in the field of batteries.

Dihydroindeno[1,2-*b*]fluorene has also been integrated, in 2022, in the design of catalysts.[223] A ruthenocene bimetallic complex incorporating this fragment was synthesized and tested as a burning rate catalyst on the thermal decomposition of ammonium perchlorate. The performance reached was promising with notably a reduction in the activation energy compared to other ruthenium complexes previously reported in the literature. It is impressive to see how this fragment can be very efficient in very different fields.

However, in these last three examples, the [1,2-*b*] isomer is again used. To develop more in depth the other positional isomers, improving their synthesis is a mandatory step. This could be achieved by modern synthetic approaches such as those recently develop by Akhmetov and coworkers with C_{aryl}–F bond activation.[224] Using alumina-mediated C–F bond activation, they managed to synthesize the [2,1-*b*]-isomer. Another interesting example is provided by Kotora and coworkers in 2020, who have reported an efficient Rh-catalysed intramolecular [2 + 2 + 2] cyclotrimerization of triyndiols to efficiently provide a series of dihydroindeno[2,1-*c*]fluorene.[225] This approach has also been used to synthesize [7]-helical extended DSF-IFs, which appears as an interesting route to design, in the future, other chiral materials based on the [2,1-*c*]-DHIF core.[226]

As discussed herein, the dihydroindeno[1,2-*b*] fluorene positional isomers, the flagship parent of the dihydroindenofluorene family has become a major player in the field of organic electronics. The other positional isomers have been far less developed but deserve, undoubtedly, particular attention. Future rational designs of these five exciting π-conjugated systems may have the ambition to reach state of the art device performances. This constitutes an exciting journey.

Conflicts of interest

There are no conflicts to declare.

Acknowledgements

The authors thank all their collaborators, who have been involved in the projects and especially the PhD students: Dr Damien Thirion, Dr Nicolas Cocherel, Dr Maxime Romain, Dr Sébastien Thiery, Dr Jean-David Peltier, Dr Lambert Sicard, and Dr Fabien Lucas. The authors also thank the CNRS, the University of Rennes 1, the ANR (11-BS07-020-01/14-CE05-0024/19/CE05-0024, CE07-0041), the Ademe and the Région Bretagne for their respective financial supports.

References

1 G. Hong, X. Gan, C. Leonhardt, Z. Zhang, J. Seibert, J. M. Busch and S. Bräse, *Adv. Mater.*, 2021, **33**, 2005630.
2 D. Xia, C. Duan, S. Liu, D. Ding, M. Baumgarten, M. Wagner, D. Schollmeyer, H. Xu and K. Müllen, *New J. Chem.*, 2019, **43**, 3788–3792.
3 C.-F. Wang, W.-Y. Hung, M.-H. Cheng, J.-S. Hwang, M.-K. Leung and K.-T. Wong, *Org. Electron.*, 2013, **14**, 1958–1965.
4 X. Li, H.-J. Chi, G.-H. Lu, G.-Y. Xiao, Y. Dong, D.-Y. Zhang, Z.-Q. Zhang and Z.-Z. Hu, *Org. Electron.*, 2012, **13**, 3138–3144.
5 H. Huang, Q. Fu, S. Zhuang, Y. Liu, L. Wang, J. Chen, D. Ma and C. Yang, *J. Phys. Chem. C*, 2011, **115**, 4872–4878.
6 H. P. Rathnayake, A. Cirpan, Z. Delen, P. M. Lahti and F. E. Karasz, *Adv. Funct. Mater.*, 2007, **17**, 115–122.
7 C. Tang, F. Liu, Y. J. Xia, J. Lin, L. H. Xie and G. Y. Zhong, *Org. Electron.*, 2006, **7**, 155.
8 D. Neher, *Macromol. Rapid Commun.*, 2001, **22**, 1365–1385.
9 I. Fischer and A. P. H. J. Schenning, in *Organic electronics: Emerging concepts and technologies*, eds. F. Cicoira and C. Santato, 2013, vol. 1, pp. 1–25.
10 M. Leclerc, *J. Polym. Sci., Part A: Polym. Chem.*, 2001, **39**, 2867–2873.
11 U. Scherf and E. J. W. List, *Adv. Mater.*, 2002, **14**, 477–487.
12 J. Rault-Berthelot, *Curr. Top. Electrochem.*, 2004, **10**, 265–284.
13 Q. Hou, Y. Xu, W. Yang, M. Yuan, J. Peng and Y. Cao, *J. Mater. Chem.*, 2002, **12**, 2887–2892.
14 S. Grigalevicius, L. Ma, Z.-Y. Xie and U. Scherf, *J. Polym. Sci., Part A: Polym. Chem.*, 2006, **44**, 5987–5994.
15 K. T. Kamtekar, H. L. Vaughan, B. P. Lyons, A. P. Monkman, S. U. Pandya and M. R. Bryce, *Macromolecules*, 2010, **43**, 4481–4488.
16 P. Leclère, M. Surin, P. Brocorens, M. Cavallini, F. Biscarini and R. Lazzaroni, *Mater. Sci. Eng., R*, 2006, **55**, 1–56.
17 C. K. Frederickson, B. D. Rose and M. M. Haley, *Acc. Chem. Res.*, 2017, **50**, 977–987.
18 A. G. Fix, D. T. Chase and M. M. Haley, in *Polyarenes I. Topics in Current Chemistry*, eds. J. Siegel and Y. Wu, Springer, Berlin, Heidelberg, 2012, vol. 349, pp. 159–195.
19 C. Poriel, J. Rault-Berthelot, F. Barrière and A. M. Z. Slawin, *Org. Lett.*, 2008, **10**, 373–376.
20 D. Thirion, C. Poriel, F. Barrière, R. Métivier, O. Jeannin and J. Rault-Berthelot, *Org. Lett.*, 2009, **11**, 4794–4797.
21 D. Thirion, C. Poriel, J. Rault-Berthelot, F. Barrière and O. Jeannin, *Chem. – Eur. J.*, 2010, **16**, 13646–13658.
22 D. Thirion, M. Romain, J. Rault-Berthelot and C. Poriel, *J. Mater. Chem.*, 2012, **22**, 7149–7157.
23 M. Romain, D. Tondelier, J.-C. Vanel, B. Geffroy, O. Jeannin, J. Rault-Berthelot, R. Métivier and C. Poriel, *Angew. Chem., Int. Ed.*, 2013, **52**, 14147–14151.
24 M. Romain, S. Thiery, A. Shirinskaya, C. Declairieux, D. Tondelier, B. Geffroy, O. Jeannin, J. Rault-Berthelot, R. Métivier and C. Poriel, *Angew. Chem., Int. Ed.*, 2015, **54**, 1176–1180.
25 M. Romain, D. Tondelier, B. Geffroy, O. Jeannin, E. Jacques, J. Rault-Berthelot and C. Poriel, *Chem. – Eur. J.*, 2015, **21**, 9426–9439.
26 M. Romain, C. Quinton, D. Tondelier, B. Geffroy, O. Jeannin, J. Rault-Berthelot and C. Poriel, *J. Mater. Chem. C*, 2016, **4**, 1692–1703.

27 C. Poriel and J. Rault-Berthelot, *Acc. Chem. Res.*, 2018, **51**, 1818–1830.
28 J. Jacob, L. Oldridge, J. Zhang, M. Gaal, E. J. W. List, A. C. Grimsdale and K. Müllen, *Curr. Appl. Phys.*, 2004, **4**, 339–342.
29 A. C. Grimsdale, P. Leclere, R. Lazzaroni, J. D. MacKenzie, C. Murphy, S. Setayesh, C. Silva, R. H. Friend and K. Müllen, *Adv. Funct. Mater.*, 2002, **12**, 729–733.
30 J. Kim, S. H. Kim, I. H. Jung, E. Jeong, Y. Xia, S. Cho, I.-W. Hwang, K. Lee, H. Suh, H.-K. Shim and H. Y. Woo, *J. Mater. Chem.*, 2010, **20**, 1577–1586.
31 A. Can, A. Facchetti and H. Usta, *J. Mater. Chem. C*, 2022, **10**, 8496–8535.
32 W. Deuschel, *Helv. Chim. Acta*, 1951, **34**, 2403–2416.
33 O. M. Behr, G. Eglinton, A. R. Galbraith and R. A. Raphael, *J. Chem. Soc.*, 1960, 3614–3625.
34 L. Chardonnens and L. Salamin, *Helv. Chim. Acta*, 1968, **51**, 1095–1102.
35 L. Chardonnens and L. Avar, *Helv. Chim. Acta*, 1969, **52**, 1091–1095.
36 R. G. Harvey, J. Pataki, C. Cortez, P. Di Raddo and C. X. Yang, *J. Org. Chem.*, 1991, **56**, 1210–1217.
37 S. Merlet, M. Birau and Z. Y. Wang, *Org. Lett.*, 2002, **4**, 2157–2159.
38 Y. Wang, P. R. McGonigal, B. Herlé, M. Besora and A. M. Echavarren, *J. Am. Chem. Soc.*, 2014, **136**, 801–809.
39 C.-W. Lee, E.-C. Liu and Y.-T. Wu, *J. Org. Chem.*, 2015, **80**, 10446–10456.
40 C. Poriel, J.-J. Liang, J. Rault-Berthelot, F. Barrière, N. Cocherel, A. M. Z. Slawin, D. Horhant, M. Virboul, G. Alcaraz, N. Audebrand, L. Vignau, N. Huby, G. Wantz and L. Hirsch, *Chem. – Eur. J.*, 2007, **13**, 10055–10069.
41 T. P. I. Saragi, T. Spehr, A. Siebert, T. Fuhrmann-Lieker and J. Salbeck, *Chem. Rev.*, 2007, **107**, 1011–1065.
42 C. Poriel, L. J. Sicard and J. Rault-Berthelot, *Chem. Commun.*, 2019, **55**, 14238–14254.
43 C.-C. Hsiao, Y.-K. Lin, C.-J. Liu, T.-C. Wu and Y.-T. Wu, *Adv. Synth. Catal.*, 2010, **352**, 3267–3274.
44 L. Sicard, C. Quinton, J.-D. Peltier, D. Tondelier, B. Geffroy, U. Biapo, R. Métivier, O. Jeannin, J. Rault-Berthelot and C. Poriel, *Chem. – Eur. J.*, 2017, **23**, 7719–7727.
45 D. Horhant, J.-J. Liang, M. Virboul, C. Poriel, G. Alcaraz and J. Rault-Berthelot, *Org. Lett.*, 2006, **8**, 257–260.
46 I. B. Berlman, *J. Chem. Phys.*, 1970, **52**, 5616–5621.
47 G. Heimel, M. Daghofer, J. Gierschner, E. J. List, A. C. Grimsdale, K. Mullen, D. Beljonne, J. L. Bredas and E. Zojer, *J. Chem. Phys.*, 2005, **122**, 054501–054511.
48 J. Rault-Berthelot, C. Poriel, F. Justaud and F. Barrière, *New J. Chem.*, 2008, **32**, 1259–1266.
49 J. Rault-Berthelot and J. Simonet, *J. Electroanal. Chem.*, 1985, **182**, 187–192.
50 J. Rault-Berthelot, M.-M. Granger and L. Mattiello, *Synth. Met.*, 1998, **97**, 211–215.
51 C. Poriel, Y. Ferrand, P. Le Maux, J. Rault-Berthelot and G. Simonneaux, *Inorg. Chem.*, 2004, **43**, 5086–5095.
52 C. Poriel, Y. Ferrand, P. Le Maux, C. Paul-Roth, G. Simonneaux and J. Rault-Berthelot, *J. Electroanal. Chem.*, 2005, **583**, 92–103.
53 C. Poriel and J. Rault-Berthelot, *Adv. Funct. Mater.*, 2020, **30**, 1910040.
54 T. Hadizad, J. Zhang, Z. Y. Wang, T. C. Gorjanc and C. Py, *Org. Lett.*, 2005, **7**, 795–797.
55 T. Hadizad, J. Zhang, D. Yan, Z. Y. Wang, J. P. M. Serbena, M. S. Meruvia and I. A. Hümmelgen, *J. Mater. Sci.: Mater. Electron.*, 2007, **18**, 903–912.
56 N. Cocherel, C. Poriel, J. Rault-Berthelot, F. Barrière, N. Audebrand, A. M. A. Slawin and L. Vignau, *Chem. – Eur. J.*, 2008, **14**, 11328–11342.
57 N. Cocherel, C. Poriel, L. Vignau, J.-F. Bergamini and J. Rault-Berthelot, *Org. Lett.*, 2010, **12**, 452–455.
58 C. Poriel, N. Cocherel, J. Rault-Berthelot, L. Vignau and O. Jeannin, *Chem. – Eur. J.*, 2011, **17**, 12631–12645.
59 C. Poriel, J. Rault-Berthelot and D. Thirion, *J. Org. Chem.*, 2013, **78**, 886–898.
60 L.-H. Xie, X.-Y. Hou, C. Tang, Y.-R. Hua, R.-J. Wang, R.-F. Chen, Q.-L. Fan, L.-H. Wang, W. Wei, B. Peng and W. Huang, *Org. Lett.*, 2006, **8**, 1363–1366.
61 J.-D. Peltier, B. Heinrich, B. Donnio, O. Jeannin, J. Rault-Berthelot and C. Poriel, *Chem. – Eur. J.*, 2017, **23**, 17290–17303.
62 Z. Jiang, H. Yao, Z. Liu, C. Yang, C. Zhong, J. Qin, G. Yu and Y. Liu, *Org. Lett.*, 2009, **11**, 4132–4135.
63 M. Lv, X. Lu, Y. Jiang, M. E. Sandoval-Salinas, D. Casanova, H. Sun, Z. Sun, J. Xu, Y. Yang and J. Chen, *Angew. Chem., Int. Ed.*, 2022, **61**, e202113190.
64 C.-C. Wu, W.-G. Liu, W.-Y. Hung, T.-L. Liu, Y.-T. Lin, H.-W. Lin, K.-T. Wong, Y.-Y. Chien, R.-T. Chen, T.-H. Hung, T.-C. Chao and Y.-M. Chen, *Appl. Phys. Lett.*, 2005, **87**, 052103.
65 P. Maslak, *Adv. Mater.*, 1994, **6**, 405–407.
66 H. E. Simmons and T. Fukunaga, *J. Am. Chem. Soc.*, 1967, **89**, 5208–5215.
67 S.-Y. Ku, L.-C. Chi, W.-Y. Hung, S.-W. Yang, T.-C. Tsai, K.-T. Wong, Y.-H. Chen and C.-I. Wu, *J. Mater. Chem.*, 2009, **19**, 773–780.
68 K.-T. Wong, L.-C. Chi, S.-C. Huang, Y.-L. Liao, Y.-H. Liu and Y. Wang, *Org. Lett.*, 2006, **8**, 5029–5032.
69 Y. Park, J.-H. Lee, D. H. Jung, S.-H. Liu, Y.-H. Lin, L.-Y. Chen, C.-C. Wu and J. Park, *J. Mater. Chem.*, 2010, **20**, 5930–5936.
70 A. P. Kulkarni, C. J. Tonzola, A. Babel and S. A. Jenekhe, *Chem. Mater.*, 2004, **16**, 4556–4573.
71 D. Thirion, J. Rault-Berthelot, L. Vignau and C. Poriel, *Org. Lett.*, 2011, **13**, 4418–4421.
72 D. Thirion, M. Romain, J. Rault-Berthelot and C. Poriel, *Mater. Adv.*, 2021, **2**, 1271–1283.
73 C. Poriel and J. Rault-Berthelot, *Adv. Funct. Mater.*, 2021, **31**, 2010547.
74 F. Barrière, C. Poriel and J. Rault-Berthelot, *Electrochim. Acta*, 2013, **110**, 735–740.
75 D. Thirion, C. Poriel, R. Métivier, J. Rault-Berthelot, F. Barrière and O. Jeannin, *Chem. – Eur. J.*, 2011, **17**, 10272–10287.

76 K. H. Lee, S. O. Kim, S. Kang, J. Y. Lee, K. S. Yook, J. Y. Lee and S. S. Yoon, *Eur. J. Org. Chem.*, 2012, 2748–2755.
77 K. H. Lee, S. O. Kim, J. N. You, S. Kang, J. Y. Lee, K. S. Yook, S. O. Jeon, J. Y. Lee and S. S. Yoon, *J. Mater. Chem.*, 2012, **22**, 5145–5154.
78 Q. Meng and W. Hu, *Phys. Chem. Chem. Phys.*, 2012, **14**, 14152–14164.
79 S. Kola, J. Sinha and H. E. Katz, *J. Polym. Sci., Part B: Polym. Phys.*, 2012, **50**, 1090–1120.
80 C. Wang, H. Dong, W. Hu, Y. Liu and D. Zhu, *Chem. Rev.*, 2012, **112**, 2208–2267.
81 K. Zhou, H. Dong, H.-I. Zhang and W. Hu, *Phys. Chem. Chem. Phys.*, 2014, **16**, 22448–22457.
82 X. Gao and Z. Zhao, *Sci. China: Chem.*, 2015, **58**, 947–968.
83 C. Py, T. C. Gorjanc, T. Hadizad, J. Zhang and Z. Y. Wang, *J. Vac. Sci. Technol., A*, 2006, **24**, 654–656.
84 J. P. M. Serbena, I. A. Hümmelgen, T. Hadizad and Z. Y. Wang, *Small*, 2006, **2**, 372–374.
85 J. P. M. Serbena, J. Y. Huang, D. Ma, Z. Y. Wang and I. A. Hümmelgen, *Org. Electron.*, 2009, **10**, 357–362.
86 T. Nakagawa, D. Kumaki, J.-I. Nishida, S. Tokito and Y. Yamashita, *Chem. Mater.*, 2008, **20**, 2615–2617.
87 H. Usta, C. Risko, Z. Wang, H. Huang, M. K. Deliomeroglu, A. Zhukhovitskiy, A. Facchetti and T. J. Marks, *J. Am. Chem. Soc.*, 2009, **131**, 5586–5608.
88 Z.-P. Fan, X.-Y. Li, X.-E. Luo, X. Fei, B. Sun, L.-C. Chen, Z.-F. Shi, C.-L. Sun, X. Shao and H.-L. Zhang, *Adv. Funct. Mater.*, 2017, **27**, 1702318.
89 Y.-I. Park, J. S. Lee, B. J. Kim, B. Kim, J. Lee, D. H. Kim, S.-Y. Oh, J. H. Cho and J.-W. Park, *Chem. Mater.*, 2011, 4038–4044.
90 B. J. Kim, Y.-I. Park, H. J. Kim, K. Ahn, D. R. Lee, D. H. Kim, S.-Y. Oh, J.-W. Park and J. H. Cho, *J. Mater. Chem.*, 2012, **22**, 14617–14623.
91 Y. Miyata, T. Minari, T. Nemoto, S. Isoda and K. Komatsu, *Org. Biomol. Chem.*, 2007, **5**, 2592–2598.
92 M. Ozdemir, D. Choi, G. Kwon, Y. Zorlu, H. Kim, M.-G. Kim, S. Seo, U. Sen, M. Citir, C. Kim and H. Usta, *RSC Adv.*, 2016, **6**, 212–226.
93 R. Ozdemir, D. Choi, M. Ozdemir, G. Kwon, H. Kim, U. Sen, C. Kim and H. Usta, *J. Mater. Chem. C*, 2017, **5**, 2368–2379.
94 R. Ozdemir, S. Park, İ. Deneme, Y. Park, Y. Zorlu, H. A. Alidagi, K. Harmandar, C. Kim and H. Usta, *Org. Chem. Front.*, 2018, **5**, 2912–2924.
95 H. Usta, A. Facchetti and T. J. Marks, *Acc. Chem. Res.*, 2011, **44**, 501–510.
96 Y.-J. Cheng, J. Luo, S. Huang, X. Zhou, Z. Shi, T.-D. Kim, D. H. Bale, S. Takahashi, A. Yick, B. M. Polishak, S.-H. Jang, L. R. Dalton, P. J. Reid, W. H. Steier and A. K. Y. Jen, *Chem. Mater.*, 2008, **20**, 5047–5054.
97 F. Liu, F. Wu, Z. Tu, Q. Liao, Y. Gong, L. Zhu, Q. Li and Z. Li, *Adv. Funct. Mater.*, 2019, **29**, 1901296.
98 H. Usta, A. Facchetti and T. J. Marks, *J. Am. Chem. Soc.*, 2008, **130**, 8580–8581.
99 S. Bebiche, P. Cisneros-Perez, T. Mohammed-Brahim, M. Harnois, J. Rault-Berthelot, C. Poriel and E. Jacques, *Mater. Chem. Front.*, 2018, **2**, 1631–1641.
100 N. Arfaoui, M. Mahdouani, I. Bouhadda, C. Poriel, R. Bourguiga, E. Jacques, M. Chevrier and S. Bebiche, *Superlattices Microstruct.*, 2018, **123**, 286–296.
101 E. Jacques, M. Romain, A. Yassin, S. Bebiche, M. Harnois, T. Mohammed-Brahim, J. Rault-Berthelot and C. Poriel, *J. Mater. Chem. C*, 2014, **2**, 3292–3302.
102 X. Gao and Y. Hu, *J. Mater. Chem. C*, 2014, **2**, 3099–3117.
103 Y. Zhao, Y. Guo and Y. Liu, *Adv. Mater.*, 2013, **25**, 5372–5391.
104 L. Feng, H. Dong, Q. Li, W. Zhu, G. Qiu, S. Ding, Y. Li, M. A. Christensen, C. R. Parker, Z. Wei, M. B. Nielsen and W. Hu, *Sci. China Mater.*, 2017, **60**, 75–82.
105 M. A. Christensen, C. R. Parker, T. J. Sørensen, S. de Graaf, T. J. Morsing, T. Brock-Nannestad, J. Bendix, M. M. Haley, P. Rapta, A. Danilov, S. Kubatkin, O. Hammerich and M. B. Nielsen, *J. Mater. Chem. C*, 2014, **2**, 10428–10438.
106 M. A. Baldo, D. F. O'Brien, Y. You, A. Shoustikov, S. Sibley, M. E. Thompson and S. R. Forrest, *Nature*, 1998, **395**, 151–154.
107 A. Chaskar, H.-F. Chen and K.-T. Wong, *Adv. Mater.*, 2011, **23**, 3876–3895.
108 H. Sasabe and J. Kido, *Chem. Mater.*, 2011, **23**, 621–630.
109 Y. Tao, C. Yang and J. Qin, *Chem. Soc. Rev.*, 2011, **40**, 2943–2970.
110 L. Xiao, Z. Chen, B. Qu, J. Luo, S. Kong, Q. Cong and J. Kido, *Adv. Mater.*, 2011, **23**, 926–952.
111 K. S. Yook and J. Y. L. Lee, *Adv. Mater.*, 2012, **24**, 3169–3190.
112 H. Sasabe and J. Kido, *Eur. J. Org. Chem.*, 2013, 7653–7663.
113 D. Chen, S.-J. Su and Y. Cao, *J. Mater. Chem. C*, 2014, **2**, 9565.
114 K. S. Yook and J. Y. Lee, *Adv. Mater.*, 2014, **26**, 4218–4233.
115 K. S. Yook and J. Y. Lee, *Chem. Rec.*, 2016, **16**, 159–172.
116 C. Poriel and J. Rault-Berthelot, *Acc. Mater. Res.*, 2022, **3**, 379–390.
117 L.-C. Chi, W.-Y. Hung, H.-C. Chiu and K.-T. Wong, *Chem. Commun.*, 2009, 3892–3894.
118 F. Lucas, D. Tondelier, B. Geffroy, T. Heiser, O. A. Ibraikulov, C. Quinton, C. Brouillac, N. Leclerc, J. Rault-Berthelot and C. Poriel, *Mater. Chem. Front.*, 2021, **5**, 8066–8077.
119 C. Poriel, R. Métivier, J. Rault-Berthelot, D. Thirion, F. Barrière and O. Jeannin, *Chem. Commun.*, 2011, **47**, 11703–11705.
120 S. Chaurasia, Y.-C. Chen, H.-H. Chou, Y.-S. Wen and J. T. Lin, *Tetrahedron*, 2012, **68**, 7755–7762.
121 J. Zhang, B. Zhao, Y. Mi, H. Liu, Z. Guo, G. Bie, W. Wei, C. Gao and Z. An, *Dyes Pigm.*, 2017, **140**, 261–268.
122 J. Mogensen, H. Michaels, R. Roy, L. Broløs, M. D. Kilde, M. Freitag and M. B. Nielsen, *Eur. J. Org. Chem.*, 2020, 6127–6134.
123 Z.-E. Chen, Q.-L. Qi and H. Zhang, *Synth. Met.*, 2020, **267**, 116473.
124 M. Pawlicki, H. A. Collins, R. G. Denning and H. L. Anderson, *Angew. Chem., Int. Ed.*, 2009, **48**, 3244–3266.
125 Q. Zheng, S. K. Gupta, G. S. He, L.-S. Tan and P. N. Prasad, *Adv. Funct. Mater.*, 2008, **18**, 2770–2779.
126 Z. Liu, D. Cao, Y. Chen and Q. Fang, *Dyes Pigm.*, 2010, **86**, 63–67.

127 Á. M. Marín, J. P. Telo, D. Collado, F. Nájera, E. Pérez-Inestrosa and U. Pischel, *Chem. – Eur. J.*, 2018, **24**, 2929–2935.
128 H. H. Fan, L. Guo, K. F. Li, M. S. Wong and K. W. Cheah, *J. Am. Chem. Soc.*, 2012, **134**, 7297–7300.
129 D. An and Z. Ye, *J. Chil. Chem. Soc.*, 2015, **60**, 2971–2974.
130 L. Guo, K. F. Li, M. S. Wong and K. W. Cheah, *Chem. Commun.*, 2013, **49**, 3597–3599.
131 L. Guo, X. Liu, T. Zhang, H.-B. Luo, H. H. Fan and M. S. Wong, *J. Mater. Chem. C*, 2020, **8**, 1768–1772.
132 T.-C. Lin, C.-S. Hsu, C.-L. Hu, Y.-F. Chen and W.-J. Huang, *Tetrahedron Lett.*, 2009, **50**, 182–185.
133 S. Welter, N. Salluce, A. Benetti, N. Rot, P. Belser, P. Sonar, A. C. Grimsdale, K. Müllen, M. Lutz, A. L. Spek and L. De Cola, *Inorg. Chem.*, 2005, **44**, 4706–4718.
134 Y. Ie, M. Nitani and Y. Aso, *Chem. Lett.*, 2007, **36**, 1326–1327.
135 S. Thiery, B. Heinrich, B. Donnio, C. Poriel and F. Camerel, *J. Mater. Chem. C*, 2014, **2**, 4265–4275.
136 H. So, J. H. Kim, J. H. Lee, H. Hwang, D. K. An and K. M. Lee, *Chem. Commun.*, 2019, **55**, 14518–14521.
137 K.-W. Park and T. L. Andrew, *J. Phys. Chem. C*, 2022, **126**, 17663–17669.
138 W. Schroth and K. Schmidt, *Chem*, 1963, **3**, 309.
139 J.-H. Ho, Y.-C. Lin, L.-T. Chou, Y.-Z. Chen, W.-Q. Liu and C.-L. Chuang, *Tetrahedron Lett.*, 2013, **54**, 1991–1993.
140 W. Dilthey, I. Thewalt and O. Trösken, *Ber. Dtsch. Chem. Ges.*, 1934, **67**, 1959–1964.
141 C. Weizmann, E. Bergmann and L. Haskelberg, *J. Chem. Soc.*, 1939, 391–397.
142 C. Poriel, J. Rault-Berthelot, D. Thirion, F. Barrière and L. Vignau, *Chem. – Eur. J.*, 2011, **17**, 14031–14046.
143 C. Poriel, F. Barrière, D. Thirion and J. Rault-Berthelot, *Chem. – Eur. J.*, 2009, **15**, 13304–13307.
144 C. Poriel, F. Barrière, J. Rault-Berthelot and D. Thirion, *Chem. – Eur. J.*, 2019, **25**, 10689–10697.
145 P. Hapiot, C. Lagrost, F. Le Floch, E. Raoult and J. Rault-Berthelot, *Chem. Mater.*, 2005, **17**, 2003–2012.
146 K.-T. Wong, Y.-Y. Chien, R.-T. Chen, C.-F. Wang, Y.-T. Lin, H.-H. Chiang, P.-Y. Hsieh, C.-C. Wu, C. H. Chou, Y. O. Su, G.-H. Lee and S.-M. Peng, *J. Am. Chem. Soc.*, 2002, **124**, 11576–11577.
147 S. Tang, M. Liu, C. Gu, Y. Zhao, P. Lu, D. Lu, L. Liu, F. Shen, B. Yang and Y. Ma, *J. Org. Chem.*, 2008, **73**, 4212–4218.
148 G. Klaerner and R. D. Miller, *Macromolecules*, 1998, **31**, 2007–2009.
149 C.-C. Wu, T.-L. Liu, Y.-T. Lin, W.-Y. Hung, T.-H. Ke, K.-T. Wong and T.-C. Chao, *Appl. Phys. Lett.*, 2004, **85**, 1172–1174.
150 H. Li, A. S. Batsanov, K. C. Moss, H. L. Vaughan, F. B. Dias, K. T. R. Kamtekar, M. R. Bryce and A. P. Monkman, *Chem. Commun.*, 2010, **46**, 4812–4814.
151 E. J. W. List, R. Guentner, P. Scandiucci de Freitas and U. Scherf, *Adv. Mater.*, 2002, **14**, 374–378.
152 X. Chen, H.-T. Tseng, J.-L. Liao and S.-A. Chen, *J. Phys. Chem. B*, 2005, **109**, 17496–17502.
153 F. Montilla and R. Mallavia, *Adv. Funct. Mater.*, 2007, **17**, 71–78.
154 S. Kappaun, H. Scheiber, R. Trattnig, E. Zojer, E. J. W. List and C. Slugovc, *Chem. Commun.*, 2008, 5170–5172.
155 Y.-F. Bo, Y.-Y. Liu, H. Soleimaninejad, M.-N. Yu, L.-H. Xie, T. A. Smith, K. P. Ghiggino and W. Huang, *J. Phys. Chem. A*, 2019, **123**, 2789–2795.
156 T. Takeda, K. Inukai, K. Tahara and Y. Tobe, *J. Org. Chem.*, 2011, **76**, 9116–9121.
157 S. Nobusue and Y. Tobe, *Synlett*, 2016, 2140–2144.
158 S. Li, M. Aljhdli, H. Thakellapalli, B. Farajidizaji, Y. Zhang, N. G. Akhmedov, C. Milsmann, B. V. Popp and K. K. Wang, *Org. Lett.*, 2017, **19**, 4078–4081.
159 Y. Wei, X. Zheng, D. Lin, H. Yuan, Z. Yin, L. Yang, Y. Yu, S. Wang, L.-H. Xie and W. Huang, *J. Org. Chem.*, 2019, **84**, 10701–10709.
160 L. Sicard, O. Jeannin, J. Rault-Berthelot, C. Quinton and C. Poriel, *ChemPlusChem*, 2018, **83**, 874–880.
161 F. Lucas, L. Sicard, O. Jeannin, J. Rault-Berthelot, E. Jacques, C. Quinton and C. Poriel, *Chem. – Eur. J.*, 2019, **25**, 7740–7748.
162 D. Radulescu and M. Alexa, *Bul. Chim., Soc. Chim. Romania*, 1939, **1**, 25–29.
163 L. Chardonnens and R. Ritter, *Helv. Chim. Acta*, 1955, **38**, 393–396.
164 W. Kemp and J. Spanswick, *J. Chem. Soc. C*, 1967, 2544–2545.
165 Y. Altman and D. Ginsburg, *J. Chem. Soc.*, 1961, 1498–1505.
166 L. Chardonnens and J. Häger, *Helv. Chim. Acta*, 1970, **53**, 843–847.
167 M. Nierenstein and C. W. Webster, *J. Am. Chem. Soc.*, 1945, **67**, 691–692.
168 W. Deuschel, *Helv. Chim. Acta*, 1951, **34**, 168–185.
169 L. Chardonnens and H. Chardonnens, *Helv. Chim. Acta*, 1958, **41**, 2109–2111.
170 M. Romain, M. Chevrier, S. Bebiche, T. Mohammed-Brahim, J. Rault-Berthelot, E. Jacques and C. Poriel, *J. Mater. Chem. C*, 2015, **3**, 5742–5753.
171 L. Chardonnens and J. Rody, *Helv. Chim. Acta*, 1959, **42**, 1328–1331.
172 W. Deuschel, *Helv. Chim. Acta*, 1952, **35**, 1774–1776.
173 L. Chardonnens and H. Chardonnens, *Helv. Chim. Acta*, 1966, **49**, 1931–1934.
174 B. Du, L. Wang, S.-C. Yuan, T. Lei, J. Pei and Y. Cao, *Polymer*, 2013, **54**, 2935–2944.
175 Y.-Y. Li, H.-Y. Lu, M. Li, X.-J. Li and C.-F. Chen, *J. Org. Chem.*, 2014, **79**, 2139–2147.
176 R. P. Kaiser, D. Nečas, T. Cadart, R. Gyepes, I. Císařová, J. Mosinger, L. Pospíšil and M. Kotora, *Angew. Chem., Int. Ed.*, 2019, **58**, 17169–17174.
177 J.-D. Peltier, B. Heinrich, B. Donnio, O. Jeannin, J. Rault-Berthelot, E. Jacques and C. Poriel, *J. Mater. Chem. C*, 2018, **6**, 13197–13210.
178 C. Poriel, C. Quinton, F. Lucas, J. Rault-Berthelot, Z.-Q. Jiang and O. Jeannin, *Adv. Funct. Mater.*, 2021, **31**, 2104980.
179 L. Zhao, C. Duan, D. Ding, S. Liu, D. Xia, Y. Guo, H. Xu and M. Baumgarten, *Chin. Chem. Lett.*, 2021, **32**, 397–400.
180 D. Xia, D. Gehrig, X. Guo, M. Baumgarten, F. Laquai and K. Müllen, *J. Mater. Chem. A*, 2015, **3**, 11086–11092.

181 M. Kimura, S. Kuwano, Y. Sawaki, H. Fujikawa, K. Noda, Y. Taga and K. Takagi, *J. Mater. Chem.*, 2005, **15**, 2393–2398.
182 J. Luo, Y. Zhou, Z.-Q. Niu, Q.-F. Zhou, Y. Ma and J. Pei, *J. Am. Chem. Soc.*, 2007, **129**, 11314–11315.
183 T. Lei, J. Luo, L. Wang, Y. Ma, J. Wang, Y. Cao and J. Pei, *New J. Chem.*, 2010, **34**, 699–707.
184 F. Goubard and F. Dumur, *RSC Adv.*, 2015, **5**, 3521–3551.
185 C. Fan, Y. Chen, P. Gan, C. Yang, C. Zhong, J. Qin and D. Ma, *Org. Lett.*, 2010, **12**, 5648–5651.
186 C. Poriel, J. Rault-Berthelot and Z.-Q. Jiang, *Mater. Chem. Front.*, 2022, **6**, 1246–1252.
187 J. Ma, M. Idris, T. Y. Li, D. S. M. Ravinson, T. Fleetham, J. Kim, P. I. Djurovich, S. R. Forrest and M. E. Thompson, *Adv. Opt. Mater.*, 2022, **10**, 2101530.
188 F. Lucas, C. Brouillac, S. Fall, N. Zimmerman, D. Tondelier, B. Geffroy, N. Leclerc, T. Heiser, C. Lebreton, E. Jacques, C. Quinton, J. Rault-Berthelot and C. Poriel, *Chem. Mater.*, 2022, **34**, 8345–8355.
189 Q. Duez, M. Romain, C. Tonneaux, J. De Winter, V. Lemaur, J. Cornil, C. Poriel and P. Gerbaux, *Anal. Methods*, 2018, **10**, 2303–2306.
190 D. Li, J. Li, D. Liu, W. Li, C.-L. Ko, W.-Y. Hung and C. Duan, *ACS Appl. Mater. Interfaces*, 2021, **13**, 13459–13469.
191 K. Udagawa, H. Sasabe, C. Cai and J. Kido, *Adv. Mater.*, 2014, **26**, 5062–5066.
192 M. Kim and J. Y. Lee, *Adv. Funct. Mater.*, 2014, **24**, 4164–4169.
193 S.-y Chang, G.-T. Lin, Y.-C. Cheng, J.-J. Huang, C.-L. Chang, C.-F. Lin, J.-H. Lee, T.-L. Chiu and M.-k Leung, *ACS Appl. Mater. Interfaces*, 2018, **10**, 42723–42732.
194 C. W. Lee and J. Y. Lee, *Adv. Mater.*, 2013, **25**, 5450–5454.
195 Q.-L. Xu, X. Liang, S. Zhang, Y.-M. Jing, X. Liu, G.-Z. Lu, Y.-X. Zheng and J.-L. Zuo, *J. Mater. Chem. C*, 2015, **3**, 3694–3701.
196 G. Lu, R. Wu, N. Li, X. Wang, L. Zhou and C. Yang, *J. Mater. Chem. C*, 2022, **10**, 17303–17308.
197 M. Kim and J. Y. Lee, *ACS Appl. Mater. Interfaces*, 2014, **6**, 14874–14880.
198 H. Uoyama, K. Goushi, K. Shizu, H. Nomura and C. Adachi, *Nature*, 2012, **492**, 234.
199 Y. Fu, H. Liu, B. Z. Tang and Z. Zhao, *Nat. Commun.*, 2023, **14**, 2019.
200 T.-A. Lin, T. Chatterjee, W.-L. Tsai, W.-K. Lee, M.-J. Wu, M. Jiao, K.-C. Pan, C.-L. Yi, C.-L. Chung, K.-T. Wong and C.-C. Wu, *Adv. Mater.*, 2016, **28**, 6976–6983.
201 X. Hong, D. Zhang, C. Yin, Q. Wang, Y. Zhang, T. Huang, J. Wei, X. Zeng, G. Meng, X. Wang, G. Li, D. Yang, D. Ma and L. Duan, *Chem*, 2022, **8**, 1705–1719.
202 H. Liu, Z. Liu, G. Li, H. Huang, C. Zhou, Z. Wang and C. Yang, *Angew. Chem., Int. Ed.*, 2021, **60**, 12376–12380.
203 C.-C. Peng, S.-Y. Yang, H.-C. Li, G.-H. Xie, L.-S. Cui, S.-N. Zou, C. Poriel, Z.-Q. Jiang and L.-S. Liao, *Adv. Mater.*, 2020, **32**, 2003885.
204 D. H. Ahn, J. S. Moon, S. W. Kim, S. Y. Lee, D. Karthik, J. Y. Lee and J. H. Kwon, *Org. Electron.*, 2018, **59**, 39–44.
205 S.-J. Woo, Y. Kim, S.-K. Kwon, Y.-H. Kim and J.-J. Kim, *ACS Appl. Mater. Interfaces*, 2019, **11**, 7199–7207.
206 B. Li, Z. Li, T. Hu, Y. Zhang, Y. Wang, Y. Yi, F. Guo and L. Zhao, *J. Mater. Chem. C*, 2018, **6**, 2351–2359.
207 M. Godumala, S. Choi, S. Y. Park, M. J. Cho, H. J. Kim, D. H. Ahn, J. S. Moon, J. H. Kwon and D. H. Choi, *Chem. Mater.*, 2018, **30**, 5005–5012.
208 X.-Q. Wang, S.-Y. Yang, Q.-S. Tian, C. Zhong, Y.-K. Qu, Y.-J. Yu, Z.-Q. Jiang and L.-S. Liao, *Angew. Chem., Int. Ed.*, 2021, **60**, 5213–5219.
209 X. Tang, L. S. Cui, H. C. Li, A. J. Gillett, F. Auras, Y. K. Qu, C. Zhong, S. T. E. Jones, Z. Q. Jiang, R. H. Friend and L. S. Liao, *Nat. Mater.*, 2020, **19**, 1332–1338.
210 Z. Wang, D. Li, W. Li, J. Zhang, M. Luo, S. Du, X. Zhang, S. Xu and Z. Ge, *Adv. Opt. Mater.*, 2023, 2300017.
211 J. Jayakumar, T.-L. Wu, M.-J. Huang, P.-Y. Huang, T.-Y. Chou, H.-W. Lin and C.-H. Cheng, *ACS Appl. Mater. Interfaces*, 2019, **11**, 21042–21048.
212 P. Rajamalli, N. Senthilkumar, P. Y. Huang, C. C. Ren-Wu, H. W. Lin and C. H. Cheng, *J. Am. Chem. Soc.*, 2017, **139**, 10948–10951.
213 P. Rajamalli, V. Thangaraji, N. Senthilkumar, C.-C. Ren-Wu, H.-W. Lin and C.-H. Cheng, *J. Mater. Chem. C*, 2017, **5**, 2919–2926.
214 Y. Chen, Q. Sun, Y. Dai, D. Yang, X. Qiao and D. Ma, *J. Mater. Chem. C*, 2020, **8**, 13777–13785.
215 Z. Liu, G. Li, H. Liu, C. Zhou, K. Li, Z. Wang and C. Yang, *Adv. Opt. Mater.*, 2021, **9**, 2101410.
216 H. Peng, J. Lou, G. Li, C. Zhou, Z. Wang and H. Liu, *J. Mater. Chem. C*, 2022, **10**, 5813–5820.
217 H. Peng, Y. Xu, C. Zhou, R. Pei, J. Miao, H. Liu and C. Yang, *Adv. Funct. Mater.*, 2023, **33**, 2211696.
218 Y. Liu, Y. Xu, H. Peng, J. Miao, H. Liu and C. Yang, *Chem. Commun.*, 2023, **59**, 9255–9258.
219 S. Bebiche, I. Bouhadda, T. Mohammed-Brahim, N. Coulon, J. F. Bergamini, C. Poriel and E. Jacques, *Solid-State Electron.*, 2017, **130**, 49–56.
220 Z. Ning, Q. Zhang, H. Pei, J. Luan, C. Lu, Y. Cui and H. Tian, *J. Phys. Chem. C*, 2009, **113**, 10307–10313.
221 D. Beaudoin, J.-N. Blair-Pereira, S. Langis-Barsetti, T. Maris and J. D. Wuest, *J. Org. Chem.*, 2017, **82**, 8536–8547.
222 Z. Chen, P. Sun, P. Bai, H. Su, J. Yang, Y. Liu, Y. Xu and Y. Geng, *Chem. Commun.*, 2021, **57**, 10791–10794.
223 Y. Dibdalli, J. Gaete, C. Valdebenito, J. L. Arroyo, I. Martínez, G. Abarca and C. Morales-Verdejo, *J. Organomet. Chem.*, 2022, **973–974**, 122408.
224 M. Feofanov, A. Förtsch, K. Amsharov and V. Akhmetov, *Chem. Commun.*, 2021, **57**, 12325–12328.
225 I. Caivano, Z. Tošner, I. Císařová, D. Nečas and M. Kotora, *ChemPlusChem*, 2020, **85**, 2010–2016.
226 T. Cadart, D. Nečas, R. P. Kaiser, L. Favereau, I. Císařová, R. Gyepes, J. Hodačová, K. Kalíková, L. Bednárová, J. Crassous and M. Kotora, *Chem. – Eur. J.*, 2021, **27**, 11279–11284.